UNIVERSITY OF ŽILINA

TRANSCOM 2011

9-th EUROPEAN CONFERENCE
OF YOUNG RESEARCH AND SCIENTIFIC WORKERS

PROCEEDINGS

SECTION 4

ELECTRIC POWER SYSTEMS
ELECTRICAL AND ELECTRONIC ENGINEERING

ŽILINA June 27 - 29, 2011
SLOVAK REPUBLIC

UNIVERSITY OF ŽILINA

TRANSCOM 2011

9-th EUROPEAN CONFERENCE
OF YOUNG RESEARCH AND SCIENTIFIC WORKERS

under the auspices of

Ing. Eugen Jurzyca
Minister of Education, Science, Research and Sport of the Slovak Republic

&

Prof. Ing. Tatiana Čorejová, PhD.
Rector of the University of Žilina

SECTION 4

ELECTRIC POWER SYSTEMS
ELECTRICAL AND ELECTRONIC ENGINEERING

ŽILINA June 27 - 29, 2011
SLOVAK REPUBLIC

Edited by Milan Smetana, Peter Brída

ISBN: 978-80-554-0373-1

TRANSCOM 2011
9-th European conference of young research and scientific workers

TRANSCOM 2011, the 9-th international conference of young European researchers, scientists and educators, aims to establish and expand international contacts and co-operation. The main purpose of the conference is to provide young scientists with an encouraging and stimulating environment in which they present results of their research to the scientific community. TRANSCOM has been organised regularly every other year since 1995. Between 160 and 400 young researchers and scientists participate regularly in the event. The conference is organised for postgraduate students and young research workers up to the age of 35 and their tutors. Young workers are expected to present the results they had achieved.

The conference is organised by the University of Žilina. It is the university with about 13 000 graduate and postgraduate students. The university offers Bachelor, Master and PhD programmes in the fields of transport, telecommunications, forensic engineering, management operations, information systems, in mechanical, civil, electrical, special engineering and in social sciences.

SECTIONS AND SCIENTIFIC COMMITTEE

1. TRANSPORT AND COMMUNICATIONS TECHNOLOGY.

Scientific committee: Černý J. (CZ), Drozdziel P. (PL), Dydkowski G. (PL), Gašparík J. (SK), Havel K. (SK), Janáček J. (SK), Jánošíková Ľ. (SK), Kampf R. (CZ), Kavička A. (CZ), Kazda A. (SK), Novák A. (SK), Palúch S. (SK), Peško Š. (SK), Rievaj V. (SK), Šulgan M. (SK), Volek J. (CZ), Žarnay M. (SK), Žarnay P. (SK)

2. ECONOMICS AND MANAGEMENT.

Scientific committee: Bartošová V. (SK), Blašková M. (SK), Borkowski S. (PL), Březinová O. (CZ), Ďurišová M. (SK), Glebocki K. (PL), Graźulis V. (LT), Hittmár Š. (SK), Hrnčiar M. (SK), Kucharčíková A. (SK), Lyakin A. (RUS), Rostášová M. (SK), Rybakov F. (RUS), Seemann P. (SK), Strenitzerová M. (SK), Tomová A. (SK), Veretennikova B.O (RUS)

3. INFORMATION AND COMMUNICATION TECHNOLOGIES.

Scientific committee: Dado M. (SK), Diviš Z. (CZ), Drozdová M. (SK), Hudec R. (SK), Huotari J, (FIN), Keil R. (DE), Klimo M. (SK), Kolev P. (BG), Kotsopoulos S. (GR), Koudelka O. (A), Kováčiková T. (SK), Madleňák R. (SK), Matiaško K. (SK), Ranc D. (FR), Spalek J. (SK), Vaculík J. (SK), Vaculík M. (SK), Vrček N. (CR), Wieser V. (SK), Zábovský M. (SK)

4. ELECTRIC POWER SYSTEMS. ELECTRICAL AND ELECTRONIC ENGINEERING.

Scientific committee: Altus J. (SK), Blažek V. (DE), Brandstetter P. (ČR), Capolino G. A. (FR), Consoli A. (IT), Čápová K. (SK), Dobrucký B. (SK), Janoušek L. (SK), Luft M. (PL), Rusek S. (ČR), Szkutnik, J. (PL), Špánik P. (SK), Vittek J. (SK)

5. MATERIAL ENGINEERING. MECHANICAL ENGINEERING TECHNOLOGIES.

Scientific committee: Adamczak S. (PL), Bokůvka O. (SK), Dzimko M. (SK), Guagliano M. (I), Kunz L. (CZ), Meško J. (SK), Neslušan M. (SK), Nicoletto G. (I), Palček P. (SK), Skočovský P. (SK), Takács J. (H)

6. MACHINES AND EQUIPMENTS. APPLIED MECHANICS.

Scientific committee: Dekýš V. (SK), Gerlici J. (SK), Chudzikiewicz A. (PL), Jandačka J. (SK), Kalinčák D. (SK), Malenovský E. (CZ), Medvecký Š. (SK), Nemček M. (CZ), Sága M. (SK), Sitarz M. (PL), Szava I. (RO), Zapoměl J. (CZ), Žmindák M. (SK)

7. CIVIL ENGINEERING.

Scientific committee: Bujňák J. (SK), Ferrero A. M. (IT), Garbuz A. (UA), Horváth F. (HU), Ižvolt L. (SK), Melcer J. (SK), Petkova R. (BG), Plášek O. (CZ), Malachova A. (RU), Ungureanu V. (RO)

8. SOCIAL SCIENCES.

Scientific committee: Banáry B. (SK), Cabanová V. (SK), Grecmanová H. (CZ), Hádková M. (CZ), Kráľová Z. (SK), Larry Fast (USA), Lengyelfalusy T. (SK)

9. SECURITY ENGINEERING. FORENSIC ENGINEERING.

Scientific committee: Artamonov S. V. (RU), Burg H. (DE), Dudáček A. (CZ), Horák R. (CZ), Kasanický G. (SK), Klučka J. (SK), Leitner B. (SK), Navrátil L. (CZ), Podbregar I. (SLO), Poledňák P. (SK), Šimák L. (SK), Štofko S. (SK)

ORGANIZING COMMITTEE

CHAIRPERSONS Čelko Ján, Bokůvka Otakar

EXECUTIVE SECRETARY Vráblová Helena

MEMBERS Bača Tomáš, Bačová Katarína, Baďurová Silvia, Belan Juraj, Bomba Lukáš, Brída Peter, Brumerčík František, Gavláková Eva, Hampl Marek, Harušinec Jozef, Horváth Peter, Hrbček Jozef, Jošt Jozef, Kittel Ladislav, Kolla Eduard, Koniar Dušan, Kopas Peter, Landťák Milan, Lieskovský Anton, Mendrošová Katarína, Mišiaková Kvetoslava, Mokryš Michal, Mrvová Miroslava, Mužíková Karolína, Pácha Matěj, Peterková Andrea, Pilát Peter, Pitor Ján, Raždík Ján, Smetana Milan, Spuchľáková Erika, Šípek Michal, Šramová Veronika, Tengler Jiří, Tkáčová Gabriela, Vaško Alan, Vaško Milan, Vlček Jozef, Vrábel Ján, Vráblová Lucia, Závodská Anna, Zvaríková Katarína, Žiačková Vladimíra

SECTION 4 ELECTRIC POWER SYSTEMS. ELECTRICAL AND ELECTRONIC ENGINEERING

REVIEWERS:

Altus Juraj
Beňová Mariana
Brandštetter Pavel
Čáp Ivo
Dobrucký Branislav
Frívaldský Michal
Gála Michal
Gombárska Daniela
Janoušek Ladislav
Kállay Fedor
Pácha Matěj
Smetana Milan
Strapáčová Tatiana
Šimák Vojtech
Špánik Pavol
Vittek Ján

Note:

Authors are responsible for language contents of their papers

CONTENTS

Transcom 2011, 27-29 June 2011
University of Žilina, Žilina, Slovak Republic

Study of select parameters influencing the true penetration depth in eddy current NDT applications

Marcel Alman
University of Žilina, Faculty of Electrical Engineering, Department of Electromagnetic an Biomedical Engineering, Univerzitná 1, 01026 Žilina, Slovakia, marcel.alman@fel.uniza.sk

Abstract. This study evaluates influences of selected parameters on the true penetration depth of eddy currents in NDT applications by numerical means. Two different excitation coils are used to drive eddy currents in a conductive plate, respectively. Dimensions of coils, thickness of the plate as well as the excitation frequency are varied to explore the influences. The presented results reveal the existence of "optimal" exciting frequency for various material thicknesses to gain deepest penetration of eddy currents.

Keywords: excitation frequency, coil parameters, penetration depth, eddy current density distribution

1. Introduction

Eddy current testing is widely used for quality assurance of structural components made of conducting materials [1]. This method is suitable only to surface or near-surface flaw detection because of the decay in magnetic flux and in eddy current density with depth in the material as a result of the skin effect.

When a plane electromagnetic wave is incident perpendicularly on a conducting half-space, the skin effect is defined by the wave frequency and the electromagnetic parameters of investigated material. The depth in the material at which the eddy current density decreases to 36.9% of its surface value is known as the standard depth of penetration and is commonly used as a criterion for the eddy current inspection process:

$$\delta = \frac{1}{\sqrt{\pi f \mu \sigma}} . \qquad (1)$$

The standard depth of penetration decreases with increase in electric conductivity, magnetic permeability or testing frequency.. On the other side the true penetration depth, depends also on the investigated material thickness and the selected coil parameters [2].

One of the advantages of eddy current testing over the other non-destructive methods is maturity of computational techniques to simulate various modifications of testing system under real conditions without conducting a time consuming experiments. Author's earlier studies considered influences of various excitation coil parameters and of electromagnetic material parameters on eddy current density distribution along material depth [3] - [5]. Since conductivity and permeability of a material being tested are fixed, the only way to control penetration of eddy currents at different depths are through the excitation frequency and by selecting various excitation coil types and their dimensions.

The aim of this paper is to find out an optimal excitation frequency for different material thicknesses.

2. Numerical investigation

Numerical simulations using the finite element method are carried out to investigate influences of certain parameters on eddy currents distribution. Two excitation coils are utilized to drive eddy currents, respectively. Their configurations are shown in Fig. 1. The first one is of the circular shape and the second one of the rectangular shape. The coils are positioned as follows – circular coil in normal position and the rectangular coil in tangential position regarding the surface of a tested material.

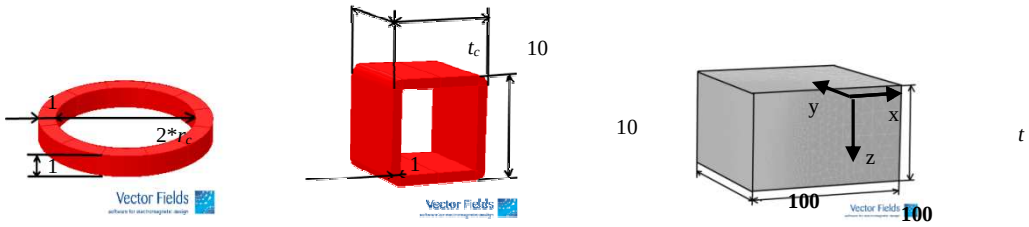

Fig.1. Numerical models of circular coil, rectangular coil and plate.

Electromagnetic parameters of a plate specimen being tested are those ones of the Inconel-600; σ = 1.0 MS/m, μ_r = 1. Dimensions of the specimen are shown in Fig. 1. The plate is without any defect. The coils are situated 1 mm above the surface of the specimen. Current density of the driving current is set to 1 A/mm^2.

Previous studies of the author concentrated on influences of the coils' dimensions (Fig. 1) on eddy current attenuation along the material depth [3, 4]. It was shown that for each coil in the particular position there is only one parameter among others that significantly influences the eddy current attenuation. In case of the circular coil in the normal position it is the coil radius r_c and in case of the rectangular coil in the tangential position it is the winding thickness t_c. Therefore influences of these parameters on eddy current attenuation along the material depth is further investigated here along with variations in the material thickness and in the excitation frequency. Parameters of the coils are adjusted as follows (see Fig. 1 for notations):

- circular coil: tc = 1 mm, wc = 1 mm, rc = 2, 3, 4, 5, 7, 10, 12, 15 mm,
- rectangular coil: lc = 10 mm, hc = 10 mm, wc = 1 mm, tc = 1, 2, 5, 10, 15, 20, 25, 30 mm.

Thickness of the material is changed as follows t = 5, 10, 20 and 30 mm.
Excitation frequency is varied in a wide range: f = 1 ÷ 500kHz.

First investigations are performed to find out an optimal excitation frequency considering variable material electromagnetic parameters and material thickness to gain deepest penetration of eddy currents. Then it is investigated to what extend do excitation coil parameter variations (circular coil – inner radius rc, rectangular coil – thickness of the winding tc) influence the true penetration depth in view of variable material thickness. To reduce size of the solved problem only ¼ of the plate is modelled with proper symmetry conditions.

;

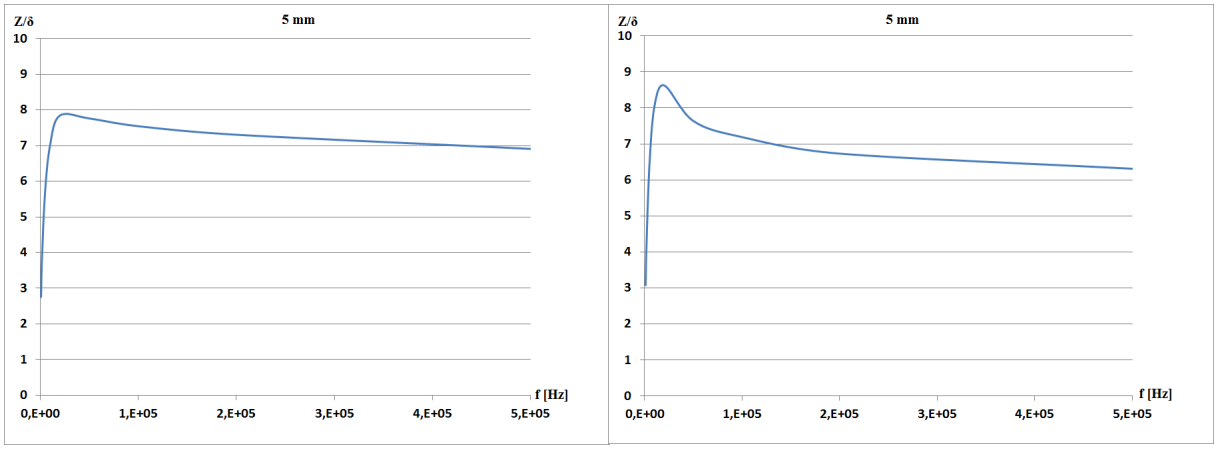

Fig.2. Dependence of a true penetration depth on the excitation frequency for the circular (left) and the tangential (right) coils in relative units and material thickness of 5mm.

The graphs shown in Fig.2 and Fig.3 display the frequency dependence of eddy current density attenuation depth for the plate with thicknesses of t = 5, 30 mm, respectively. Attenuation of eddy current density to 80% of its maximum value is considered here. Although, the standard depth of penetration considers attenuation to 36.9%, for some of considered cases such attenuation does not occur (thin material, low frequency) and for this reason the level of 80% is set. The depth at which this attenuation occurs is selected from simulated dependence of the eddy current density along the material depth and for easier comparison it is normalized by the appropriate standard depth of penetration.

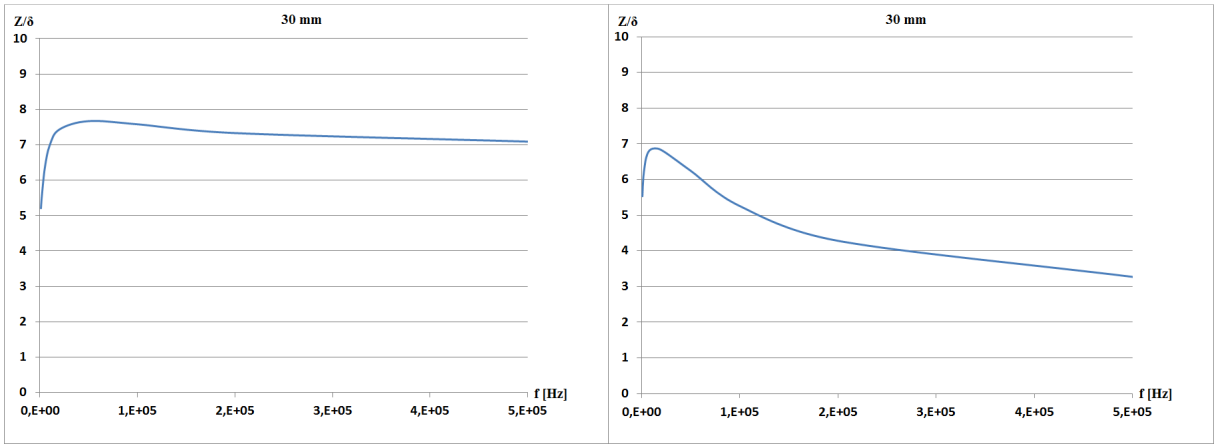

Fig.3. Dependence of a true penetration depth on the excitation frequency for the circular (left) and the tangential (right) coils in relative units and material thickness of 30mm

Based on the presented results it can be concluded that when a material with finite thickness is considered an optimum exciting frequency can be selected to gain the deepest penetration of eddy currents. Type of excitation coil and its spatial orientation influence the selection. For example for the plate with a thickness of 5mm the optimum excitation frequency is 20kHz for both the considered coils. When the plate with a thickness of 30mm is used in conjunction with a circular coil the optimum frequency is 50kHz, however, for the rectangular coil it is 15kHz.

Influence of selected parameters of excitation coils and of the material thickness on the eddy current penetration is studied here. Comparisons are carried out for the plate with thicknesses of t = 5,10,20 and 30mm, and for the two types of excitation coils. Selected dimensional parameters of the coils are changed to explore their influences on the eddy current penetration. Only those parameters are considered which have the most significant impact on the eddy current density distribution along the material depth [3] – [5], namely, according to the notation in Fig. 1, the radius r_c of the

circular coil in the normal position and the winding thickness l_c of the rectangular coil in the tangential position Frequency of the exciting signal is set to f = 10kHz

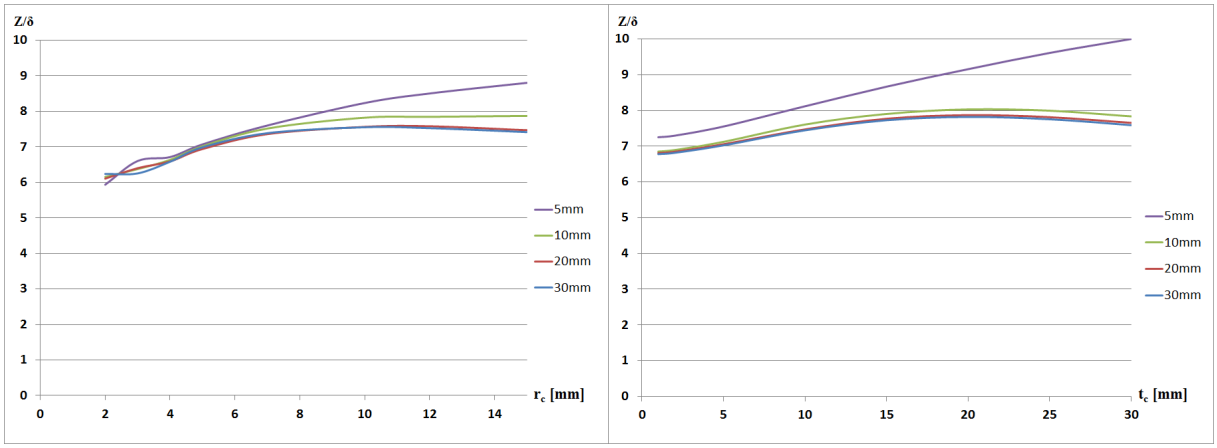

Fig.4. Dependence of eddy current penetration depth on inner diameter "rc" of the circular coil in normal position, winding thickness "lc" of the rectangular coil in tangential position and material thickness in relative units

Results of the numerical investigations are shown in Fig. 4. The charts display the dependence of eddy current penetration depth on the inner diameter "r_c" for the circular coil, and on the winding thickness "l_c" for the rectangular coil. The plate thickness is the parameter in this case and the y-axis corresponds to the material depth where the eddy current density is attenuated to 80% of its maximum value while it is normalized by the standard depth of penetration. From the presented results one can clearly conclude that the diameter of circular coil in the normal position has considerable impact on eddy current propagation for thin plates. When the thickness of a plate increases, the impact is reducing, especially when the plate thickness is higher than the standard depth of penetration. Similar conclusion is valid for the winding thickness of the rectangular coil when it is oriented tangentially.

3. Conclusion

Influences of selected excitation coils' parameters and of a material thickness on true penetration depth of eddy currents in non-destructive evaluation were investigated in this study. The aim was to find out an optimal excitation frequency for different coil types and variable material thickness. Two exciting coils were used to drive the eddy currents in a plate specimen made of the Inconel 600; the first circular coil in normal position and the second rectangular coil oriented tangentially regarding the surface of the plate. During the simulations excitation frequency and material thickness were altered. It has been clearly demonstrated that while using a circular and rectangular coils and 5mm thick plate the optimal excitation frequency is approximately 20kHz for both coils. When the plate with a thickness of 30mm is used in conjunction with a circular coil the optimal frequency is 50kHz; however, for the rectangular coil it is 15kHz.

Second part of the study compared the influence of selected parameters of excitation coils on eddy current penetration for different thicknesses of the material. It was shown that the diameter of a circular coil oriented normally to the material surface and the winding thickness of a rectangular coil in the tangential position has strong impact on eddy current penetration. However, this is valid only for materials with a thickness lower or comparable to the standard depth of penetration.

These facts should be helpful while using the eddy currents in NDT applications for specific material conditions or when designing an eddy current probes for certain applications to gain proper performances of the inspection.

;

Acknowledgement

This work was supported by the Slovak Research and Development Agency under the contract No. APVV-0194-07.This work was also supported by grant of the Slovak Grant Agency VEGA, project No. 1/0765/10.

References

[1] JANOUŠEK, L., ČÁPOVÁ, K., GOMBÁRSKA, D., SMETANA, M.: *Progress in eddy-current non-destructive evaluation of conductive materials*. In: ACTA TECHNICA CSAV, Vol. 55, No. 1, April 2010, ISSN 0001–7043, p. 13-28.

[2] Z. Mottl, The quantitative relations between true and standard depth of penetration for air-cored probe coils in eddy current testing. *NDT Intern* 23 (1990), pp. 11–18.

[3] Alman,M., Influence of basic excitation coil parameter variations in view of eddy current distribution in NDT applications, *IEEE Workshop Králíky 2009: proceedings*, Králíky – Czech Republic (2009), ISBN 978-80-214-3938-2, 22-26.

[4] Alman, M., Excitation coil parameters in view of eddy current distribution in ECT applications, *The 8th International Conference ELEKTRO 2010: proceedings*, Žilina – Slovak Republic (2010), ISBN 978-80-554-0196-6, 221-224.

[5] Alman, M., – Janousek, L.: Influence of excitation coil parameters and material thickness variations on eddy current distribution in ECT applications. In CPEE 2010: Proceedings of the International Conference on Computational Problems of Electrical Engineering: proceedings. Lázne Kynžvart: University of West Bohemia, 2010. ISBN 978-80-7043-899-2, p.10

Transcom 2011, 27-29 June 2011
University of Žilina, Žilina, Slovak Republic

Influence of extremely low frequency electromagnetic fields on *Saccharomyces Cerevisiae* growth

[*]Jan Barabas, [*]Ivo Cap
[*]University of Zilina, Faculty of Electrical Engineering, Department of Electromagnetic and Biomedical Engineering, Univerzitna 1, 01026 Zilina, Slovakia, {jan.barabas, ivo.cap}@fel.uniza.sk

Abstract. The following article details experimental findings in the proliferative response of *Saccharomyces cerevisiae* following exposure to low frequency electromagnetic (EM) field. Yeast samples have been subjected to 66 hour session of EM exposure (frequency 1,6 kHz, magnetic flux density 2mT) under identical ambient conditions. The results indicate a pronounced anti-proliferative effect of the said fields on the exposed samples. The observed proliferative response might hint at frequency-selective behavior and/or induced intracellular current-dependent response and warrants further research in this area.

Keywords: low frequency electromagnetic fields, exposure, proliferation, yeast, *Saccharomyces cerevisiae*.

1. Introduction

Recent technological evolution has caused a dramatic increase of man-made electromagnetic fields (EMF) in our biosystem. While undoubtedly being beneficial to mankind, these newly introduced phenomena, commonly referred to as electromagnetic pollution, might also pose a problem for living organisms which developed and adapted to a relatively EM-free environment. In view of this uncertainty, the International Agency for Research on Cancer (IARC), a subsidiary of World Health Organization (WHO), has classified low frequency magnetic fields as group 2B carcinogens - considered possibly carcinogenic to humans [1].

However, a controlled use of these fields might also be beneficial in various medical areas, including, but not limited to cancer therapy. To this end, plain baker's yeast has been employed as a model organism for cancer research and use thereof in various experiments seems plausible when studying the fundamental aspects of cell biology. Resources are now available for yeast that enhance investigations, such as the presence of strains with each gene deleted, each protein tagged and databases on protein-protein interactions, gene regulation, and subcellular protein location. When considering an analogy to human cancer, numerous cellular processes that are present in the mammalian cell are also present in a simplified form in yeast cells. Nonetheless, yeast cells are considered to be a key to elucidating mechanisms and identifying the key players in cellular processes. Armed with this information, cancer cell biologists can investigate the analogous pathway in the far more complex and elaborate system of the mammalian cell. Of interest are especially the tumourigenic properties of cancer cells, the indefinite division of cells and yeast may help in the quest to slow down or even reverse this process [2].

2. Materials and methods

2.1. Exposure apparatus

The exposure apparatus consists principally of an incubator, exposure coil, shielding box, signal generator and an amplifier. The incubator allowed for identical exposure conditions of both the exposed and control samples. Fig. 1 shows a simplified scheme of the incubator. Temperature sensors were placed at locations marked with a green dot and fans at locations marked with a yellow dot. The purpose of the fans was to drive cool air into the exposure chamber to cool the

exposed samples/coil and then via the control chamber. The magnetic bias introduced into the system due to the fans/other equipment was approximately six orders of magnitude less than the 2mT generated by the coil. With this setup the mutual average temperature ΔT_m between the exposed and control samples never exceeded ±0.2 ˚C (experimentally verified and recorded over a period of 72 hours).

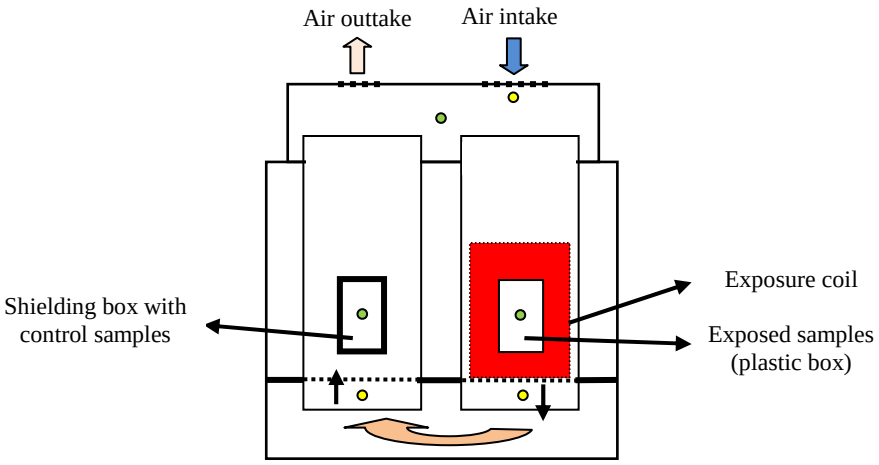

Fig.1. Incubator schematic representation

The coil was manufactured from a PVC tube (outer diameter 167mm, inner diameter 154mm, coil length 150mm) using a chasing lather to create the necessary thread to place the 0.9 mm copper wire, wound in 2 layers (100 turns per layer). A small plastic holder was inserted into the coil core in order to optimally position the plastic box (i.e. in the coil center) containing the exposed samples. Proper functioning of the coil was evaluated using a sensitive flux-gate sensor placed in the center of coil which was then powered by a low-amplitude driving signal (in order not to saturate the sensor) – the measured value was then compared to the theoretically calculated value and only a minor deviation was found (±50 μT).

During the course of the experiment the control samples were kept in a grounded shielding box. The said box was manufactured from 6 mm steel plates welded together, with a higher amount of nickel component to allow for higher magnetic permeability. The box was additionally shielded using a multilayer aluminum sheet, especially at the top box cover. A sensitive flux-gate sensor was once again used to measure the variations in magnetic flux density within the box when placed near the operating coil. Results indicate minimum change in magnetic flux density, on average six orders of magnitude lower than those within the exposed samples plastic box. Humidity was also evaluated post-experiment within both boxes using hydrosensitive paper cards and was identical in both boxes.

2.2 Yeast samples

Baker's yeast VIVO, distributed by LESAFFRE Slovensko, a.s.[3] has been used in the experiment. The shape has been experimentally verified using a microscope (fig.2a) and was found to be circular. After experimentally finding the optimal dilution factor, sixteen Petri dishes were inoculated in a sterile environment – 8 controls and 8 exposed samples, per dilution type. The agar used was GKCH – chloramphenicol yeast glucose agar, manufactured by Imuna, Šarišské Michaľany, Slovakia which is used for cultivation of yeasts and moulds. The purity of the used materials and inoculation procedure was assured by using a control Petri dish. The Petri dishes were then placed into the control and shielding boxes and inserted into the incubator (fig.2b).

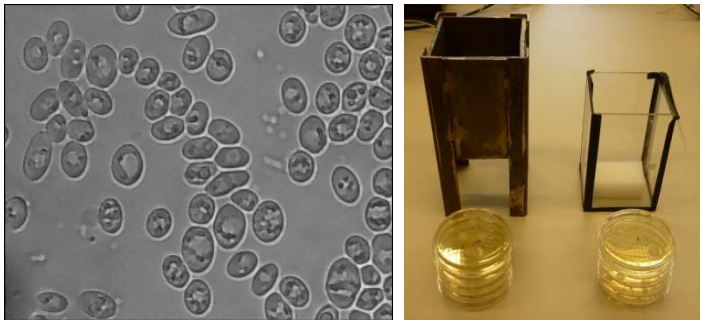

a) b)

Fig. 2. a) Shape of used yeast samples, b) Shielding box (left) for control samples and plastic box for exposed samples

2.3 Evaluation methods

Two different quantities were observed post-exposure – the number of colony forming units (CFU) per dish and the area that the said CFU's take up on all petri dishes (in units relative to the scanned data file). Results were consulted by a professional researcher[1], however later results were processed using in-house developed GUI application (*PetriCounter*) to ease the evaluation. The Petri dishes have been inserted into a 2x2 matrix placed atop a conventional flat-bed scanner and scanned at 200DPI resolution as 8bit grayscale image, fig.3a. The image was then processed in the said software (fig.3b) programmed in MATLAB R2010a environment and consisted of various image transformations and mathematical functions in order to obtain the desired output values. The low overall error rate, when compared to professional evaluation, made the software an excellent evaluation tool for our purpose.

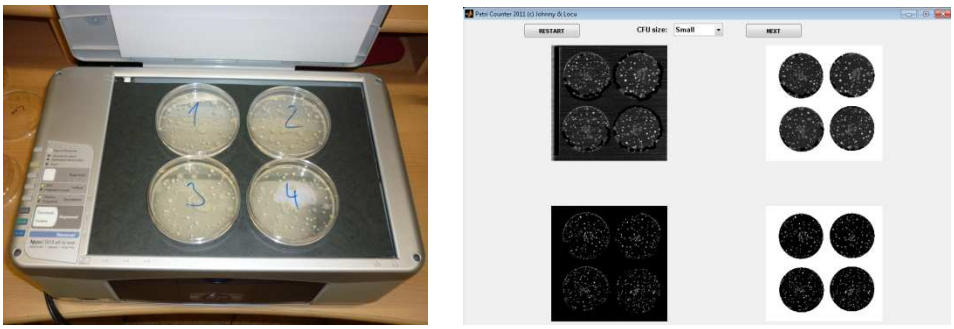

a) b)

Fig. 3. Petri dishes placed in scanner (a), developed PetriCounter software (b)

2.4 Experiment protocol and results

The inoculated Petri dishes were inserted into the pre-heated incubator (unit was running 2 hours prior experiment start in order to assure equal and stable temperature of both boxes) and the experiment executed for 66 consecutive hours. The harmonic 1,6 kHz driving signal was generated using a signal generator (Agilent 33220A) and amplified using an amplifier. The resulting driving current flowing into the exposure coil was 2A and the resulting magnetic flux density in the center of the coil was 2mT. Petri dishes were positioned in such a way that maximum magnetic flux density was achieved along the center axis of the petri dishes. A total of two sessions were executed, each containing 16 Petri dishes (8 controls, 8 exposed) and the results were evaluated using the already mentioned *PetriCounter* software and statistically processed. For the statistical analysis of the results the Student's t-test was used (P=0.95).

[1] Maria Barabasova, VUM, Zilina, Slovakia

2.4.1 CFU counts

Colony forming units were counted immediately post-exposure using the previously described software. The total CFU count was calculated from eight Petri dishes per dilution and a ratio was established between exposed and control samples.

	PETRI DISH n.								
	1	2	3	4	5	6	7	8	$\frac{\sum n(exp.)}{\sum n(cont.)}$
Source (dilution)	*exp. / cont.*								
LESAFFRE (7)	*139/127*	*138/141*	*104/129*	*116/142*	*142/130*	*135/137*	*110/135*	*120/140*	***0.93***
LESSAFFRE (8)	*18/21*	*15/25*	*12/17*	*12/16*	*17/21*	*16/23*	*13/19*	*14/17*	***0.74***

Tab. 1. CFU counts per petri dish (exposed/controls) and ratio ∑n(exposed)/ ∑n(controls)

A paired t-test was performed on the collected data. For dilution n.7 the mean CFU difference (Mean=9.625, Standard Deviation=16.414, N=8, t(7)=1.659, two-tail p=0.141) was lower than of dilution n.8 (M=5.250, SD=2.375, N=8, t(7)=6.251, two-tail p=0.000).

2.4.2 Growth dynamics

Yeast growth dynamics were evaluated immediately post-exposure using the previously described software. The yeast-occupied area was calculated from eight Petri dishes per dilution and a ratio was established between exposed and control samples.

	PETRI DISH n.								
	1	2	3	4	5	6	7	8	$\frac{\sum n(exp.)}{\sum n(cont.)}$
Source (dilution)	*exp./cont.*								
LESAFFRE (7)	*18988/36501*	*20631/39692*	*18252/44859*	*19930/38120*	*19420/43215*	*20863/39210*	*18790/39102*	*18977/37124*	***0.49***
LESSAFFRE (8)	*5278/7907*	*6264/11340*	*3426/12039*	*3751/10016*	*5811/10036*	*5970/11756*	*4210/11740*	*4158/11012*	***0.45***

Tab. 2. Yeast growth area per petri dish (exposed/controls) and ratio ∑n(exposed)/ ∑n(controls)

A paired t-test was performed on the collected data. A statistically significant mean area difference was observed for both dilutions:

- dilution n.7 : M=20247, SD=3255, N=8, t(7)=17.592, two-tail p=0.000,
- dilution n.8 : M=5872, SD=1899, N=8, t(7)=8.745, two-tail p=0.000.

3. Discussion

The experimental data has shown interesting results. When taking into account the EMF sensitivity in view of CFU counts, the yeast strand VIVO has responded by a significant decrease of the number of CFU's, which also correlates with the calculated ratio (tab.1). An even more pronounced difference was observed in the growth dynamics, wherein almost a two-fold difference in growth dynamics has been observed, when compared to the controls (tab.2). The chosen dilution factor does not seem to play an important role in the above-discussed findings and as such further investigation will no longer introduce this variable.

Two currently known variables are to be considered when interpreting the findings - specific target-frequency of particular organisms, perhaps suggesting the presence of an endogenous electromagnetic field(s) that plays a seemingly important role in the multiplication and overall growth process of the said organisms, and also the magnitude of induced cellular currents, regulating the intricate transmembrane transport mechanism. The former would fit the theory of

coherent oscillations postulated and pioneered by H. Fröhlich [4], while the latter stems from electromechanic analogy of the cell model, collectively known as the Hodgkin–Huxley cell model and the associated Goldman equation [5].

It is the opinion of the authors that the above findings warrant a more in-depth research and as such would at least partially elucidate the intricacies of electromagnetic field effects on living systems.

References

[1] IARC Monographs - agent classification, http://monographs.iarc.fr/ENG/Classification/, available online 25.3.2011

[2] NITISS, J., HEITMAN, J. *Yeast as a tool in cancer research*, Springer, 2010, ISBN 978-1402059629

[3] Testing protocol – LESAFFRE - VIVO, http://www.lesaffre.sk/content/file/protokol-o-skuske---vivo.pdf, available online 25.3.2011

[4] S. J. WEBB, M. E. STONEHAM, H. FRÖHLICH "Evidence for non-thermal excitation of energy levels in active biological systems" Physics Letters A, vol. 63, pp. 407, 1977

[5] FALL, CH. Computational Cell Biology, Springer, 2002, ISBN 978-0387953694

Transcom 2011, 27-29 June 2011
University of Žilina, Žilina, Slovak Republic

Permanent Magnet Synchronous Motor Loss Minimization

[*]Zdeno Biel
[*]University of Zilina, Faculty of Electrical Engineering, Department of Power Electrical Systems,
Univerzitna 1, 01026 Zilina, Slovakia, Zdeno.Biel@kves.uniza.sk

Abstract. This paper describes loss minimization method for the drives with permanent magnet synchronous motor. Electrical losses, which consist of copper losses and iron losses, can be minimized by appropriate control of stator current vector. Such current control exploits reluctance torque and field weakening. Method itself is based on d, q equivalent circuit taking into account iron losses. The loss minimization method is implemented in speed vector control structure and verified by simulation.

Keywords: Permanent magnet synchronous motor, Loss minimization, Efficiency, Equivalent circuit.

1. Introduction

Electrical drives with permanent magnet synchronous motors (PMSM) are widely used in industrial applications and as a traction drives. Their main advantages in comparison with induction machines are higher efficiency, higher power factor, higher power density and wide speed range.

Nowadays particular emphasis is addressed towards energy saving, which include also electricity. Especially continuously operating electric drives consume a significant quantity of electricity. Even a small increasing in drive efficiency can therefore yield significant energy saving. If the motor is operating with constant speed and constant load, losses can be minimized by appropriate design of the motor operational mode. This isn't valid for motors operating at variable speed and load torque. In this case, it is possible to reduce motor losses by optimal management of the stator current space vector.

This paper describes a method for minimizing electrical losses of PMSM. The method is based on the d, q axis equivalent circuit of PMSM, which takes into account the iron losses. The value of direct axis current, i_d is controlled in order to achieve maximum efficiency in contrary to traditional control strategy, in which the i_d is controlled to be zero ($i_d = 0$). The reluctance torque and field weakening are utilized to minimize the losses.

2. PMSM d, q Axis Equivalent Circuit with Iron Losses

Dynamic d, q axis equivalent circuit of PMSM taking into account iron losses is shown in Fig. 1. Iron losses consist of hysteresis losses and eddy current losses. These losses are represented by resistance R_C. The second and significant component of the total electrical losses are copper losses in stator winding resistance, R.

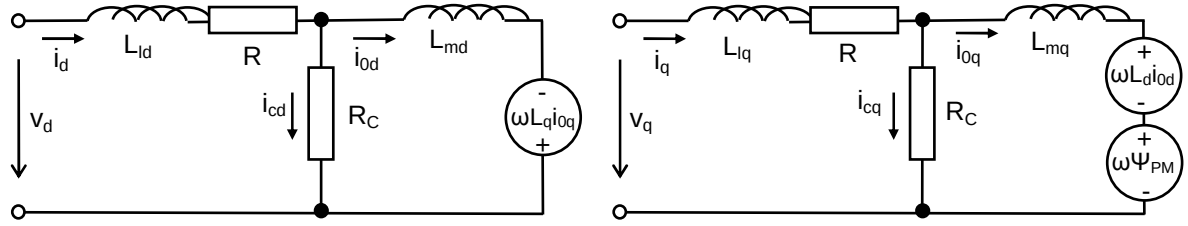

Fig. 1. Dynamic d, q axis equivalent circuit of PMSM taking into account iron losses.

PMSM dynamic model, which take into account iron losses, is described in d_q rotating frame coupled with the rotor as follows:

$$\frac{di_d}{dt} = \frac{1}{L_{ld}}\left(v_d - Ri_d - L_{md}\frac{di_{0d}}{dt} + L_q p\omega_r i_{0q}\right) \quad (1)$$

$$\frac{di_q}{dt} = \frac{1}{L_{lq}}\left(v_q - Ri_q - L_{mq}\frac{di_{0q}}{dt} - L_d p\omega_r i_{0d} - \Psi_{PM} p\omega_r\right) \quad (2)$$

$$\frac{d\omega_r}{dt} = \frac{1}{J}(T_E - T_L) \quad (3)$$

Equations (1) and (2) are derived from the equivalent circuit. Equation (3) is the motor mechanical equation. Currents, i_d, i_q and electromagnetic torque, T_E ere expressed as:

$$i_d = i_{0d} + i_{cd} = i_{0d} + \frac{-\omega L_q i_{0q} + L_{md}\frac{di_{0d}}{dt}}{R_c} \quad (4)$$

$$i_q = i_{0q} + i_{cq} = i_{0q} + \frac{\omega(\Psi_{PM} + L_d i_{0d}) + L_{mq}\frac{di_{0q}}{dt}}{R_c} \quad (5)$$

$$T_E = \frac{3}{2}p\left[\Psi_{PM} i_{0q} + (L_{md} - L_{mq}) i_{0d} i_{0q}\right] \quad (6)$$

R – stator winding resistance
R_c – iron loss resistance
L_d, L_q – d_q axis inductances
L_{ld}, L_{lq} – d_q axis leakage inductances
L_{md}, L_{mq} – d_q axis magnetizing inductances
J – rotor inertia
Ψ_{PM} – permanent magnet rotor flux
T_E – electromagnetic torque
T_L – load torque
ω_r – rotor mechanical angular speed
i_d, i_q – d_q axis current components
v_d, v_q – d_q axis voltage components

From (6) can be seen that the electromagnetic torque consists of two terms. The first term is a synchronous torque, which is proportional to the current i_{0q}. The second term is the reluctance torque, which is proportional to the product of i_{0d} and i_{0q}. The reluctance torque is equal to zero if surface mounted permanent magnets are used. In this case L_d=L_q, or the same is valid for control with i_d=0. To exploit the reluctance torque, d-axis current must be different from zero and interior permanent magnets for which L_d< L_q, must be used. Reluctance torque then can be used to minimize PMSM losses.

3. Strategy for Loss Minimization

Loss minimization strategies are described in [1], [2], [3]. These methods are based on (8) which express the electrical losses as a function of i_d, T_E, ω. The total electrical losses are expressed in (7), where W_{Cu} are copper losses and W_{Fe} are iron losses.

$$W_E = W_{Cu} + W_{Fe} = \frac{3}{2}R\left(i_d^2 + i_q^2\right) + \frac{3}{2}R_c\left(i_{cd}^2 + i_{cq}^2\right) \quad (7)$$

Currents i_q, i_{cd}, i_{cq} can be also expressed as a function of i_d, T_E, ω by (4), (5), (6). After substituting into (7) we can expressed the total electrical loss as a similar function:

$$W_E(i_d, T_E, \omega) = W_{Cu}(i_d, T_E, \omega) + W_{Fe}(i_d, T_E, \omega) \quad (8)$$

In steady-state the motor torque, T_e and speed, ω are constant. Then the total electrical losses depend only on the value of i_d. Fig. 2 shows the total electrical losses W_E, copper losses W_{Cu} and iron losses W_{Fe} as a function of i_d at the rated speed and the rated torque. The motor parameters are listed in Tab. 1.

n_N	2000 rpm	R_c	280 Ω
T_N	2.5 Nm	L_d	10.87 mH
p	4	L_q	21.32 mH
R	1.28Ω	Ψ_{PM}	0.124 Wb

Tab. 1. PMSM parameters

From Fig. 2 can be seen that total electrical losses are minimal for some negative value of i_d current. If the current, i_d is controlled to this value the efficiency for given motor speed and load torque has highest value. The value of this optimal current, i_{dopt} is a function of the speed and torque. Therefore it is necessary to express the current, i_{dopt} as such function. Analytical solution can be obtained via fourth-order equation, which is not suitable for real time control.

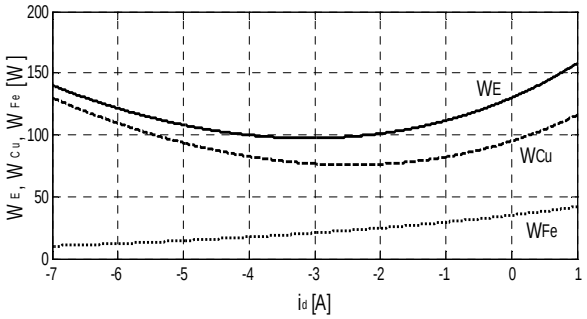

Fig. 2. Electrical losses W_E, copper losses W_{Cu} and iron losses W_{Fe} as a function of i_d at rated speed and torque.

Polynomial approximation, where i_{dopt} as a function of i_q is expressed is described in [1]. The coefficients of polynomial for various speeds are then stored in table form. Optimal d axis current is calculated from (9):

$$i_{dopt} = K_0 + K_1 i_q + K_2 i_q^2 \tag{9}$$

Another way to determine i_{dopt} for the given speed and torque is described in [2]. An algorithm that searches for the minimum of the function (8) is used to find corresponding value of current i_{dopt}. This method is verified by simulation for PMSM with parameters listed in Tab. 1.

4. Simulation Verification

The simulations uses block diagram of vector controlled PMSM with implementation of the loss minimization algorithm shown in Fig. 3.

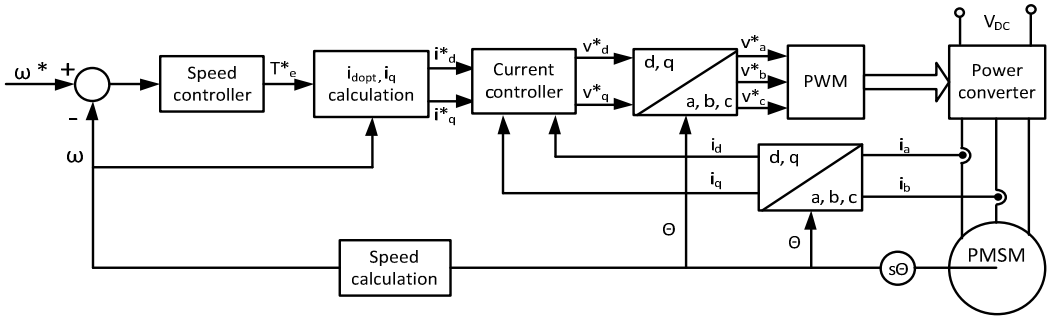

Fig. 3. Block diagram of PMSM vector control with implementation of the loss minimization algorithm.

In Fig. 4. (a) the efficiency as a function of speed for control with i_d=0 and loss minimization control, i_d=i_{dopt} is shown. Fig. 4. (b) shows the efficiency as a function of load torque. These figures confirm the efficiency increase by 8% at the rated speed and rated torque.

Fig. 5. (a) shows the total electrical losses as a function of time for i_d=0 and loss minimization control, i_d=i_{dopt}. Again the reduction of losses is confirmed if the loss minimization algorithm is used. Rated speed of PMSM was reached at t=0.2 s. Then the load torque increases to its nominal

value 2.5 Nm at t=0.5 s. Time functions of currents, i_d, i_q for loss minimization control are shown in Fig. 5. (b).

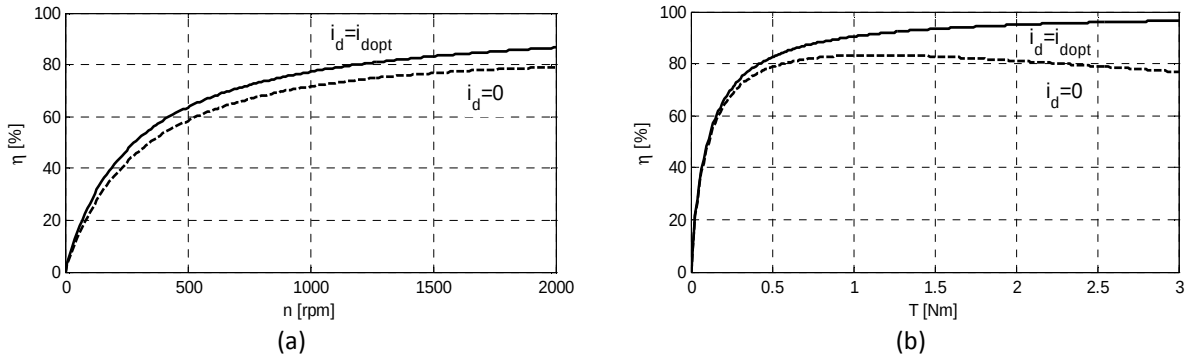

Fig. 4. Motor efficiency as a function of the speed (a) and load torque (b).

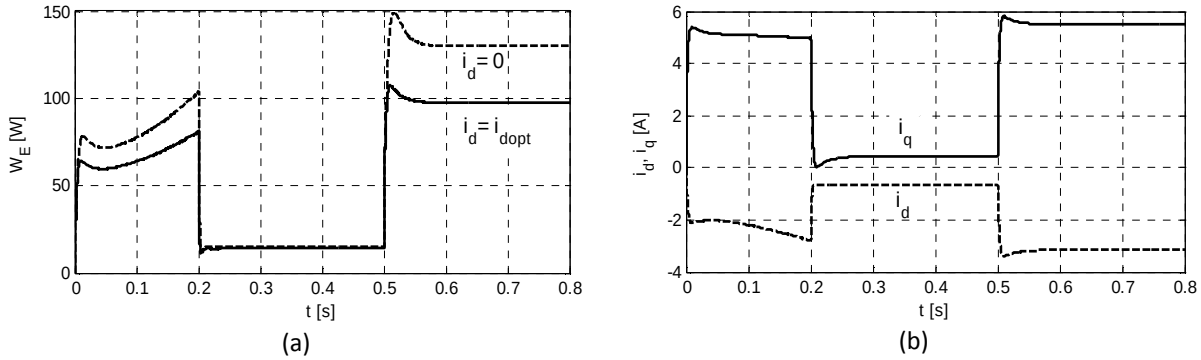

Fig. 5. Total losses as a function of time for $i_d=0$ and $i_d=i_{dopt}$ (a) and i_d, i_q currents (b).

5. Conclusion

In this paper loss minimization strategy of PMSM has been described and validated by simulation. This loss minimization strategy is based on equivalent circuit of PMSM, which takes into account iron losses. Simulation results confirmed the increase of efficiency by 8%. This method is efficient mainly for interior permanent magnet synchronous motor, in which the reluctance torque is exploited.

Acknowledgement

The authors wish to thank for support the Slovak Grant agency VEGA.

References

[1] MORIMOTO, S., TONG, Y., TAKEDA, Y., HIRASA, T. *Loss minimization control of permanent magnet synchronous motor drives*, IEEE Transaction on Industrial Electronics, No. 5, October 1994

[2] CAVALLARO, C., DI TOMMASO, A. O., MICELI, R., RACITI, A., RICCO GALLUZZO, G., TRAPANESE, M. *Analysis a DSP implementation and experimental validation of a loss minimization algorithm applied to permanent magnet synchronous motor drives*, IEEE Industrial Electronic Society, April 2004

[3] ODVÁŘKA, E., ONDRŮŠEK, Č. *Evaluation of control strategies for permanent magnet synchronous machines in terms of efficiency*, Recent Advances in Mechatronics 2008 - 2009

Transcom 2011, 27-29 June 2011
University of Žilina, Žilina, Slovak Republic

Study of structural properties of transformer oil based magnetic fluids using ultrasound spectroscopy

*Jozef Drga, *Jozef Kúdelčík, *Peter Bury
* University of Žilina, Faculty of Electrical Engineering, Department of Physics, Univerzitná 1, 01026 Žilina, Slovakia, drga@fyzika.uniza.sk

Abstract. This work deals with the experimental investigation of magnetic fluids by the acoustic absorption coefficient measurement as a function of external magnetic field. The experimental arrangement is described and the measured effect of the external magnetic field and time of application on the magnetic fluids is discussed.

Keywords: magnetic fluid, acoustic spectroscopy.

1. Introduction

Transformer oils have in transformers two main functions – electrical insulation and cooling. Cooling and insulation of transformer oil significantly increases the transformer performance [1]. However, transformer oils have small thermal conductivity and cooling is thus less efficient. A solution can be to use a magnetic fluid based on transformer oils [2]. Magnetic fluids are colloidal suspensions of magnetic particles covered by a surfactant layer in a carrier liquid, in our case in transformer oil ITO 100. The magnetic particles are usually ferrites (formula MFe2O3, where M represents Co, Fe, or Ni). The particles' diameter is about 1 -10 nm and each particle is a magnetic monodomain. In an external magnetic field the magnetic particles form clusters with length of about 10 – 100 nm. Magnetic particles in the fluid increase thermal conductivity [3] and dielectric constant [2]. However, aggregation of particles can induce electric breakdown [4]. The surfactant function is to prevent the aggregation of particles. A surfactant molecule consists of a polar head and a no polar tail. The polar head takes up on the magnetic particle. Oil acid is a most frequently used surfactant.

A useful method for studying structural changes in magnetic fluids due to the magnetic field on temperature is the measurement of the attenuation change of an ultrasonic wave in a magnetic fluid. In the present study the magnetic fluid based in the transformer oil ITO 100 is investigated by ultrasonic spectroscopy to study the influence of magnetic field on the its structure. The effect of time of the external magnetic field application was analyzed, too.

2. Experimental arrangement

The block diagram of the experimental arrangement is shown in Fig. 1. The measurements of the changes of the absorption coefficient of the ultrasound wave of frequency 5,86 MHz were carried out by a pulse method using the MATEC Pulse Modulator and Attenuation Recorder [5]. An ultrasound wave propagating in the measured cell (1.5 x 1 x 1 cm3) inserted in an electromagnet undergoes a multiple reflection from the transducers and its subsequent echoes are recorded. Two selected adjacent pulses following separate paths reach a detector from where signals proportional to their amplitudes are fed to the MATEC receiver. The signal from the MATEC, which is proportional to the changes of the acoustic wave absorption coefficient in the magnetic fluid, was recorded by oscilloscope and measured by a computer program [6]. We use 1,5% magnetic fluid

based on ITO 100 inhibited transformer oil. The magnetic particles had the mean diameter 10,6 nm. The speed of ultrasound in magnetic liquid without external magnetic field is c = 1524 m/s (20 ºC).

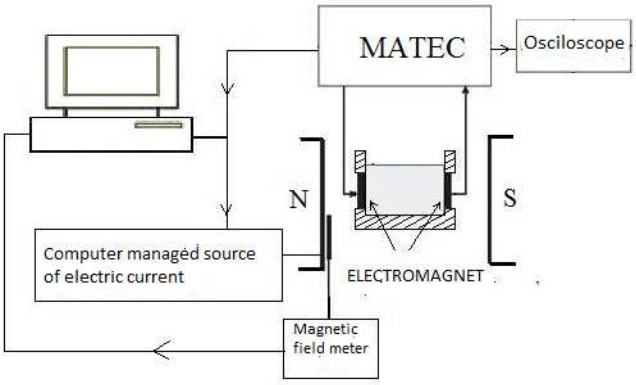

Fig.1. Experimental setup.

3. Results and discussion

In Fig. 2 we show the absorption coefficient change as a function of magnetic field *B* that is parallel to *k*. In this figure we compare two measurements of the magnetic fluid with magnetic field exposure to 133 mT (circles) and 200 mT (squares) with linear increase of the magnetic field of 2,27 mT per minute up to its maximum value.

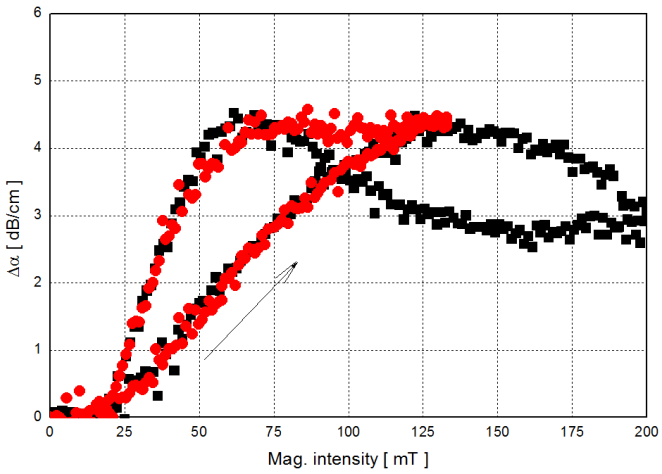

Fig. 2. Dependence of absorption coefficient change on magnetic field.

These results show a strong influence of the magnetic field on the ultrasound wave absorption coefficient. With increasing magnetic field, the change of ultrasound wave absorption increases. When the magnetic field is swept at a constant rate, the interactions between the external magnetic field and the magnetic moment of the magnetic nanoparticle leads to the aggregation of particles and clusters are formed (structures as long as hundreds of nanometers [7]). This effect causes the increase of the absorption of ultrasound wave with increasing external magnetic field the saturation of which is about ~130 mT. The next increase of magnetic field under 130 mT leads to probably the mutual connection of clusters the result of which is lower concentration and resulting decrease of acoustic absorption. The character of absorption coefficient changes continues with decreasing magnetic field. In spite of the fact that magnetic field decreases the started process continue up to

approximately 130 mT. Then the process is opposite, so that the changes of the acoustic wave absorption coefficient show a hysteresis. This effect can be described by existence of clusters, which lifetimes were smaller than time of decrease of the magnetic fluid. The structure return to the initial state immediately after the magnetic field has been removed.

Investigating the transformer oil based magnetic field in the range 0 – 200 mT we observe two basic mechanisms. The absorption coefficient change increases with the increasing magnetic field generally to a maximum value (133 mT in both the 1st and 2nd case). This is connected to the aggregation of the magnetic particles into clusters. Decreasing the absorption coefficient change after reaching its maximum value can be due to the dilution of the fluid as a consequence of the agglomeration of the clusters into longer structure. When the magnetic field is decreasing, we observe hysteresis. This is related to the presence of the clusters and to the continuing agglomeration of the magnetic particles into clusters during the magnetic field decrease. A second maximum was observed at 65 mT in the 2nd case. After the magnetic field decreased below the above value, the absorption coefficient decreased as well. This is caused by the disintegration of the formed clusters. This disintegration is caused by the thermal Brown motion.

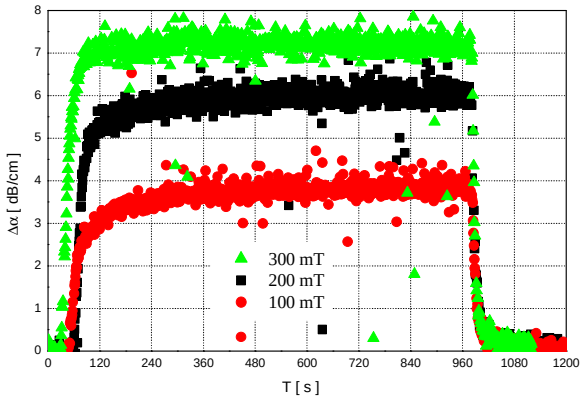

Fig. 3. Time dependence of absorption coefficient change for pulse changes of magnetic field.

Fig. 3. presents the coefficient of the acoustic absorption change for three pulse changes of the magnetic field: 300 mT (triangles), 200mT (squares) and 100 mT (circles). At the beginning of the measurement the magnetic field was set to zero value and after that occurred its pulse change. The magnetic field was held at a constant value for 15 minutes. The change of the absorption coefficient occurred practically in quite short time. It can be seen that after 120 seconds the change of the absorption coefficient was fixed. After magnetic field switch off, the change of the acoustic absorption coefficient decreased exponentially with a relaxation constant about 10 seconds. This means that the clusters practically immediately disintegrated by the thermal Brown motion.

4. Conclusion

Acoustic spectroscopy is a very useful tool for the investigation of magnetic fluids. We studied the change of the acoustic absorption coefficient of the magnetic fluid based on ITO 100 inhibited transformer oil. The coefficient of the acoustic absorption change depends on the magnetic field strength and reflect the diameter and the concentration of clusters formed from the magnetic particles. For a detailed study of the properties of the magnetic fluids additional measurements are needed.

References

[1] ZHANG, J., LI, X., VANCE, M. *Experiments and modeliung of heat transfer in oil transformer winding with zigzag cooling ducts*, Applied Thermal Engineering, Vol 28, p. 36 - 48, 2008.

[2] SEGAL, V., RABINOVICH, A., NATTRASS, D., RAJ, K., NNUNES A. *Experimental study of magnetic colloidal fluids behavior in power transformers*, J. Magn. Magn. Mater, Vol 215-216, p. 513 – 515, 2000.

[3] CHOI, C., YOO, H. S., OH J. M. *Preparation and heat transfer properties of nanoparticle-in- transformer oil dispersions and advances energy-efficient coolants*, Current Applied Physics, Vol. 8, p. 710 - 712, 2008.

[4] HERCHL, F., KOPČANSKÝ, P., TIMKO, M., KONERACKÁ, M., MARTON, K., KOLCUNOVA, I., TOMČO, L. *Dielectric properties of magnetic liquids in high electric fields*, Acta Phys. Pol. A., Vol. 113, p. 569 – 572, 2008.

[5] BURY, P., HOCKICKO, P., JAMNICKÝ, I. *Transport and relaxation study of ionic phosphate glasses*, Adv. Mater. Research, Vol . 39, p. 111 – 116, 2008.

[6] KÚDELČÍK, J., BURY, P., ZÁVIŠOVÁ, V., TIMKO, M., KOPČANSKÝ, P. *Acoustic spectroscopy of magnetic fluid based on transformer oil*, Acta Electrotechnica et Informatica, Vol. 10, No 3, p. 90 - 92, 2010.

[1] [7] KOPČANSKÝ, P., TOMČO, L., MARTON, K., KONERACKÁ, M., TIMKO, M., POTOČOVÁ, I. *The DC dielectric breakdown strength of magnetic fluids based on transformer oil*, J. Magn. Magn. Mater., Vol. 289, p. 415 – 418, 2005.

Transcom 2011, 27-29 June 2011
University of Žilina, Žilina, Slovak Republic

Calibration of Resolver Sensor Using Ellipse Fitting Technique

[*]Ján Faber, [*]Ján Vittek, [*]Peter Minárech
[*]University of Žilina, Faculty of Electrical Engineering, Department of Power Electrical Systems,
Univerzitna 1, 010 26 Žilina, Slovakia, {Jan.Faber, Peter.Minarech}@kves.uniza.sk; Jan.Vittek@fel.uniza.sk

Abstract. In servo drives resolvers are used as sensors for position and speed measurement to obtain feedback signals for controllers. Measurement accuracy is limited mainly by sensor's signals errors such as different magnitudes, dc drifts and quadrature error. Estimation of the resolver error parameters can be formulated in terms of ellipse fitting problem, which is in this paper exploited for auto-calibration algorithm. Recursive least square estimation is used to find characteristic ellipse of the resolver. Estimated error parameters are consequently used for sensor line signals correction to improve accuracy of position measurement. Proposed method does not require any additional hardware. Performance of the correction algorithm is verified by simulation and the presented results confirm improvement of position measurement.

Keywords: Resolver sensor, ellipse fitting, recursive least squares, calibration, measurement accuracy.

1. Introduction

For precise motion control the quality of speed and position feedback is the most relevant for achieving high performance. Resolver has proven to be robust and reliable position sensor because of its ability to operate in severe and hostile environment. In considered application, the resolver sensor feeds rotary position data to a digital signal controller (DSC). Resolver signals are further processed in DSC to extract position information. Accuracy of the position measurement is limited by quality of the sensor line signals, which in ideal case are sine and cosine waves. In practice these signals are not ideal and show different amplitudes, dc drifts and quadrature error. All non-idealities occuring in resolver signals are described in [2]. In general accuracy of position measurement can be improved by calibration.

Calibration can be carried out using additional hardware. For example high precision rotary table can be used as position reference and the measured position error over one revolution can be implemented by software like compensation function for measurement accuracy improvement [3].

Another possibility is to exploit auto-calibration algorithm, which does not need additional hardware. Such algorithms process and correct resolver line signals to improve sensor's accuracy. One of the possible methods for resolver position error suppression is ellipse fitting approach [1]. Line signals plotted versus each other are tracking an ellipse. By finding the ellipse parameters we can obtain resolver error parameters. If such parameters are known they can be used for resolver line signals corrections with subsequent reduction of resolver's position error.

Resolver is rotary transformer with one rotor and two stator windings displaced 90 degrees from each other. Resolver output signals after demodulation can be expressed as follows:

$$\begin{aligned} V_{\sin} &= A_s \sin(\theta) + B_s \\ V_{\cos} &= A_c \cos(\theta + \alpha) + B_c \end{aligned} \tag{1}$$

where A_s and A_c are sine and cosine amplitudes, B_s and B_c are offsets, α represents amount of imperfect quadrature and θ is rotor position. These signals are sampled by AD converter in DSC and position information is then extracted. By proper corrections of line signals the observer position error can be substantially reduced. Following paragraphs describe procedure based on ellipse fitting technique enabling to gain line signals corrections.

2. Ellipse fitting

Data from resolver signals are tracking an ellipse that can be defined in Cartesian plane by implicit equation [5]:

$$x_1 V_{\cos}^2 + x_2 V_{\sin}^2 + x_3 V_{\sin} V_{\cos} + x_4 V_{\cos} + x_5 V_{\sin} = 1 \qquad (2)$$

If we define ellipse parameter vector as $\boldsymbol{x}=[x_1\ x_2\ x_3\ x_4\ x_5]^T$ and input data vector as $\boldsymbol{a}=[V_{cos}^2\ V_{sin}^2\ V_{cos}V_{sin}\ V_{cos}\ V_{sin}]$ that the right hand side will be $b=[1]$. Matrix form of (2) is as follows:

$$\begin{bmatrix} \mathbf{a_1} \\ \mathbf{a_2} \\ \vdots \\ \mathbf{a_k} \end{bmatrix} \mathbf{x}^T = \begin{bmatrix} b_1 \\ b_2 \\ \vdots \\ b_k \end{bmatrix} + \begin{bmatrix} e_1 \\ e_2 \\ \vdots \\ e_k \end{bmatrix} \Rightarrow \mathbf{Ax} = \mathbf{B} + \mathbf{E}, \qquad (3)$$

where $\boldsymbol{E}$ is matrix containing measurement errors. With every new measurement a new vector $\boldsymbol{a_k}$ into matrix $\boldsymbol{A}$ is obtained. To find corresponding ellipse represented by its coefficients $\boldsymbol{x}$ equation $\boldsymbol{x}=\boldsymbol{A}^{-1}\boldsymbol{B}$ needs to be solved. But the solution cannot be found in this form because the matrix $\boldsymbol{A}$ is singular and the measurement error caused by noise is always present as it is shown in figure 1. Regression analysis therefore must be used and solution can be calculated by least squares in the form $\boldsymbol{x}=(\boldsymbol{A}^T\boldsymbol{A})^{-1}\boldsymbol{A}^T\boldsymbol{B}$. Due to many measurements matrix $\boldsymbol{A}^T\boldsymbol{A}$ can be very big and to find its inverse is difficult task. This problem can be overcome by using recursive least squares (RLS) algorithm [4].

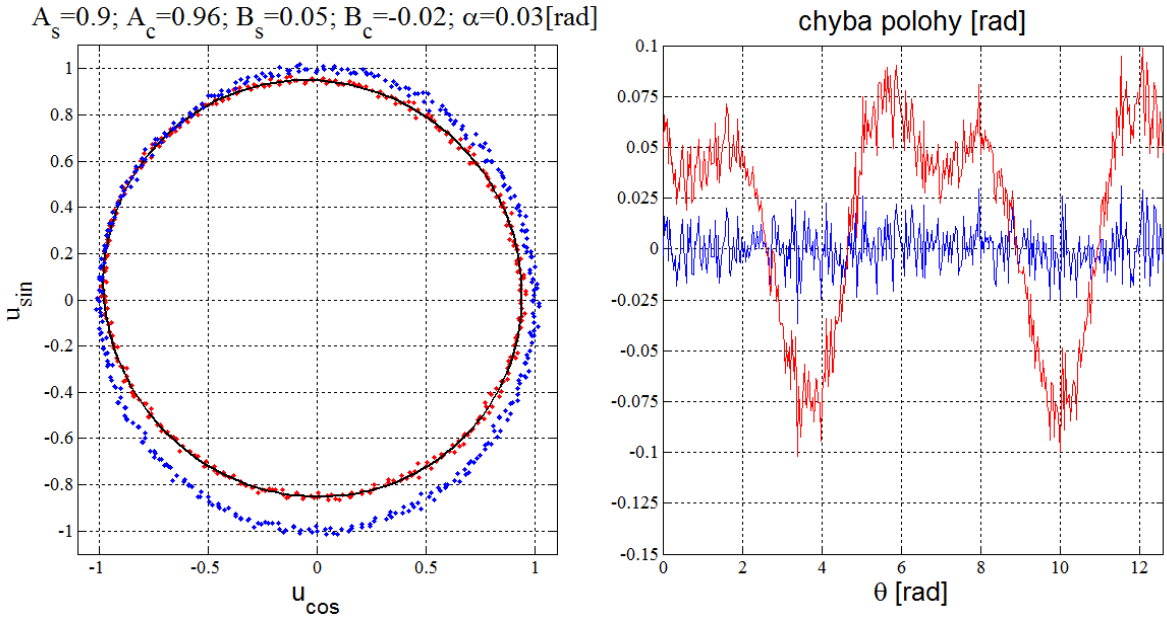

Fig. 1. a) Resolver line signals values plotted versus each other. b) Corresponding position error.

3. Recursive least squares estimation

In general RLS estimator minimizes following error function in each iteration k:

$$e(k) = \sum_{i=1}^{k} \left\{ \lambda^{k-1} (b(i) - \mathbf{a}(k)\mathbf{x}(i))^2 \right\} \qquad (4)$$

Parameter λ is optional forgetting factor from interval (0, 1›. We can collect all necessary equations to form RLS algorithm as follows:

$$\mathbf{E}_k = \mathbf{B_k} - \mathbf{A_k x_{k-1}}$$
$$\mathbf{P}_k = \lambda^{-1}\mathbf{P_{k-1}}\left(\mathbf{I} - \lambda^{-1}\mathbf{A_k^T}(1+\lambda^{-1}\mathbf{A_k P_{k-1} A_k}^{\mathbf{T}})^{-1}\mathbf{A_k P_{k-1}}\right) \quad (5)$$
$$\mathbf{x_k} = \mathbf{x_{k-1}} + \mathbf{P_k A_k}^{\mathbf{T}}\mathbf{E_k}$$

First the new error is calculated using old estimate $\boldsymbol{x_{k-1}}$ and new data $\boldsymbol{A_k}$. Than matrix $\boldsymbol{P_k}$ is updated. If in each iteration k the $\boldsymbol{A_k}$ is input matrix with only one row, than term $(1+\lambda^{-1}\boldsymbol{A_k P_{k-1} A_k}^{T})^{-1}$ in (5) will be one by one matrix and its inverse needn't be calculated. Finally vector $\boldsymbol{x_k}$ is updated. To converge to its true solution sufficient amount of data evenly distributed along ellipse over whole revolution need to be collected.

4. Correction of line signals

To gain line signals correction, the calculated ellipse parameters represented by vector $\boldsymbol{x}$ must be related to signals error parameters A_s, A_c, B_s, B_c and α. Merging two equations in (1) and eliminating θ results in following equation:

$$\left(\frac{V_{\cos}-B_c}{A_c\cos(\alpha)}\right)^2 + \left(\frac{V_{\sin}-B_s}{A_s\cos(\alpha)}\right)^2 + \frac{2\sin(\alpha)}{A_s A_c\cos^2(\alpha)}(V_{\sin}-B_s)(V_{\cos}-B_c) = 1 \quad (6)$$

Comparing equations (2) and (6) with their corresponding coefficients and after algebraic manipulations the following equations for line signals error parameters estimation can be derived using vector $\boldsymbol{x}$:

$$B_s = \frac{2x_1x_5 - x_3x_4}{x_3^2 - 4x_1x_2} \qquad A_c = \sqrt{\frac{4x_2(1+x_1B_c^2 + x_2B_s^2 + x_3B_sB_c)}{4x_1x_2 - x_3^2}}$$
$$B_c = \frac{2x_2x_4 - x_3x_5}{x_3^2 - 4x_1x_2} \qquad A_s = A_c\sqrt{\frac{x_1}{x_2}} \quad (7)$$
$$\alpha = \arcsin\left(\frac{x_3}{\sqrt{4x_1x_2}}\right)$$

By (7) it is possible to calculate resolver error parameters using characteristic ellipse parameters. Corrected line signals are than calculated as follows:

$$\hat{V}_{\sin} = \frac{V_{\sin}-B_s}{A_s}$$
$$\hat{V}_{\cos} = \frac{\frac{V_{\cos}-B_c}{A_c} + \sin(\alpha)\hat{V}_{\sin}}{\cos(\alpha)} \quad (8)$$

Extracted position information from these corrected line signals has higher accuracy.

5. Simulation results

Simulations were carried out to verify performance of the proposed algorithm. PC program simulates field oriented control of synchronous motor with permanent magnets (SMPM). In Fig. 2 speed oscillations due to resolver non-ideal line signals can be seen. Proposed algorithm during time interval $t \in (0, 1\rangle$ s collect the samples of sin and cos signals. This data forms the blue ellipse and are used as the input data for (5) to calculate characteristic ellipse parameters $\boldsymbol{x}$. From $\boldsymbol{x}$ are calculated estimated parameters A_s, A_c, B_s, B_c and α using (7). Finally, after time interval 1 s, correction of the resolver line signals is applied using (8). The effect of line signal correction to the

speed and position accuracy can be seen from Fig. 2. The red ellipse represents data from corrected line signals. Described method is suitable for offline calibration because during normal operation input data don't have to be evenly distributed along the ellipse, which is very important for finding corresponding ellipse parameters. Estimated resolver error parameters can be used for correction during normal drive operation. The input data have to be collected at constant speed and during at least one mechanical revolution. From the Fig. 2. we can see significant suppression of position error after correction is applied.

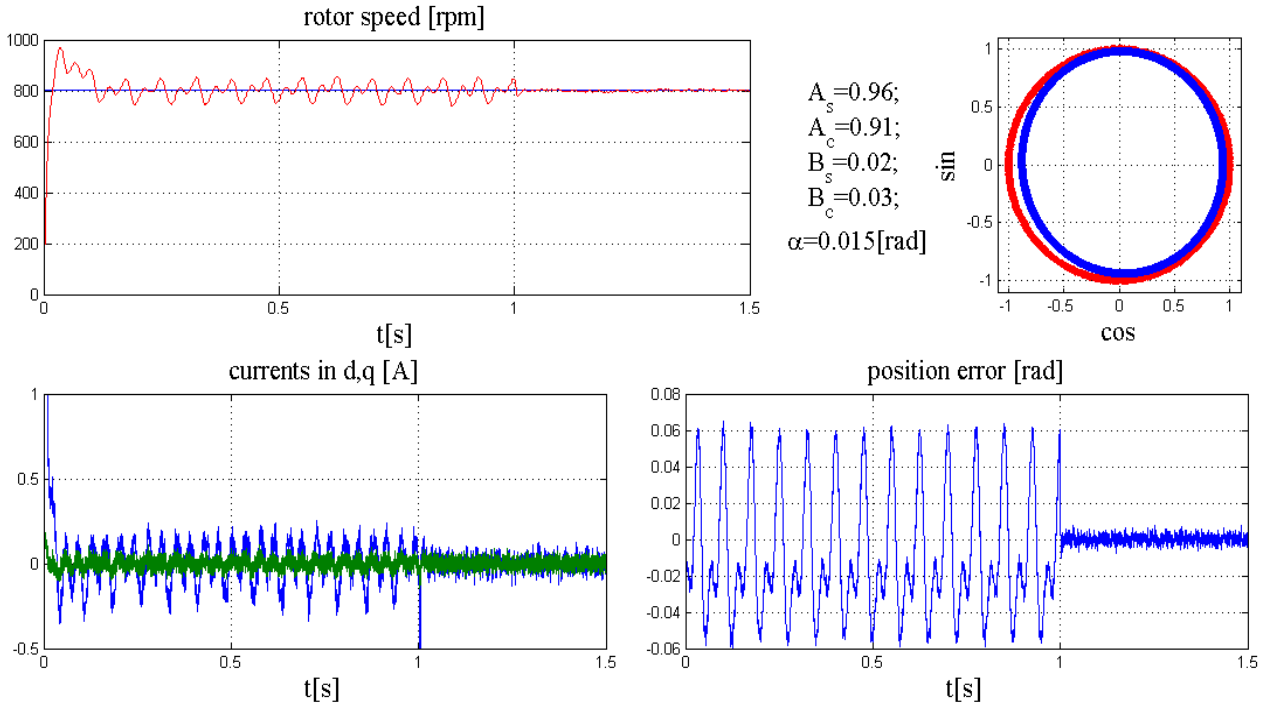

Fig. 2. Verification of the proposed algorithm by simulation.

6. Conclusion

Resolver represent absolute position sensor used in many industrial applications to control position and speed of actuator. Accuracy of the measurement is essential to achieve high performance of the drive.

When the resolver signals are plotted versus each other they form an ellipse. This paper investigates formulation between ellipse parameters and line signals error parameters. To find corresponding ellipse from measured data recursive least squares estimator is used. From ellipse parameters are calculated resolver error parameters that are further used for correction. This procedure is carried out before normal operation of the drive. Estimated error parameters are than used in normal operation to correct line signals.

Proposed calibration algorithm was verified by simulation. From the results can be clearly seen that the method can substantially reduce position error previously caused by resolver line signals imperfections.

Acknowledgement

The authors wish to thank for support the Slovak Grant agency VEGA.

References

[1] HOSEINNEZHAD, R., BAB-HADIASHAR, A., HARDING, P. *Calibration of resolver sensors in electromechanical braking systems: a modified recursive weighted least-squares approach*. IEEE Transactions on industrial electronics, Vol. 54, No. 2, April 2007.

[2] HANSELMAN, D. C. R*esolver signal requirement for high accuracy resolver-to digital conversion*. IEEE Transactions on industrial electronics, Vol. 37, No. 6, December 1990.

[3] KAUL, S. K., TICKOO, A. K., KOUL, R., KUMAR, N. *Improving the accuracy of low-cost resolver-based encoders using harmonic analysis.* www.sciencedirect.com, December 2007.

[4] LEWIS, J. M., LAKSHMIVARAHAN, S., DHALL, S. *Dynamic data assimilation a least squares approach.* Cambridge University Press 2006.

[5] FITZGIBBON, A., PILU, M., FISHER, R. B. *Direct least squares fitting of ellipses*. Pattern Analysis and Machine Intelligence, Vol. 21, No. 5, May 1999.

Transcom 2011, 27-29 June 2011
University of Žilina, Žilina, Slovak Republic

A design of CAN-bus for experimental stand of hybrid drive

*Tomas Haubert
*Czech Technical University in Prague, Faculty for Electrical Engineering, Department of electric drives and traction

Abstract. This manuscript discusses a particular design of CAN bus for the control of experimental stand of hybrid drives. In order to design the CAN bus, it is necessary know the dynamic; measurement and control signals. The experimental stand simulates the drive in hybrid vehicles. The main part of this hybrid drive is an electric power splitter (EPS), which divides the input of mechanical energy from internal combustion engine (ICE) into the first output mechanical energy for car wheel and the second electric energy supplies the DC bus. The experimental stand includes a supercapacitor for storage of electrical energy and a traction motor for the drive wheel car.

Keywords: hybrid vehicle, hybrid drive, electric power splitter, CAN

1. Introduction

The CAN (Controller Area Network) is a serial communication bus, which was developed by Bosch in the early 1980's to realize the data exchange between controller and measurement systems in modern automobiles. The communication medium can be a double stranded wire, coaxial cable or optical fiber with communication speed of up to 1 MbPS. Communication interface integrates physical level and data link layer and it care about correctness sending or receiving data. In case of error detection the communication interface generates the error frame. A signalization level is recessive or dominant. The data link layer cares about an approach to communication medium, provides a priority, data coding and error detection. An individual data frames are received simultaneously by all nodes which decide on the desirability of data the application layer.

The application layer is the topmost layer and therefore can be defined by standards such as the CANOpen standard for industrial automation. The using of the standard application layer is not necessary, because it is possible to program the actual application. Data area length is up to 8 bytes and a bus designer must design the number of data bytes and information value.

2. Experimental Stand of Hybrid Vehicles

As a part of Josef Bozek Research center, the experimental stand has been created in laboratory at Department of electric drives and traction. This stand can change the configuration of hybrid drives on serial hybrid drives, parallel hybrid drives, and a combined hybrid drive. The actual configuration is combined to the hybrid drive with electric power splitter. The schematic of this experimental stand is shown in fig. 1. The parts of this drive are two identical induction motors, which are controlled by Danfoss frequency converters. The first motor simulates a combustion engine (ICE) and works with speed control. The traction load (brake) is simulated by the second motor with produces braking torque M_{brake}.

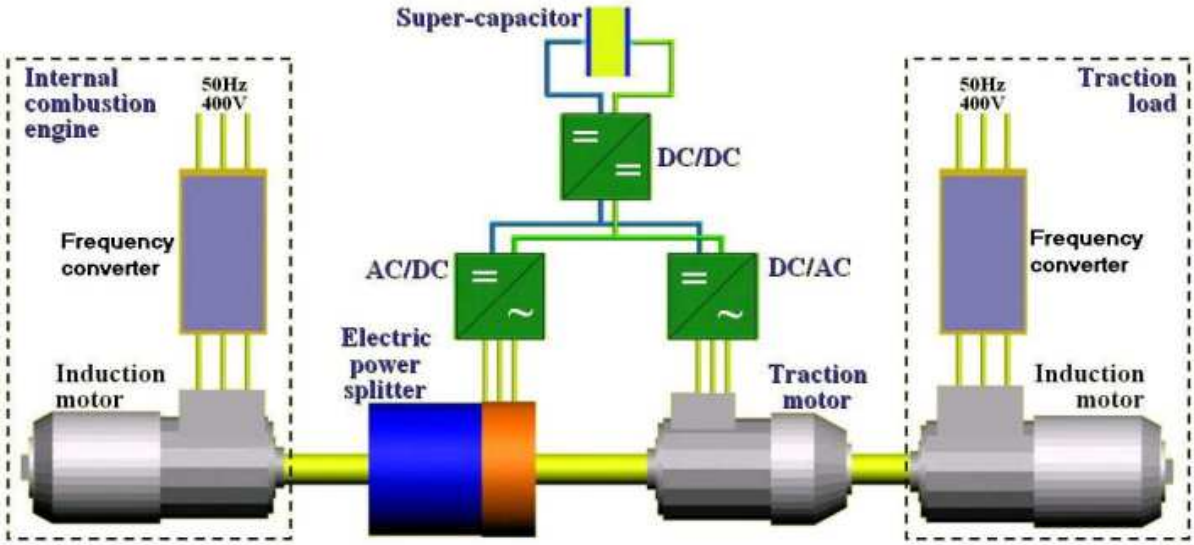

Fig. 1. Experimental working stand

The electric power splitter is a synchronous machine, which has two rotating parts. The input is the reference speed from ICE and the output are the stator turn and electrical energy, which is transferred by brush to the AC/DC converter. This converter is a source of electrical energy to the DC bus. The energy from this DC bus is transferred by DC/AC converter to the traction motor (TM). The shaft of TM is connected to the EPS stator and traction load. To the DC-bus is connected in parallel to the DC/DC converter for charging/discharging supercapacitor.

2.1. The control and measurement signals experimental stand

The two signals which are measured are current and voltage in DC bus, the electrical energy in the supercapacitor, torque between ICE and EPS and torque between TM and brake. The signals for control are the reference speed for frequency converter of ICE, reference torque for frequency converter of brake. The next control signals are the reference for AC/DC and DC/AC converters. The control unit of DC/DC converter the supercapacitor will have a special frame for settings and control of energy in supercapacitor.

3. A design of CAN-bus

In Tab. 1 is given the list of all controlled and measurement signals, which are necessary to ensure the stable operation of hybrid drive.

The name of signal	Label	Specification
ICE reference speed	n_{refICE} [RPM]	The reference speed is connected to the frequency input f_{TTL} in range 0 – 65 kHz of frequency converter. The speed range of ICE is from 0 to 3000 RPM.
ICE actual speed	$n_{realICE}$ [RPM]	The feedback from speed sensor with frequency input f_{TTL} in range 0 – 65 kHz corresponding to actual speed in range 0 – 3000 RPM.
Brake reference torque	M_{brake} [Nm]	The reference torque is connected to the frequency input in range 0 – 65 kHz of frequency converter, corresponding to actual torque in range -30 - +30 Nm
Brake actual speed	$n_{realbrake}$ [RPM]	See ICE actual speed.
Voltage from AC/DC converter	U_{ACDC} [V]	The reference is voltage in range 0 – 10 V, which corresponds to the output voltage AC/DC converter in range 0 – max value. Max value voltage depends on different stator and rotor speed of EPS.
TM reference speed	n_{TM} [RPM]	The reference value is voltage in range 0 – 10 V, which corresponds to the speed in range 0 – 6000 RPM.

Reference energy of supercapacitor	E_{SC} [kJ]	The value of reference energy supercapacitor depends on the main control system. Max value stored energy is 157 kJ.
Logic signals	-	The logic signals for CAN units, which turn on/off the main control system.
Torque between ICE and EPS	M_{ICE} [Nm]	Measurement torque between ICE and EPS is measured by HBM Spider8.
Torque between TM and brake	M_{brake} [Nm]	Measurement torque between TM and brake, which simulates the load from wheel car.
DC bus voltage	U_{DC} [V]	It is the output voltage from AC/DC converter EPS, the input voltage for DC/AC converter TM and in/out voltage for DC/DC converter of supercapacitor.
DC bus current	I_{DC} [V]	It is the current between output of AC/DC converter EPS and input of DC/AC converter.
Actual stored energy of supercapacitor	E_{SC} [kJ]	It is the actual energy stored in supercapacitor, which has a capacity equal to 100F. For voltage max value 56 V is the stored energy 157 kJ.

Tab.1. The measurement and control signals

3.1. The CAN units for measurement and control hybrid drive

The number of CAN units depends on the number of control units in an experimental stand and the geometrical structure these control units. The actual geometrical structure is shown on Fig. 2.

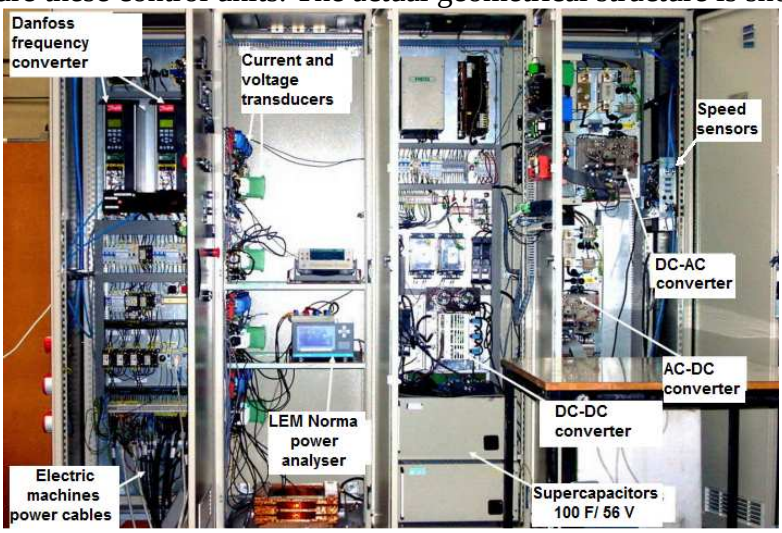

Fig. 2. The geometrical structure of experimental stand

The CAN units are developing for this experimental stand and are including a Freescale digital signal processor (DSP). These units are:

- CAN unit 1 – Speed sensors
- CAN unit 2 – Danfoss frequency converter
- CAN unit 3 – AC/DC and DC/AC converter
- CAN unit 4 – Control unit of supercapacitor
- CAN unit 5 – Measurement unit for torque sensors

3.2. A design of data frames

For CAN-bus design is necessary know a dynamics of controlled system. The smallest time response of data exchange in CAN-bus is ca 1 ms. For faster signals it is better to use another transfer medium. Experimental stand of hybrid drive has 4 drivers with a tenth of a second response time. The structure of data parts communicating frames, transmission period and priority are shown in Tab. 2. The highest priority is assigned to transfer information from speed sensor to frequency converter. This message is transmitted every 20 ms. The signals for control of hybrid drive have the variable transmission period. The data frames include the byte for configuration of control units.

Priority	Transmission period	The number of CAN unit	DATA 1	DATA 2	DATA 3	DATA 4	DATA 5	DATA 6
1	20 ms	1	$n_{realICE}$	$n_{realICE}$	$n_{realbrake}$	$n_{realbrake}$		
2	-	2	Config	Config	n_{refICE}	n_{refICE}	$M_{refbrake}$	$M_{refbrake}$
3	-	3	Config	Config	U_{ACDC}	n_{TM}		
4	-	4	Config	Config	E_{refSC}	E_{refSC}		
5	50 ms	3	U_{DC}	I_{DC}				
6	100 ms	4	Config	Config	E_{SC}	E_{SC}		
7	100 ms	5	M_{ICE}	M_{ICE}	M_{brake}	M_{brake}		

Tab.2. The structure of data frames

The main control system will be replaced for development purposes very simple manual control, where will be developed in LabVIEW in a master PC. For communication between the master PC and another control unit CAN-bus will be used CAN-USB converter. From the main program will be possible to transmit all signals.

4. Conclusion

The CAN bus provides a reliable communication between control units, which are used as basic buildings blocks of the structure of experimental stand of the hybrid drive. Use this bus is appropriate to the amount of data transmitted, requirements for transmission speed and reliability.

The choice of communication method was the first task by implementation of control modern methods on experimental stand of hybrid drive. The second task will be optimizing data frames and verifying the functionality of the proposed solution.

References

[1] CUNDEV, D. *Ph.D. Thesis.* Czech Technical University in Prague, 2009.

[2] RAN, L., JUNFENG, W., HAIYING, W. *Design Method of CAN BUS Network Communication Structure for Electric Vehicle.* IFOST – International Forum on Strategic Technology, Ulsuan, Korea (South), October 2010

[3] RENJUN L., CHU L., FENG L. *A design for automotive CAN bus monitoring system.* Vehicle Power and Propulsion Conference, 2008. Harbin, China, September 2008

[4] CUNDEV, D., CEROVSKY, Z., MINDL, P. *Modeling of the hybrid electric drive with an electric power splitter and simulation of the fuel efficiency.* EPE '09, Barcelona, Spain, September 2009

Transcom 2011, 27-29 June 2011
University of Žilina, Žilina, Slovak Republic

Reliability simulation of QDEC machine in programmable FPGA circuit

*Ondrej Hock, *Peter Sindler, Jozef *Cuntala
University of Žilina, Faculty of Electrical Engineering, Department of Mechatronic and Electronic,
Univerzitna 1, 01026 Žilina, Slovakia, {hock, sindler, cuntala}@fel.uniza.sk

Abstract. The article deals with the design and simulation QDEC (Quadrature Decoder) machine for implementation in a programmable FPGA (Field Programmable Gate Array) circuit. The purpose research activities of reliable QDEC machine in the FPGA is the incorporation of this model to control of the robot. In the first part of the article describes the possibility of machine. In the second part are describe the state machine diagram and the algebraic description of the behavior. In the third section of article are provides the selected results from the simulation of error-free and fault states machine.

Keywords: Reliability, FPGA, QDEC machine.

1. Introduction

In the electronic circuits can been changed of transmitted information influence induced impulse or unwanted noise in transmision. In circuit arise permanent or transient errors. These errors are significantly lowers the operational reliability of the circuit. Mostly it is the transient errors, which are called *Single Event Upsets* (SEUS) [1] or the *Single Event Effects* (SEES) [2]. In such cases there is a change of state in flip circuit, overwriting the memory cell or register. Such errors are called transient because there is no permanent violation in circuit. The significant part of these faults is caused by cosmic rays or alpha particles penetrating of casing components, or power pulses that spread supply lines. For circuits manufactured production technology less than 65 nm are SEUs much more than in the previous technologies [1] [2].

Transient errors can have influence on correct behavior of program, change of machine state or change of memory data. Therefore the system must check the accuracy of the data so as to avoid that incorrect information will be considered correct. In many cases, this could have catastrophic consequences. Therefore the system must be resistant to transient errors. Effect of transient errors on the circuit is shown in figure 1.

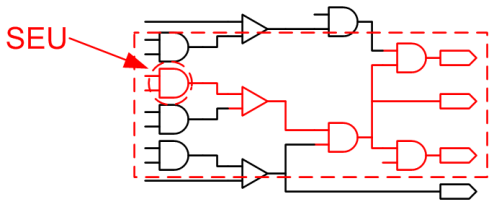

Fig. 1. Effect of transient errors on circuit which is implemented in FPGA.

QDEC machine is working as a decoder of two input signals of incremental encoder. Implementing of QDEC machine with increased reliability, we are try to eliminate transient errors in the machine.

2. Behavior of a simple QDEC machine

QDEC machine is working as a decoder of two input signals of incremental encoder. Signals are shifted between each of +/- 90°. Figure 2 displays the output channels *CHA* and *CHB*, which shows the change in the direction of rotation of the incremental encoder.

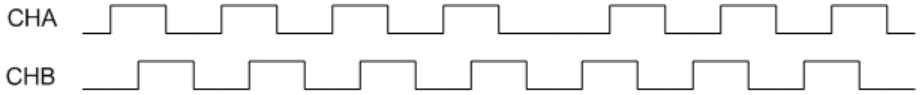

Fig. 2. Output signals from incremental encoder.

We can generate from simple QDEC machine signal *PULSE* which determines number of increments and signal *DIRECTION* which determines direction of rotation. Figure 3 shows input and output signals from simple QDEC machine.

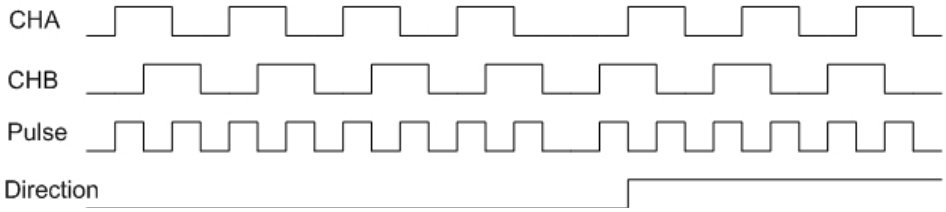

Fig. 3. Input and output signals from simple QDEC machine.

3. States diagram of simple QDEC machine

We can see in Figure 4 states diagram of error-free machine. From the state diagram is obvious that they are not treated all possible combinations. When a failure occurs the machine is getting to state which is not described. This reduces reliability of QDEC machine.

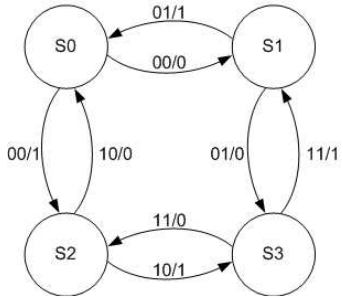

Fig. 4. States diagram of simple QDEC machine [3].

We are creating from Figure 4 states table and output table (tab.1). States *S0* to *S3* are composed of state variables z_1 and z_2. Input vectors *X1* to *X4* contain input variables *CHA* and *CHB*.

		00	01	10	11	00	01	10	11
		X1	X2	X3	X4	X1	X2	X3	X4
00	S0	-	S1	S2	-	-	1	0	-
01	S1	S0	-	-	S3	0	-	-	1
10	S2	S0	-	-	S3	1	-	-	0
11	S3	-	S1	S2	-	-	0	1	-

- undefined states

Tab. 1 States table and output table of QDEC machine

4. Algebraic description of QDEC machine

We are composed equation of output variable *Direction* (1), (2) from output table. States variable Z_1 and Z_2 represent value of state in the next step.

$$dir = Z_1.\overline{Z_2}.\overline{CHA}.\overline{CHB} + Z_1.Z_2.CHA.\overline{CHB} + \overline{Z_1}.Z_2.CHA.CHB + \overline{Z_1}.\overline{Z_2}.\overline{CHA}.CHB \quad (1)$$

we get after the adjustment:

$$dir = \left(Z_1 \ XOR \ CHB\right).\left(Z_2 \ XNOR \ CHA\right) \quad (2)$$

We are composed equations of states variable from state table (3), (4).

$$Z_1 = \overline{z_1}.\overline{z_2}.CHA.\overline{CHB} + z_1.\overline{z_2}.CHA.CHB + z_1.z_2.CHA.\overline{CHB} + \overline{z_1}.z_2.CHA.CHB \quad (3)$$

$$Z_2 = \overline{z_1}.\overline{z_2}.\overline{CHA}.CHB + z_1.\overline{z_2}.CHA.CHB + z_1.z_2.\overline{CHA}.CHB + \overline{z_1}.z_2.CHA.CHB \quad (4)$$

we get after the adjustment:

$$Z_1 = CHA.\left[\overline{z_2}.\left(z_1 \ XNOR \ CHB\right) + z_2.\left(z_1 \ XOR \ CHB\right)\right] \quad (5)$$

$$Z_2 = CHB.\left[\overline{z_2}.\left(z_1 \ XNOR \ CHA\right) + z_2.\left(z_1 \ XOR \ CHA\right)\right] \quad (6)$$

5. Fault state simulation of QDEC machine

It can be created simulation model of QDEC machine from equation (2), (5) a (6) in Matlab Simulink enviroment using the System Generator for DSP toolbox. This toolbox is design for simulation of programs for FPGA circuits. Figure 5 shows block scheme of QDEC machine. IRC block simulating behavior of incremental encoder. STATE block represent state of machine and he is designed from equations (5) and (6). LOGIC block contains involvement of logic blocks from equation (2).

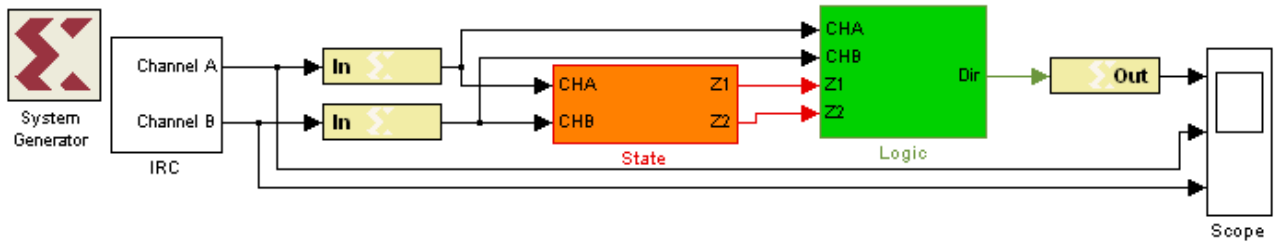

Fig. 5. Block scheme of machine in Matlab Simulink.

Figures 6, 7 and 8 shows simulation result for error-free operating, permanent fault and transient error of QDEC machine. On the upper course is displayed output variable *Direction* and on the lower course is displayed input channels *CHA* and *CHB* from incremental encoder. Figure 6 shows error-free operating of QDEC machine. At the time 10 µs and 20 µs was simulated direction change of rotation of the incremental encoder.

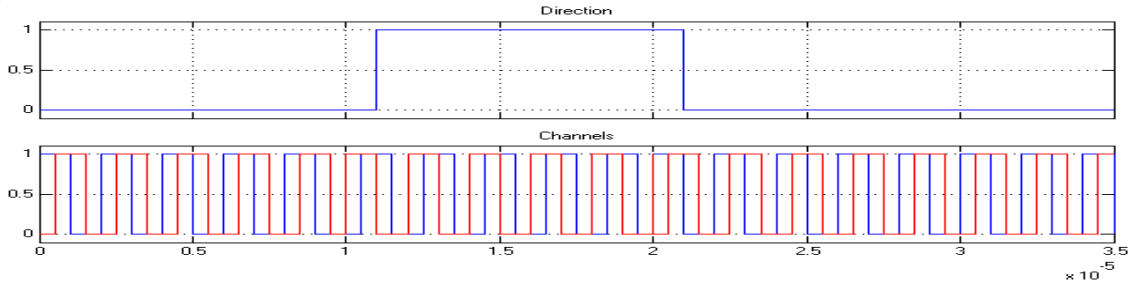

Fig. 6. Error-free operating simulation of QDEC machine.

In figure 7 we can see expressions of a permanent fault on the machine described in equation 7.

$$Z_2 = CHB.\left[z_2.\left(z_1 \ XNOR \ CHA\right) + z_2.\left(z_1 \ XOR \ CHA\right)\right] \quad (7)$$

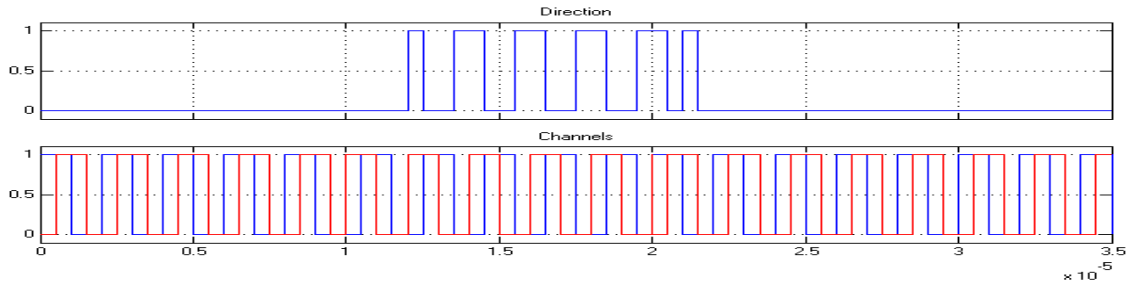

Fig. 7. Permanent fault simulation on QDEC machine.

Figure 8 shows the impact of transient error with duration 1 μs on the machine with we are simulated in a time of 15 μs. We created SEU on the AND logic element who is indicated in equation 8.

$$Z_2 = CHB\left[z_2.(z_1 \ XNOR \ CHA) + z_2.(z_1 \ XOR \ CHA)\right] \qquad (8)$$

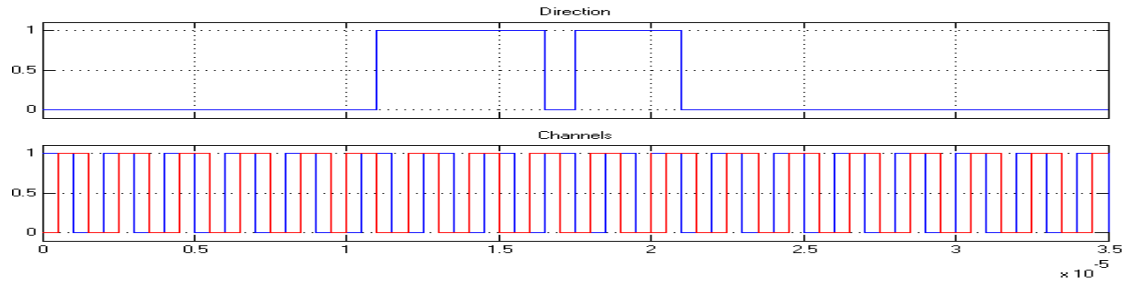

Fig. 8. Transient error simulation of QDEC machine.

6. Conclusion

As we can see on simulation results simple QDEC machine represented for error-free operating almost ideal solution for scanning motor RPM. Due to its simplicity, however, does not need to treat fault states that may have catastrophic consequences in some application. We proved in simulation that this type of QDEC machine has a lower reliability. In a further continuation of solutions we want to increase reliability by eliminating fault states of QDEC machine using methods of code redundancy respectively structural backing. Today we can use both methods whoes can be implemented in FPGA.

Acknowledgement

The authors wish to thank for the support to the R&D operational program Centre of excellence of power electronics systems and materials for their components. The project is funded by European Community, ERDF – European regional development fund.

References

[1] SYED Z. SHAZLI AND MEHDI B. TAHOORI *Transient Error Detection and Recovery in Processor Pipelines* 24th IEEE International Symposium on Defect and Fault Tolerance in VLSI Systems, 2009.

[2] ACTEL *Single-Event Effects in FPGAs* Actel Corporation, 2007.

[3] ACTEL VHDL and programmable logic for custom preipherals Actel Corporation, 2008

[4] ČUNTALA J., ŠINDLER P., KONDELOVÁ A.: *Progress in programmable logic*, Advances in Electrical and Electronic Engineering, ISSN 1336-1376, No. 2, Vol. 3 (2004), p. 219-222

[5] ČUNTALA J., ŠINDLER P., KONDELOVÁ A.: *The new implementation possibilities for electronic logical devices*, Advances in electrical and electronic engineering - Vol. 2, No. 1 (2003) , p. 61-64

Transcom 2011, 27-29 June 2011
University of Žilina, Žilina, Slovak Republic

Energy optimal control of induction motor

*Michal Hrkeľ
*University of Žilina, Department of Power Electrical Systems, Faculty of Electrical Engineering,
Univerzitna 1, 01026 Žilina, Slovakia, michal.hrkel@kves.uniza.sk

Abstract. The paper deals with minimization of induction motor losses during direct vector control. The losses in copper and iron can be minimized via control of rotor magnetic flux. An algorithm for optimal flux control is developed and verified by simulation.

Keywords: Induction motor, Vector control, Induction motor losses minimization,

1. Introduction

The most frequently used motors in industry are induction motors (IM) [1]. If the efficiency of such drives is improved then substantial energy saving can contribute to the improvement of environment.

There are two ways of motor efficiency improvement. For newly constructed IM new design techniques are developed [1]. However, for existing drives with variable speed and load, the algorithms for calculation of the optimal motor flux are widely used.

This paper presents method for control of the magnetic flux such a way that losses of induction motor are minimized. If compared with classical vector control, where the value of magnetic flux is constant, this method varies the value of magnetic flux as a function of speed and load.

2. Model of optimal vector control induction motor

2.1. Equivalent circuit and mathematic model

An equivalent circuit of IM for calculation of losses in the motor windings, iron and mechanical losses is shown in Fig. 1 for one phase of IM in synchronously rotating frame. The resistances of R_s, R_r and R_{fe} represent stator losses, rotor losses and iron losses respectively. The L_{ls}, L_{lr} and L_m are correspondingly the stator and rotor leakage inductance and magnetizing inductance. The ω_1 and ω_r are respectively the stator current frequency and rotor electrical speed. The i_{ds}, i_{dr} and i_{dm} and the i_{qs}, i_{qr} and i_{qm} are the current of stator winding, rotor winding and corresponding currents to air gap flux for direct and quadrature axis respectively-axis [2].

To the electrical losses are added the friction loss done by (1)..

$$P_{f\omega} = C_{f\omega} . \omega_r^2 \tag{1}$$

where $C_{f\omega}$ is of mechanical losses coefficient [4]

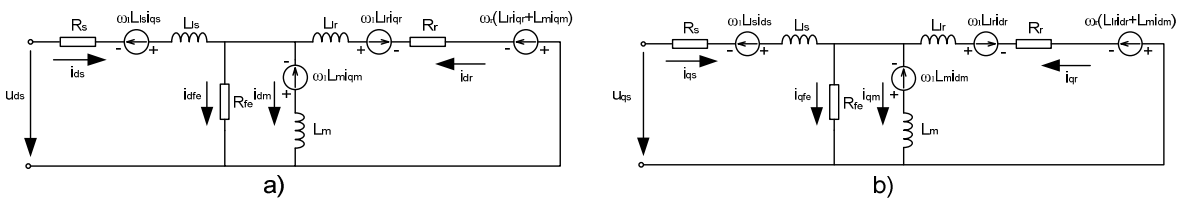

Fig.1. Equivalent circuit of IM for direct a) and quadrature axis b)

Dynamics of rotor-flux oriented vector control of IM in d_q frame is described by following equations, where (6) includes the iron losses [2]:

$$\frac{di_{ds}}{dt} = \frac{1}{L_s}\left[u_{ds} - R_s i_{ds} - L_m \frac{di_{dm}}{dt} + \omega_1 L_m i_{qm}\right] \quad (2)$$

$$\frac{di_{ds}}{dt} = \frac{1}{L_s}\left[u_{ds} - R_s i_{ds} - L_m \frac{di_{dm}}{dt} + \omega_1 L_m i_{qm}\right] \quad (3)$$

$$\frac{di_{qs}}{dt} = \frac{1}{L_s}\left[u_{qs} - R_s i_{qs} - L_m \frac{di_{qm}}{dt} - \omega_1 L_m i_{dm}\right] \quad (4)$$

$$\frac{di_{dr}}{dt} = \frac{1}{L_r}\left[-R_r i_{dr} - L_m \frac{di_{dm}}{dt}\right] \qquad i_{qr} = -\frac{1}{R_r}\omega_s[L_r i_{dr} + L_m i_{dm}] \quad (5)$$

$$i_{dm} = i_{ds} + i_{dr} + \frac{\omega_1 L_m i_{qm}}{R_{fe}} \qquad i_{qm} = i_{qs} + i_{qr} - \frac{\omega_1 L_m i_{dm}}{R_{fe}} \quad (6)$$

$$T_e = \frac{3}{2} p \frac{L_m}{L_r} i_{qm} \psi_{qm} \quad (7)$$

2.2. Optimal efficiency control

The total losses of IM are given as:

$$P_{loss} = P_{cus} + P_{cur} + P_{fe} + P_{f\omega} = (a_1 + a_2\omega_r^2)\psi_r^2 + a_3\frac{T_e^2}{\psi_r^2} + C_{f\omega}.\omega_r^2$$

$$\text{where } a_1 = \frac{R_s}{n_p^2 L_m^2}, a_2 = \frac{1}{(R_r + R_{fe})}, a_3 = \frac{L_r^2}{n_p^2 L_m^2}\left(R_s + \frac{R_r R_{fe}}{R_r + R_{fe}}\right) \quad (8)$$

Efficiency is defined as the output shaft power to total input power of induction motor [3].

$$\eta = \frac{\omega_r T_e}{P_{loss} + \omega_r T_e} \quad (9)$$

Following formula as a function of IM speed and load torque [3] can be derived for rotor magnetic flux, ψ_r, to achieve the maximum efficiency:

$$\psi_r^* = \left(\frac{a_3}{a_1 + a_2\omega_r^2}\right)^{\frac{1}{4}} (T_e)^{\frac{1}{2}} \quad (10)$$

From Fig. 2 can be clearly seen that to achieve maximum efficiency of the motor the rotor magnetic flux, ψ_r^*, should be adjusted as a function of rotor speed ω_r and load torque, T_e.

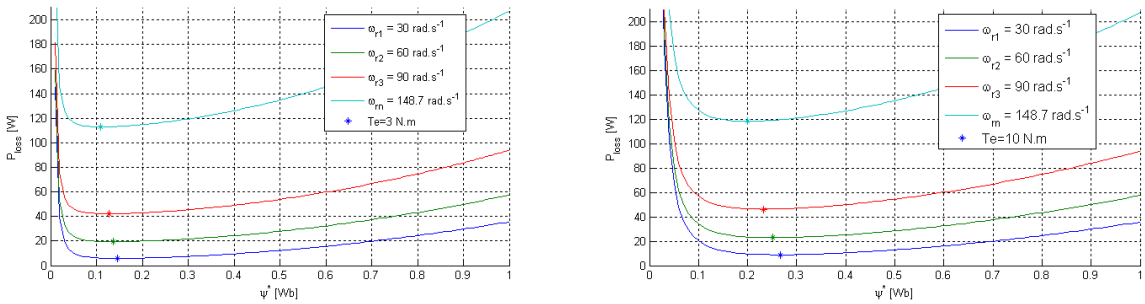

Fig.2. The losses of IM as a function of rotor flux at different speeds and different load torque as parameter.

3. Simulation results

The algorithms of IM losses minimization was verified by simulation model of vector controlled IM shown in Fig.3.

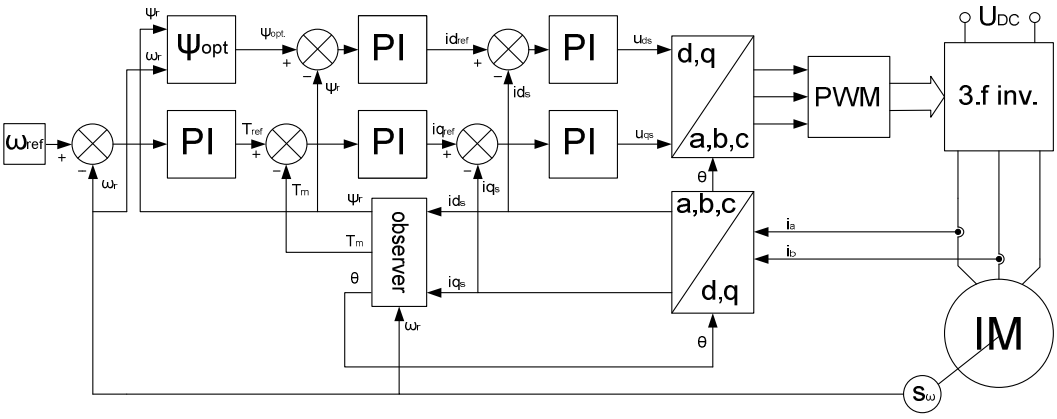

Fig.3. Block diagram of energy saving vector control of induction motor.

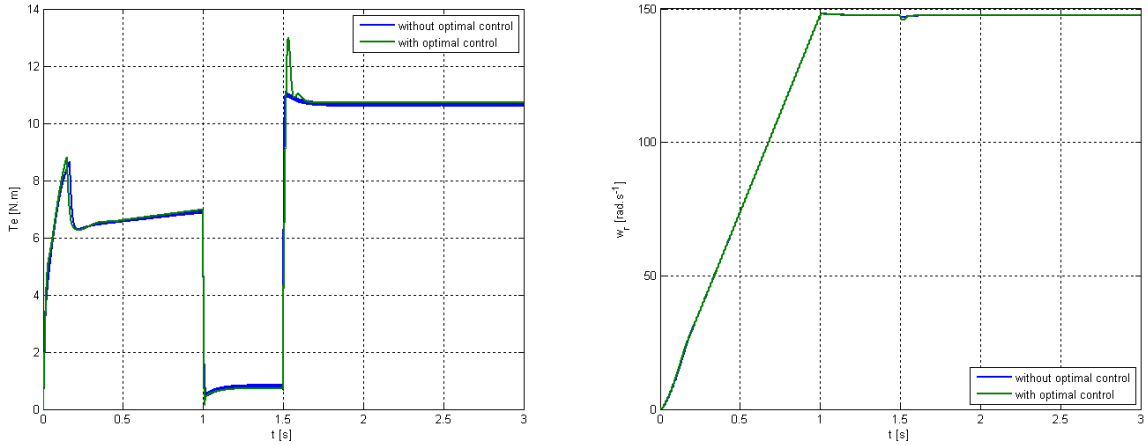

Fig. 4. Functions of angular speed, ω_r and electrical torque, T_e of vector controlled induction motor.

To verify overall energy savings the algorithm for IM vector control with a constant magnetic flux and IM vector control with the optimal magnetic flux were compared. Parameters of IM are as follows : R_s=2,876 Ω; R_r=2,654 Ω; L_m=319 mH; L_{ls}=10,75 mH; L_{lr}=10,75 mH; R_{fe}=321 Ω; ψ_n=0,897 Wb; n_n=1420 rpm; U_n=380 V; P_n=2,2 kW; f_n=50 Hz; T_n=14,8 Nm; J= 0,0423 kgm^2; $C_{f\omega}$=0,005. Induction motor speed up into rated speed in a 1 s and at t=1,5 s load torque, T_{load} =10 Nm is applied as can be seen in Fig. 4 .

From Fig. 5 the functions of efficiency and losses of IM can be seen. Overall efficiency of the motor was increased by 4% if algorithm taking into account optimal rotor flux was applied.

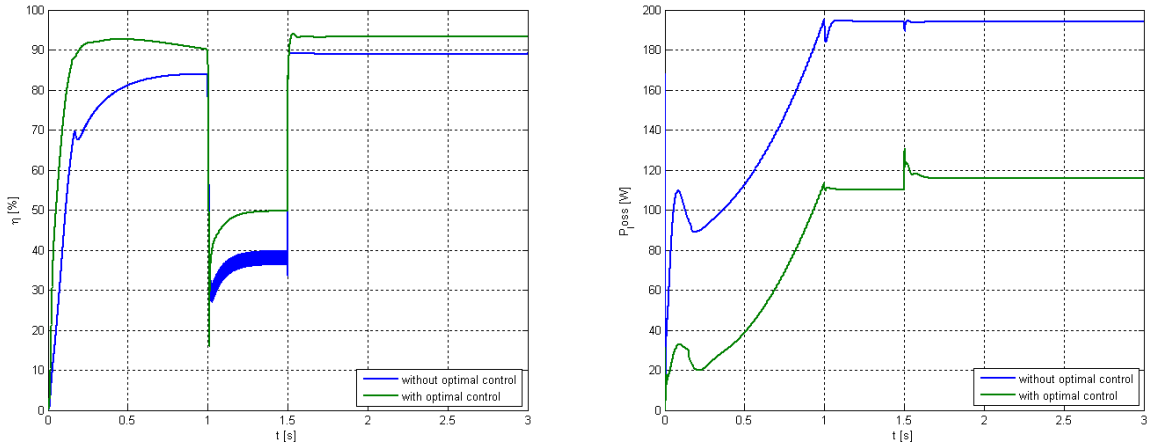

Fig.5. Computed functions of efficiency (left) and a motor losses (right).

4. Conclusion

The paper described a method for induction motor losses minimization taking into account machine speed and load torque. The method was implemented for vector control of IM and compared with constant flux control. Simulations of a new optimal flux control conform possibility to increase efficiency of IM by 4% which can bring for long tern service substantial energy savings.

Acknowledgement

The authors wish to thank for support the Slovak Grant agency VEGA 1/0355/11.

References

[1] Hussein E, Mutschler P, *Optimal lux loss model based of speed sensorless vector control induction motor*, Power Electronics, Machines and Drives, 5th IET International Conference, 2010

[2] Wong A, Ling Z, *Realization of vector control for induction motor considering iron loss*, Intelligent Information Technology Application, 2008

[3] Cui Naxin, Zhang Chenghui, Zhao Min, *Optimal efficiency control of field-oriented induction motor drive and rotor resistance adaptive identifying*, Proceedings, IPEMC, pp. 414-419, 2004.

[4] Hamid R, Amin A, Ahmed R, El-Gammal A, *New Technique for Maximum Efficiency of Induction Motors Based on Particle Swarm Optmization (PSO)*, 2006

Transcom 2011, 27-29 June 2011
University of Žilina, Žilina, Slovak Republic

Metamaterial Sensors for Biological Tissue Permittivity Measurement Based on Split Ring Resonators

[*]Katarina Istenikova
[*]University of Žilina, Faculty of Electrical Engineering, Department of Measurement and Applied Electrical Engineering, Univerzitná 1, 01026 Žilina, Slovakia, istenikova@fel.uniza.sk

Abstract. This article deals with design of microwave sensors for biological tissue dielectric properties measurement using metamaterial structure. A sensor design concept has been projected using split ring resonators (SRR). This paper presents two different constructions of sensor. First sensor is designed by using four identical split ring resonators. The second structure contains four different split ring resonators which are constructed to have different resonant frequencies and are decoupled from each other. In the paper are introduced numerical simulations of scattering parameters for above mentioned sensors without and with biological sample placed on the top of split ring resonators. The frequency shift of one individual resonant peak indicates the dielectric properties of the investigated biological sample.

Keywords: Biological tissues, dielectric properties, metamaterials, sensor, split ring resonators.

1. Introduction

Metamaterials are artificial structures that can be designed to exhibit specific electromagnetic properties not commonly found in nature. Metamaterials with simultaneously negative permittivity ε and permeability μ have received substantial attention in the scientific and engineering communities, because their unique properties have allowed novel applications, concepts and devices to be developed. Various metallic structures are used as metamaterials to achieve certain unusual characteristics which are suitable for dielectric properties measurement sensor design suitable for high frequency applications, such as microwaves. Generally the fundamental electromagnetic properties of metamaterials and the physical realization of these materials could be reviewed based on a general transmission line approach [1-2].

In this paper we describe the approach with implementation of metamaterial structure over design of sensor for permittivity of biological sample measurement in order to achieve the effective noninvasive method in microwave frequency region for dielectric properties of biological tissues detection. Organic tissue contains many inhomogeneities, especially when the abnormality like tumor is presented. Progression of metamaterial sensors can provide useful array for cancerous diseases detection.

The paper is organized as follows. The paper presents the theory behind the principle of operation of the metamaterial sensors. Next simulated results for two different metamaterial sensors without and with placed biological sample are presented. In the end of the paper there are given some conclusions.

2. Theoretical consideration

The network topology of the sensor can be derived from the theory of planar metamaterial transmission lines. The currently available artificial structures are realized by using planar structures with specific topology in *x-y* plane. Metamaterial structure used for the sensor consists of arrays of unit cells of split resonators which were designed by Pendry et al. [3]. The resonators consist of a periodically LC-loaded transmission line.

a) b)

Fig. 1. Unit cell configuration for a) left-handed, b) right-handed transmission line.

The line characteristic frequency is subsequently defined

$$\omega_0 = \frac{1}{\sqrt{LC}}. \tag{1}$$

There is a stopband for the LH-line below $\omega_0/2$ and above $2\omega_0$ for the RH-line. The resonance condition for both line types is

$$\beta l = n\pi, \tag{2}$$

where l is the physical length of resonator and β represents the wave number. For the LH-line resonator n values are attributed to negative numbers, for the RH-line resonator to positive numbers [4].

For measurement accuracy the resonance quality factors Q are of particular importance. Assuming that the inductor and capacitor have quality factors of Q_L and Q_C respectively, Q_0 factor for all harmonics and both line types is

$$Q_0 = \frac{Q_L Q_C}{Q_L + Q_C}. \tag{3}$$

2.1. Split ring resonators

Split ring resonators (SRR) are structures having strong response on electromagnetic field. The overall SRR can be represented by the equivalent circuit of a resonator. The band gap in the SRR transmission spectrum is produced by either magnetic or electrical resonances caused by the charge distribution of the incident field. The magnetic resonance is obtained mainly because of its capacitive components. When the sample is placed on the top of sensitive area, it causes the chance of the capacity and subsequently the resonant frequency of the subsistent ring is shifted. By changing the dimensions of gap, inner or outer ring or by introducing additional splits, the magnetic resonance can be influenced.

If it is possible to control the resonance of each element of the SRR array, the investigation of sample can be carried out. SRR are projected such that the outer splits are opposite to the line. If a sample, e.g. biological tissue, interacts with the outer split of a SRR, it changes the capacity due to a change of the effective permittivity [3-5].

3. Numerical simulations

The physical implementation of the transmission line sensor was carried out with the help of the software package CST Microwave Studio which is suitable for modeling of planar structures.

As shown in Fig. 2 two different prototypes were simulated. In microwave frequency region there is more types of metamaterials which could be used as a substrate of the sensor. According to requested frequency region and very small dimensions of sensors and resonators they were built on Rogers RT/Duroid 6010 with permittivity ε_r = 10.2 and a thickness h = 1.57 mm which proved the better simulation results as the other one (Rogers RT/Duroid 5880).

On the bottom side of the structure there is placed ground plane with thickness 9 μm. The major design objective was the line impedance of 50 Ω. To achieve the line impedance 50 Ω the length of the structure and transmission line 56 mm was selected. The width of transmission line is 2 mm. This values were calculated in software tool TX-line.

Both prototypes consist of 4 SRR with constant height 10 mm. The structure is a microstrip design and the sensitive area corresponds to the gap of the outer rings in each unit cell [4]. Distance between SRR was selected 1 mm and was numerically verified not to cause the change of resonant frequency by its neighboring rings.

The first structure contains 4 rings with identical width 10 mm. The second one contains 4 rings of different widths from 8 to 14 mm.

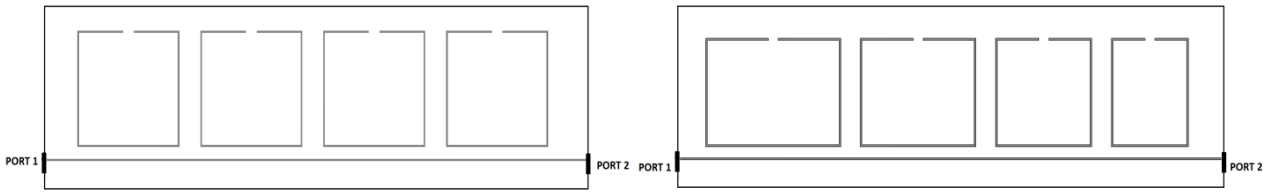

b) b)

Fig. 2. Structure of sensor based on split ring resonators. a) identical width of rings, b) different width of rings.

The results from the static simulations for TEM mode are shown in Fig. 3. The structure is inserted in an air box along, there are maintained electric boundaries only in *z* negative direction. As shown in Fig. 3 the small dielectric brick of bone with permittivity ε_r = 12 and dimensions 1.5x1.5x0.5 mm was placed on the top of the ring gap (in this case the second ring).

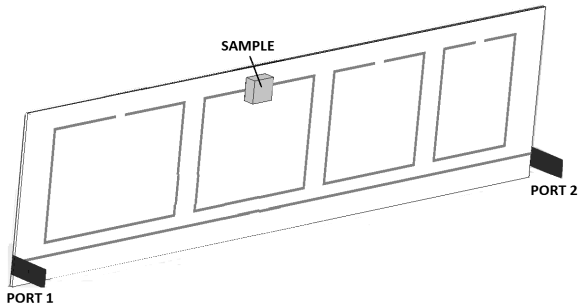

Fig. 3. Position of the investigated sample on the top of split ring resonator.

The sample placing on the top of ring causes the change of capacitance and subsequently the shift of the resonant frequency in comparison with empty ring gap. The relative permittivity determination is based on the extraction of scattering parameters (S-parameters). When the pulse reaches the biological sample it sends a reflection signal at a specific time. At the beginning of the measurement the system calibration using samples with well-known dielectric properties is necessary to specify permittivity dependence connected with resonant frequency. Subsequently the unknown sample is investigated and from the comparison of delay and amplitude of this pulse the relative permittivity of the sample can be detected.

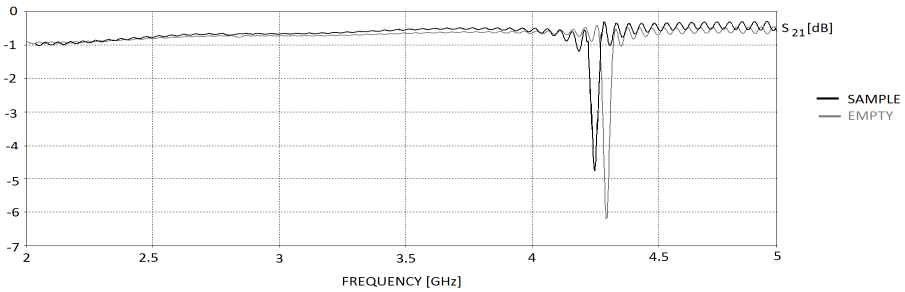

Fig. 4. Shift of the resonant frequency after placing the biological sample for sensor with identical width of rings.

On the Fig. 4 can be seen the shift of the resonant frequency and change of peak amplitude after placing the bone brick on the top of ring gap for sensor with identical width of rings. If the width of split ring resonators is identical, it has the same resonant frequency and can be seen only one peak.

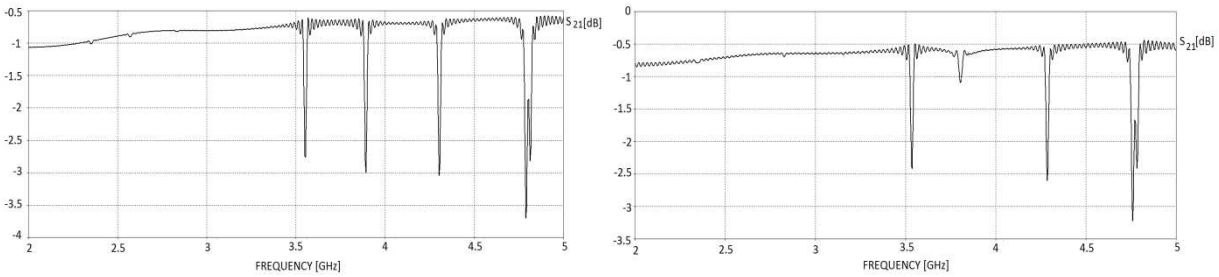

a) b)

Fig. 5. Resonant frequencies for a) empty, b) with bone sample perturbed sensor with different width of rings.

Fig. 5a) displays the S_{21} parameter for empty sensor containing 4 SRR with width of rings from 8 to 14 mm. Different width of resonators entail different resonant frequencies. For this reason on the graph there are depicted four peaks separated by a constant distance. On the Fig. 5b) there is shown the S_{21} parameter for the same sensor after placing the bone brick on the top of second ring gap. There is discernible peak shift and amplitude change for second peak in the order given which correspond to resonant frequency of second SRR where the sample is placed. From the resonant peak it is clear that the bone has higher losses. The resonant frequency can be detected and Q factor and permittivity can be calculated.

4. Conclusion

In this paper the numerical simulations of two metamaterial sensor structures for biological tissues dielectric properties detection were presented. The sensor structures were created using split ring resonators which could be due to their small dimensions important for developing very small microwave devices mainly for medical applications. In the future by using metamaterial split ring resonator sensors the presence of inhomogeneity in the tissue can be noticed which could be used in cancerous diseases diagnosis. To show the principle of biological tissue dielectric properties detection using metamaterial sensor was used bone sample. From the frequency shift the dielectric properties of sample can be detected. In future work the experimental measurement would be performed and measurement results with numerical simulations results compared.

Acknowledgement

The work has been done in the of Grant VEGA 1/0761/08 „Design of Microwave Methods for Materials Nondestructive Testing“ of the Ministry of Education of the Slovak Republic and project APVV-0535-07.

The author would like to thank Institut für Mikrowellentechnik und Photonik of Technische Universität Darmstadt, Germany.

References

[1] LAI, A., ITOH, T., CALOZ, CH. *Composite right/left-handed transmission line metamaterials*. IEEE Microwave Magazine, Vol. 5(3), p. 34-50, 2004.

[2] FAKTOROVÁ, D., OMELKA, P., ISTENÍKOVÁ, K. *Antenna parameter enhancement by using artificial magnetic structure*. Journal of Electrical Engineering, Vol. 61(7s), p. 156-159, 2010.

[3] PENDRY, J.B. *Magnetism from conductors and enhanced nonlinear phenomena*. IEEE Trans. Microwave Theor. Tech., Vol. 47(6), p. 2075-2084, 1999.

[4] PUENTES, M., STELLING, B., SCHÜSSLER, M., PENIRSCHKE, A., JACOBY, R. *Planar sensor for permittivity and velocity detection based on metamaterial transmission line resonator*. Microwave Conference 2009, EuMC 2009, p. 57-60, 2009.

[5] BONACHE, J., GIL, I., GARCIA-GARCIA, J. et al. *Split ring resonators: key particles for microwave device design*. Spanisch Conference on Electron Devices, 2005.

Transcom 2011, 27-29 June 2011
University of Žilina, Žilina, Slovak Republic

Dispatch Algorithm for VPP operation

[*]Jan Ivanecky
[*]University of Žilina, Electrotechnical Faculty, Department of Power Electrical Systems, Univerzitná 1, 01026 Žilina, Slovakia, jan.ivanecky@kves.uniza.sk

Abstract. The management of grid connected energy sources operation is of a crucial importance for successful use of renewable energy sources. These renewable sources, storage devices and controllable loads are grouped into virtual power plant (VPP). This paper presents development of dispatch algorithm based on control of renewable energy sources to meet demand of the grid. Algorithm is based on principle of decision tree which is based on some constrains corresponding with particular power generators.

Keywords: renewable energy resources, dispersed generation, virtual power plant, dispatch algorithm.

1. Introduction

Distribution grids are facing tremendous challenges due to several factors. Among them, the most important is the increasing penetration of Distributed Energy Resources (DERs), especially those based on renewable energies [1]. Following the way in which the power system has evolved from conventional structures into structures with more dispersed energy generation, some basic problems can be pointed out. In conventional power system the energy generation takes place in central units. Energy is transported through transmission systems to distribution systems, where is distributed to consumers. The energy flow is one-directional and the system structure corresponds to a “top-down” structure. Disadvantages of this structure are that the produced energy needs to be transported through long distances from generation to consumption points, which is connected with high costs and energy losses. Dispersed generation (DG), based on renewable energy resources (RES), was introduced as a solution to reduce the impact of that problem [2].

Nowadays, in distribution systems, DG units are mainly installed at a low and medium voltage level. Due to the stochastic character of RES and a high number of installed DG new problems are arising, like change of power flow direction, overloading of lines and other system elements, or overvoltages, balancing of power system and frequency control. In order to balance the generation and consumption of energy new solutions were introduced, like network security management systems (NSM), energy storage systems (ESS) or virtual power plants (VPP). In this paper the structure and the dispatch algorithm of a VPP will be described [2].

2. Virtual Power Plant

A virtual power plant is a cluster of dispersed generator units, controllable loads and storages systems, aggregated in order to operate as a unique power plant [2]. The generators can use both fossil and renewable energy source. The heart of a VPP is the dispatch algorithm which coordinates power flows coming from generators, controllable loads and storages. The exemplary structure of a VPP is shown in Fig. 1. The dispatch algorithm can operate according to its targets which can be, for example, the minimization of generation costs, minimization of production of green house gasses and maximization of profits. In order to achieve such targets the algorithm needs to receive information about the status of each unit on the one hand, and on the other hand forecast - especially for renewable units like wind and photovoltaic (PV). Furthermore, the information about possible bottlenecks in the grid plays a relevant role in optimization process of the VPP operation.

Due to the fluctuating nature of renewable energy sources, the prediction of energy production is not an easy procedure. Actually, for wind park, the day ahead forecasting errors are between 9 and 19 % [2]. Due to such errors, power networks with a high penetration of renewable energy sources, can easily have bottleneck and balancing problems.

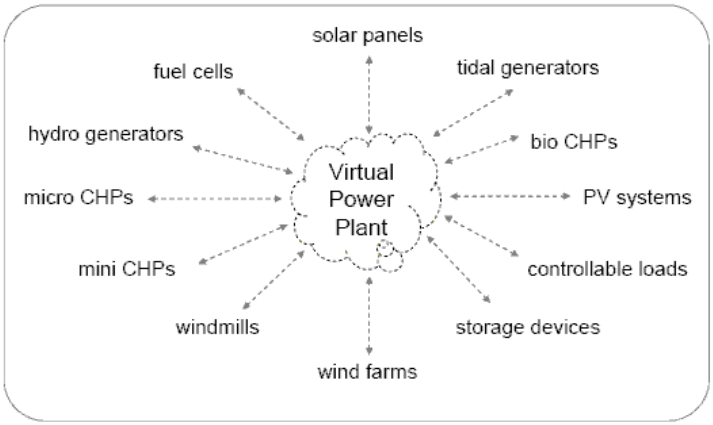

Fig. 1. The exemplary structure of virtual power plant

3. Problem formulation

In this paper we suppose that we have generation sources with following characteristic:

- Wind energy – Nominal power: P_{wind} = 1000 kW.
- Photovoltaic panels – Nominal power: P_{pv} = 800 kW.
- Pumped hydro – Nominal power: P_{water} = 100 kW.
- Biomass – Nominal power: P_{bio} = 500 kW.
- Battery storage – Nominal power: P_{bat} = 200 kW.

The VPP is operated with connection to the grid. The primary objective of dispatch optimization algorithm can vary. For example, economic optimization can either aim to minimization the cost of producing energy or maximizing profit of the VPP [3].

Operational optimization described in this paper is mainly focused on providing electrical energy for grid in the VPP control area with profit achieved from selling of energy.

3.1. Constrains

There are two distinct levels in the control of virtual power plant [4]:

- Dynamic control, which deals with the control of frequency and magnitude of the output voltage of system.
- Dispatch control, which deals with the flow of energy in the system from various sources to grid.

The dispatch algorithm determines the energy flows from various sources like battery storage and different types of renewable generators towards the grid.

Other constrains:

- Wind and photovoltaic energy are free and should be used as often as possible.
- Operation of pumped hydro plant is only possible for some time, after the depletion of water energy is not available.
- Operation of biomass power plant is possible only in range of (50% to 100%) P_{bio}, at lower range the operation is not profitable.
- Battery can operate in range of (20% to 100%) State of Charge (SOC).
- Pumped hydro plant should be operated more than 30% of P_{water}.
- Battery is used in case if options of other renewable sources are exhausted.

4. Dispatch algorithm

First part of decision tree:
Algorithm starts with condition (1):

$$P_{dem} \geq P_{wind} + P_{pv}, \quad (1)$$

where P_{dem} is demanded power,
ΔP is deviation between $P_{wind} + P_{pv}$ and P_{dem},
P_{def} is the deficit power.
If (1) is true, the next condition is:

$$P_{bio} \geq \Delta P > 0.5 \cdot P_{bio}. \quad (2)$$

If (2) is true then biomass generator is starting and $\Delta P = P_{bio}$.
Else, the next condition is

$$P_{bio} + P_{water} \geq \Delta P > P_{bio}. \quad (3)$$

If (3) is true, the next condition is

$$P_{bio} + 0.3 \cdot P_{water} < \Delta P \,\&\&\, P_{water} > 0. \quad (4)$$

If (4) is true then following is valid $\Delta P = P_{bio} + P_{water}$.
If the second part of (4) is not true and $SOC \geq 20\%$ then valid following

$$\Delta P = P_{bio} + P_{bat}. \quad (5)$$

else $SOC < 20\%$ then valid following $\Delta P = P_{bio} + P_{def}$.
If the first part of (4) is not true then

$$P_{bio} < \Delta P \leq P_{bio} + 0.3 \cdot P_{water}. \quad (6)$$

If (6) is true and $SOC \geq 20\%$ then

$$\Delta P = P_{bio} + P_{bat}. \quad (7)$$

If $SOC < 20\%$ && $P_{water} > 0$ then $\Delta P = P_{bio} + P_{water}$,
else $SOC < 20\%$ && $P_{water} = 0$ then $\Delta P = P_{bio} + P_{def}$.
If either (6) is not valid, then $\Delta P < P_{bio}$ and P_{bio} should start. Else will be deficit of power.
If (2 and 3) are not true then following condition is valid

$$\Delta P > P_{bio} + P_{water}. \quad (8)$$

In this case four alternatives can occur:

1. $P_{water} > 0$ && $SOC \geq 20\%$ then $\Delta P = P_{bio} + P_{water} + P_{bat}$,
2. $P_{water} > 0$ && $SOC < 20\%$ then $\Delta P = P_{bio} + P_{water} + P_{def}$,
3. $P_{water} = 0$ && $SOC \geq 20\%$ then $\Delta P = P_{bio} + P_{bat}$,
4. $P_{water} = 0$ && $SOC < 20\%$ then $\Delta P = P_{bio} + P_{def}$.

The last main condition which can be possible for first part of decision tree is

$$\Delta P \leq 0.5 \cdot P_{bio}. \quad (9)$$

And if $\Delta P \geq P_{water}$ there are also four alternatives for this case.

1. $P_{water} > 0$ && $SOC \geq 20\%$ then $\Delta P = P_{water} + P_{bat}$,
2. $P_{water} > 0$ && $SOC < 20\%$ then $\Delta P = P_{bio}$ or $\Delta P = P_{water} + P_{def}$,
3. $P_{water} = 0$ && $SOC \geq 20\%$ then $\Delta P = P_{bio}$ or $\Delta P = P_{bat}$,
4. $P_{water} = 0$ && $SOC < 20\%$ then $\Delta P = P_{bio}$ or $\Delta P = P_{def}$.

If $0.3P_{water} \leq \Delta P < P_{water}$ && $P_{water} > 0$ then $\Delta P = P_{water}$,

else the second part of condition will be $P_{water} = 0$ && $SOC \geq 20\%$

then $\Delta P = P_{bat}$.

else if $SOC < 20\%$ then $\Delta P = P_{def}$.

If $\Delta P < 0.3P_{water}$ && $SOC \geq 20\%$ then $\Delta P = P_{bat}$,

else if $SOC < 20\%$ then $\Delta P = P_{def}$.

Second part of decision tree:

If (1) is not true then is valid following

$$P_{dem} < P_{wind} + P_{pw}. \quad (10)$$

If $\Delta P \geq P_{water} + P_{bat}$ four cases are possible:

1. $P_{water} > 0$ && $SOC = 100\%$ then surplus power is offered in the market,
2. $P_{water} > 0$ && $SOC < 100\%$ then charge surplus power in the battery,
3. $P_{water} = 0$ && $SOC = 100\%$ then water is pumped through,
4. $P_{water} = 0$ && $SOC < 100\%$ then charge battery and pumped water through,

else

$$P_{water} \leq \Delta P < P_{bat} \,\&\&\, P_{water} > 0. \quad (11)$$

If $SOC < 100\%$ then charge battery,

else if $SOC = 100\%$ then surplus power is offered.

If the second part of (11) is not true then valid $P_{water} = 0$ and then surplus power is used for pumping water and if $SOC < 100\%$ then it is used also for charging battery else energy is offered in the market.

If $\Delta P < P_{water}$ && $SOC < 100\%$ then charge surplus power in the battery,

else if $SOC = 100\%$ then surplus power is offered in the market.

5. Conclusion

At present, control of renewable resources as a virtual power plant seems to be a right concept due to the increasing number of dispersed generation. The concept of VPP was developed to enhance the visibility and control of system operators and market actors to DERs by providing an appropriate technical and commercial interface between these system components.

This paper describes simply dispatch algorithm of VPP operation. This operation strategy will be verified when models of all parts of VPP will be build.

References

[1] KIENY, C., BERSENEFF, B., HADJSAID, N., BESANGER, Y., MAIRE, J., *On the concept and the interest of virtual power plant: Some results from the European project Fenix.* Power & Energy Society General Meeting, 2009.

[2] LOMBARDI, P., POWALKO, M., RUDION, K.., *Optimal operation of a virtual power plant.* Power & Energy Society General Meeting, 2009.

[3] SALMANI, M. A., TAFRESHI, S. M. M., SALMANI, H., *Operation optimization for a virtual power plant*. Sustainable Alternative Energy (SAE), 2009.

GUPTA, A, SAINI, R. P, SHARMA, M. P, *Computerized modelling of hybrid energy system – Part I: Problem formulation and model development*. Electrical and Computer Engineering, 2008.

Transcom 2011, 27-29 June 2011
University of Žilina, Žilina, Slovak Republic

Analysis of the electromagnetic effects on the power transformer winding and its insulation

*Jozef Jurcik,
*University of Žilina, Faculty of Electrical Engineering, Department of Measurement and Applied Electrical Engineering, Univerzitna 1, 01026 Žilina, Slovakia, jozef.jurcik@fel.uniza.sk

Abstract.
This article is about electromagnetic effects on transformer winding. It shows dimension of force causing by short-circuits and how this force is created. In graphs are shown basics dependences for transformer and its dimension (its power) and arosed forces. In the next is dealing with transient actions at overvoltages. There is showed how can overvoltages be created and how long overvoltages are take time. Third part of article is focused on measurement method. This method is preferred for testing big transformer. In method are described frequency ranges and possible exploitation of this method. Conclusion is proposal for next leading of this issue.

Keywords: short-circuit, electrical forces, measurement, transformer, winding, current, electromagnetic effect.

1. Introduction

The state of the transformer insulation depends on many actions. These actions have effect on transformer over time. So the insulation of the transformer is not only liable to ageing. In this paper are inscribed some actions affecting on transformer winding and ultimately actions affecting on transformer insulation. First we describe basic transient actions in transformer and then we adduce non-invasive method for insulation defect on which application I am working.

2. Short-circuit on output winding.

Short circuit of output winding in transformer is disrepair state. At its calculations we usually suppose that his input voltage doesn't decrease (transformer is connected on so called hard network). Short-circuit means big dangerous for the transformer. At short-circuit high currents flow across the transformer, which not only heat the transformer but they create electromagnetic forces too, which can be the reason of damage of transformer winding.

Thermal ageing of transformer oil is caused by local overheating, when molecular movement reaches so intensity, that labile binding between molecules start disengaging. There are gases which are created by the dissociation of transformer oil or solid substance too (e. g. crystalline carbon or coke) which had degrading effect on insulation. But this process has no effect on degrading oil [1].

Transient action in small transformer responses is during the one flick. In huge transformer it is during 6 to 7 oscillation. We define the time of response of transient action from (1) where Lk and Rk is inductance and resistance of transformer in short-circuits.

$$t \approx 3\frac{L_k}{R_k} \qquad (1)$$

Although transient action is short, is big dangerous for winding. Electromagnetic forces effecting on the individual conductor of winding are given conjunction of inductance of stray flux and current in conductor.

$$F \approx B \cdot i\left[Nm^{-1}; T, A\right] \qquad (2)$$

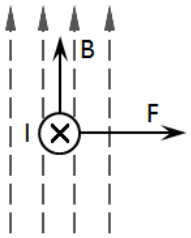

Fig. 1. Relation between inductance B, current I and electromagnetic force F.

At normal loading of transformer the forces effecting on wires are small. For example at current I = 75A and inductance B = 0,2T the force is

$$F \approx 0{,}2 \cdot 75 \approx 15 Nm^{-1} \qquad (3)$$

This force can't deform insulation of coil winding, as you can see. At short-circuit B.i rise in proportion to i^2 and in the moment of the biggest value of current, force F rise k_k[1] times. On the figure 2 is showed the biggest current in the worst cases. It reaches $k_k = 30$ and more. So force F can rise on almost 1000 times. This is force almost 15 000N. This force can destroy insulation very simple even further transformer winding too.

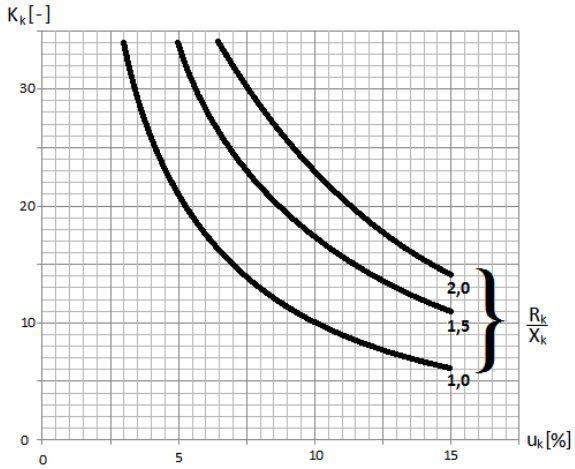

Fig. 2. Dependence of the biggest short-circuit current on the nominal current amplitude in dependence of u_k and $\frac{R_k}{X_k}$ [3].

3. Transient actions in transformer winding at overvoltage.

The transformer work in operation with normal condition is a sinusoidal voltage of nominal frequency between separate parts of its winding and between a winding and a grounded tank. If is correctly designed and manufactured its insulation, this voltage is safe for the transformer.

Transformer in operation is often given to a voltage effects, greatly crippling normal working voltage with another frequency and shape. In electric system on which is transformer connected, is often created overvoltage; that can be effect of normal working operation (turn on, switch off transformer or electric line) or state of disrepairs, which are created in electric line (for example short-circuit, intermittent arc connection with ground in network with insulated neutral wire etc.). Overvoltage can be created by a straight stroke of lightning to the electrical line or pole and also at indirect lightning discharges which are induced in a line wire of electromagnetic wave with a high voltage.

[1] coefficient of dependence of the biggest short-circuit current on the nominal current amplitude (fig. 2)

Overvoltage has a character of short-time electric pulses or periodic waves. There can be created electromagnetic waves with different frequencies, because the system includes inductions or capacitances.

At free oscillations can arise dangerous voltage which are dangerous not only for winding insulation towards ground but also for insulation between adjacent coils and windings too. The most dangerous stress is on the insulation of the first coils and windings eftsoon of initial voltage or fast decrease of voltage in case of “trap wave”. We can assessment trap wave as a superposition of two aperiodic waves with different polarity, which go consecutively provided the second wave has abrupt leading edge [2].

Small electric discharge can be created at overvoltage. At plain electric discharge the temperature of oil rise. This temperature is moving around 100°C (±20°C). In this case the hydrogen, which is product of aromatic hydrocarbon, is released. At 160°C (±40°C) temperature is possible to observe hydrogen, marsh gas and ethylene. We can proceed to create higher hydrocarbons like acetylene or clear crystalline carbon in those two cases (it is created at 1000°C). We are able to determine the palette of the various gases with this method. So we can predict the size of currents (ultimately electrical discharges) which was overran by transformer in backward assumption. Here we can see relation between electromagnetic effects and transient actions at overvoltages.

4. SFRA method.

Because the consequence of the electromagnetic stresses and transient actions at overvoltages are the same we need some diagnostic method for detect their consequences.

SWEEP frequency response analysis is a sensitive diagnostic technique for detecting changes in the electrical characteristics of power transformer windings. Such changes can result from various types of electrical or mechanical stresses (shipping damage, short-circuit forces, etc.). The test is non-destructive and non-intrusive and can be used either as a stand-alone tool to detect winding damage, or as a diagnostic tool combined with other tests (e.g. insulation power factor, frequency domain spectroscopy (FDS), insulation resistance, winding resistance or dissolved gas analysis).

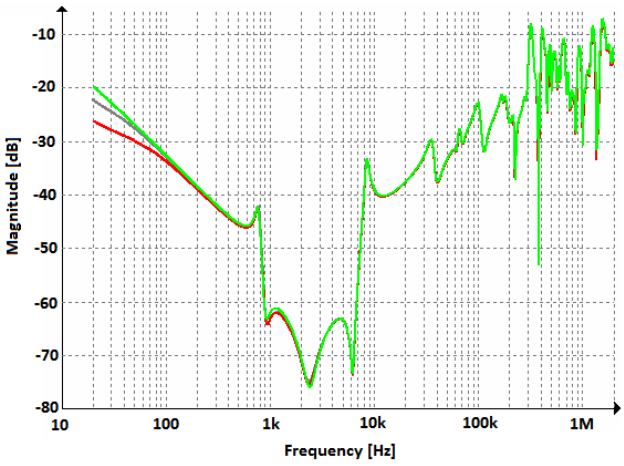

Fig. 3. Measurement of HV winding on transformer using SFRA method [4]

5. Conclusion

Seemingly basic transient actions which are running during transformer operation intervene to state of insulation in various difficult steps. How we it describe the transient actions have different basis but the effect on insulation is similar. We can develop methods for revealing of her damage.

On basics of these methods (such as FDS for example) we can monitor the state of the transformer in operation which has big meaning for operation.

Acknowledgments

This work was supported by the Grant Agency VEGA from the Ministry of Education of Slovak Republic under contract 1/0548/09.

References

[1] GUTTEN, M., KUČERA, S., KUČERA, M., ŠEBÖK, M.: Analysis of power transformers reliability with regard to the influences of short-circuit currents effects and overcurrents, p.62-64, R.85 NR 7/2009 - ISSN 0033-2097

[2] JEZIERSKI, E: Transformers. Theoretical basis, Academia Praha, 1973, Czech Republic

[3] PETROV, G. N.: Transformers, Academia Praha, 1980, Czech Republic

[4] WERELIUS P., ÖHLEN M., ADEEN L., BRYNJEBO E.: Measurement Considerations using SFRA for Condition Assessment of Power Transformers, In: International Conference on Condition Monitoring and Diagnosis, Beijing, China, April 21-24, 2008,

Transcom 2011, 27-29June 2011
University of Žilina, Žilina, Slovak Republic

Synthesis of LCLC Type Power Resonant Filter with Integrated Transformer

*Slavomir Kascak, *Jozef Sedlak
*University of Žilina, Faculty of Electrical Engineering, Department of Mechatronics and Electronics, Univerzitna 1, 01026 Žilina, Slovakia, {slavomir.kascak, jozef.sedlak}@fel.uniza.sk

Abstract. The paper deals with design analysis and synthesis of power resonant filter used for creating of sinusoidal voltage for sensitive load. The filter has to remove higher harmonic components from the supplying voltage to reach the harmonic distortion roughly 5% in the whole range of the load (0-100%). The LCLC filter can be supplied from either single-phase voltage inverter in full- or half- bridge connection, or from simple DC/DC buck converter. Non-symmetrical control causes higher contents of the harmonics, odd and even ones. Simulation results based on designed parameters and worked-out from Matlab and OrCad models confirm good quality of output quantities, voltage and current.

Keywords: LCLC resonant filter, transfer function, Fourier analysis, Bode diagram, transformer ratio

1. Basic Connection of LCTLC Converter with Output Resonant Filter and Transformer

In case of demand of the harmonic sinusoidal voltage for critical load, it is necessary to use some of resonant filter types. One of suitable is LCLC type tuned to basic harmonic [1], [3]. The LCLC filter can be supplied by either single-phase voltage inverter in full- or half- bridge connection, or simply from DC/DC buck converter [2]. Because of non-full-bridge connection of the converter the voltage transformer has to be used for increasing of output voltage, Fig. 1.

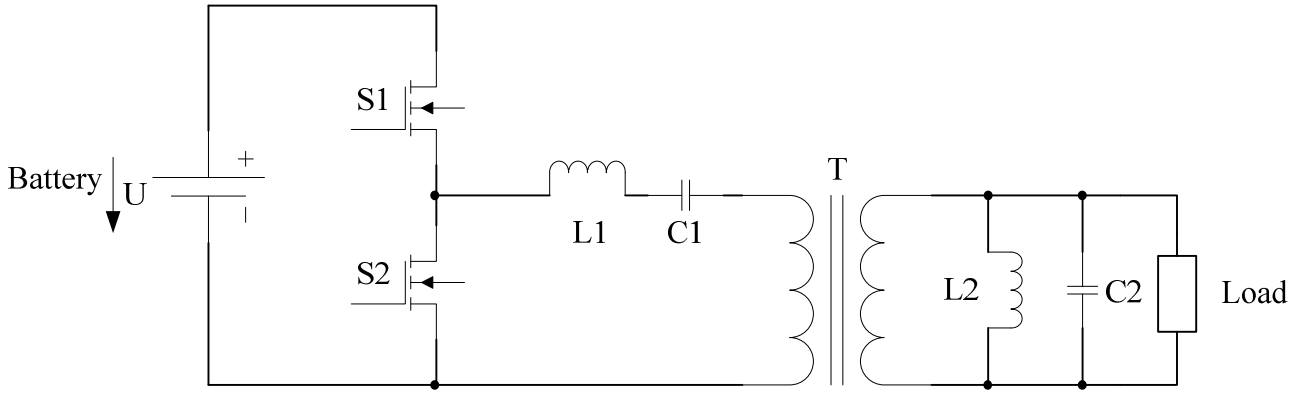

Fig.1. Schematic diagram of LCTLC converter with output resonant filter and transformer

1.1 Non-Symmetrical Control of the Converter with Output Resonant Filter and Transformer

Output voltage of the converter comprises also DC component with is captured and separated by C1 capacitor. Beside this DC voltage component can be chanced due to controlled duty cycle of converter during battery voltage changing. Non-symmetrical control causes higher contents of the harmonics, odd and even ones [3], Fig. 2. Using Fourier analysis one can derive relation (1) for basic harmonic amplitude of output voltage of converter

$$\frac{U_1(\beta)}{U} = \frac{\sqrt{2}}{\pi}\sqrt{1-\cos(\beta)} \ldots\ldots \left(= \frac{2}{\pi}\sin(\beta/2) \right) \qquad (1)$$

Where $U_{1M(\beta)}$ is magnitude of fundamental harmonic depending on voltage pulse width β

U maximum value of inverter input DC voltage

β voltage pulse width in the range of 0-180 °el. deg., whereas β = π - α, and

α control angle oriented from end of half-period to the end of positive voltage pulse.

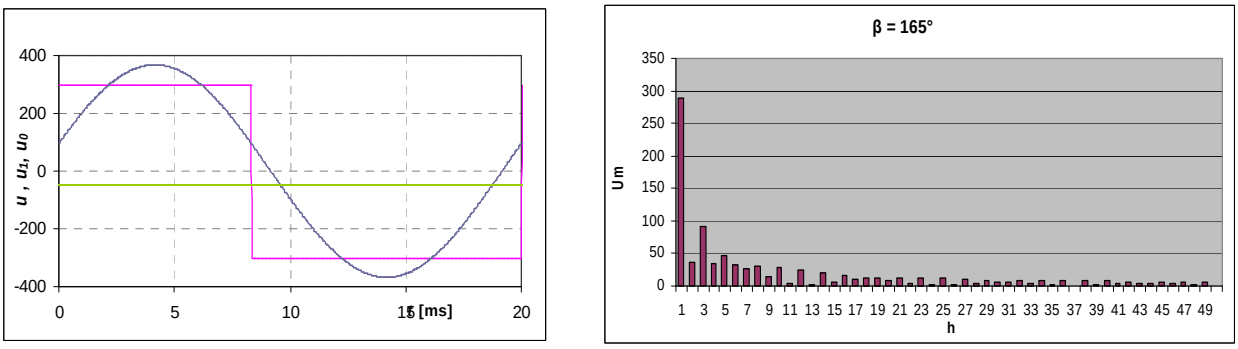

Fig. 2a,b. The output voltage of the converter with non-symmetrical control 165/180°el (a) and its harmonic content without filtering (b) [3]

2. Design analysis and Synthesis of LCTLC Filter Parameters

2.1. Design of L1C1 and L2C2 parameters

Resonant frequency of L1C1 and L2C2 should be the same as basic fundamental frequency of the converter and is requested by load demands. So, based on Thomson relation

$$\omega_{res} = \sqrt{\frac{1}{L_1 C_1}} = \sqrt{\frac{1}{L_2 C_2}} \text{ or, respectively } L_1\omega_{res} = \frac{1}{\omega_{res} C_1} = L_2\omega_{res} = \frac{1}{\omega_{res} C_2} \qquad (2)$$

where $\omega_{res}$is equal 2π× fundamental frequency of the converter. Theoretically, $\omega_{res}L_1$ and other members of (.) can be chosen from wide set. Not to exceed nominal voltages and currents of the accumulative elements we take value of the nominal load ($|Z_{load}|$). Then

$$L_1 = \frac{U_1^2}{\omega_1 P_1} \cdot k$$

$$C_1 = \frac{P_1}{\omega_1 U_1^2} \cdot k$$

$$L_2 = \frac{U_1^2}{\omega_1 P_1} \cdot \frac{1}{k} \qquad 3(a,b,c,c,d)$$

$$C_2 = \frac{P_1}{\omega_1 U_1^2} \cdot \frac{1}{k}$$

k quality factor is ratio of component impedance L_1,L_2,C_1 and C_2 to load impedance.

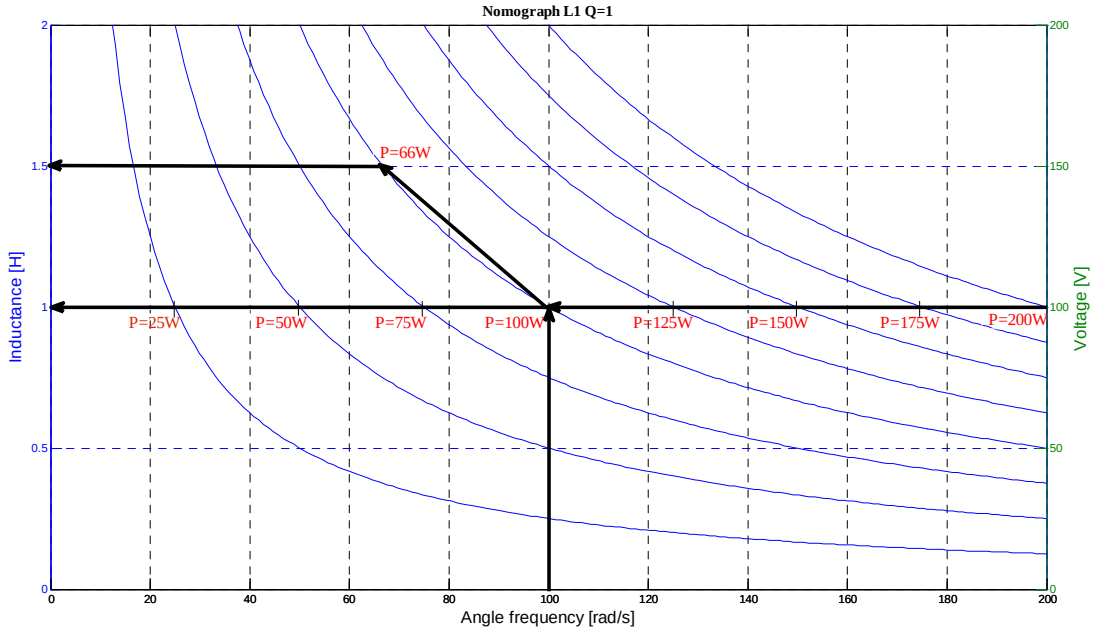

Fig. 3. Nomograph for determination of L_1 inductance knowing frequency, voltage and power of the load

2.2. Voltage Transfer Function Determination

Transfer function is defined as ratio of output voltage to input voltage, usually in Laplace form. To determine it one need to know impedance of series- and parallel part of the filter including transformer, Fig. 4.

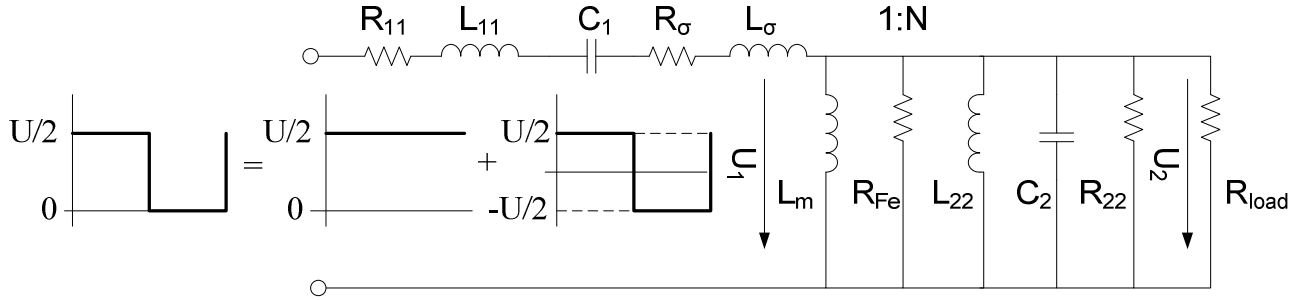

Fig. 4. Schematic diagram of LCTLC converter with output resonant filter and equivalent circuit of transformer

The leakage inductance L_σ of the transformer can be added to series inductance L_{11} of *LCLC* filter as well as the sum of winding resistances R_{11} and R_σ creates resistance R_1. L_m is magnetizing inductance of transformer and R_{Fe} represents iron losses in transformer. So,

$$\begin{aligned} R_1 &= R_{11} + R_\sigma \\ R_2 &= R_{Fe} + R_{22} + R_{load} \\ L_1 &= L_{11} + L_\sigma \\ L_2 &= L_m + L_{22} \end{aligned} \qquad 4(a,b,c,d)$$

For transfer function then we get (in the Laplace form)

$$Z_1(p) = R_1 + pL_1 + \frac{1}{pC_1};\; Z_1(p) = \frac{R_1 pC_1 + p^2 L_1 C_1 + 1}{pC_1};\; Z_1(p) = \frac{p^2 + p\dfrac{R_1}{L_1} + \dfrac{1}{L_1 C_1}}{p\dfrac{1}{L_1}}$$

$$Y_2(p)=\frac{1}{R_Z}+pC_2+\frac{1}{pL_2}\rightarrow Z_2(p)=\frac{1}{1/R_Z+pC_2+1/pL_2}=\frac{pL_2}{pL_2/R_Z+p^2L_2C_2+1}=\frac{p\frac{1}{C_2}}{p^2+p\frac{1}{R_ZC_2}+\frac{1}{L_2C_2}}$$

$$Z(p)=Z_1(p)+Z_2(p)= \frac{p^4+p^3(\frac{R_1}{L_1}+\frac{1}{R_ZC_2})+p^2(\frac{1}{L_1C_1}+\frac{R_1}{L_1}\frac{1}{R_ZC_2}+\frac{1}{L_2C_2}+\frac{1}{L_1C_2})+p(\frac{1}{L_1C_1R_ZC_2}+\frac{R_1}{L_1}\frac{1}{L_2C_2})+\frac{1}{L_1C_1L_2C_2}}{p^3+p^2\frac{1}{L_1R_ZC_2}+p\frac{1}{L_1L_2C_2}} \quad (5)$$

Output voltage of the filter can be expressed as product of input current and Z2 impedance. Since input current is input voltage divided by total impedance, the output voltage is ratio Z2 impedance and total impedance times input voltage. So finally one get

$$U_2(p)=\frac{U_1(p)}{Z(p)}\cdot Z_2(p)=U_1(p)\cdot\frac{1}{Z(p)}\cdot\frac{p\frac{1}{C_2}}{p^2+p\frac{1}{R_ZC_2}+\frac{1}{L_2C_2}}$$

$$\frac{U_2(p)}{U_1(p)}=\frac{p^2\frac{1}{L_1C_2}}{p^4+p^3(\frac{R_1}{L_1}+\frac{1}{R_ZC_2})+p^2(\frac{1}{L_1C_1}+\frac{R_1}{L_1}\frac{1}{R_ZC_2}+\frac{1}{L_2C_2}+\frac{1}{L_1C_2})+p(\frac{1}{L_1C_1R_ZC_2}+\frac{R_1}{L_1}\frac{1}{L_2C_2})+\frac{1}{L_1C_1L_2C_2}} \quad (6)$$

Using *Bode* (*f*) MatLab function is possible to present the voltage transfer function in graphical form as Bode diagram. For designed parameters

R_1=0.01 Ω; L_1=0.0228 H; C_1=444e-6 F; L_2=0.674 H; C_2=15e-6 F; R_2=211.6 Ω; $U_1=\sqrt{2}.24$ V, U_2=325V, r=9.57

the magnitude- and phase- characteristics of the voltage transfer function in frequency domain have been obtained, Fig. 5.

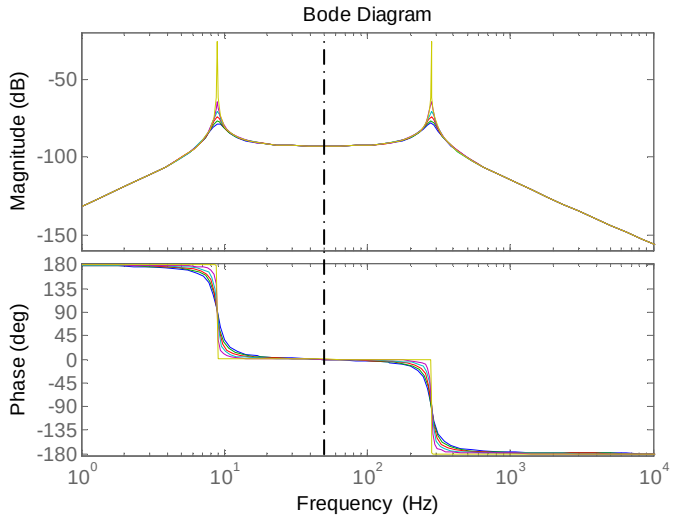

Fig. 5. Bode diagram of voltage transfer function (4) for fundamental frequency of 50 Hz

Based on worked-out diagram it can be investigate properties of the filter in greater detail (quality, sensitivity, bandwidth, THD). There is shown in Fig. 6a,b and 7a,b good quality of filter output voltages.

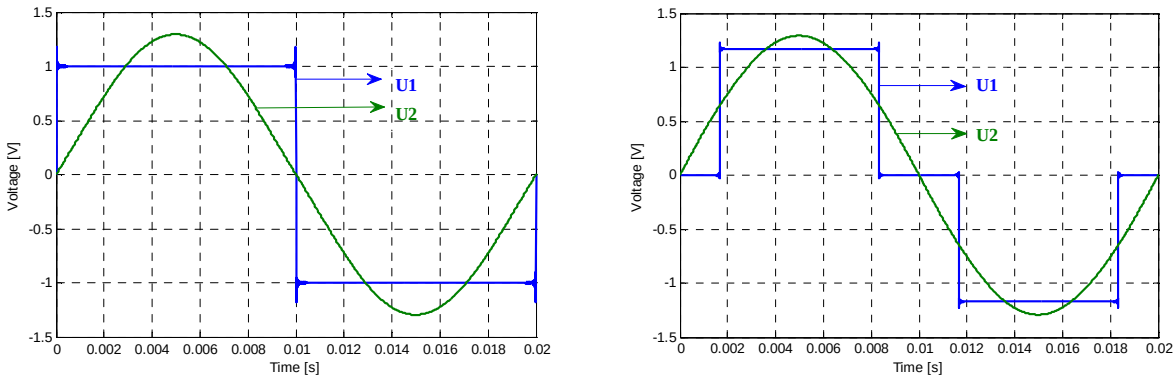

Fig. 6a,b. Output voltage $U_2$of thefilter for 180 deg.(a) and 120deg. (b) of pulse width $\beta$of the inverter output voltage U_1

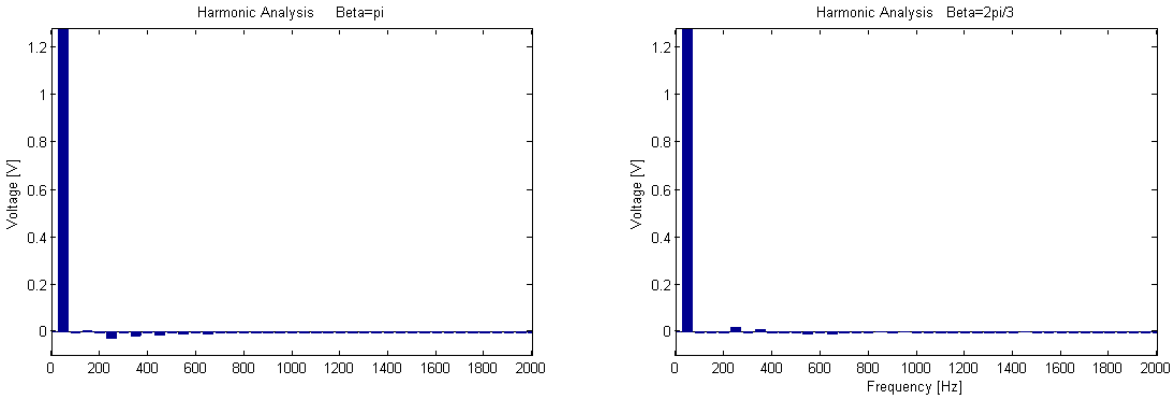

Fig. 7a,b. Harmonic analysis of output voltage U_2 for 180 deg. (a) and 120 deg. (b) of pulse width β of the inverter output voltage U_1

The total harmonic distortion *THD*of output voltage U_2 can be 5 -10 % in dependency onquality parameter*k* from the range of 1 to 2.

2.3. Transformer Ratio Calculation

When battery voltage and output voltage U_2 and frequency of the filter are set then transformer ratio can be calculated. Based on (1) the effective (RMS) value of the fundamental harmonic is determined

$$U_1 = \frac{\sqrt{2}}{\pi} U sin\left(\frac{\beta}{2}\right) \tag{5}$$

So, transformer ratio will be

$$r = 1{:}N = \frac{U_1}{U_2} \tag{6}$$

Transformer design is in detail described in paper [4]. During charging and discharging of the battery the value of the first harmonic of the primary voltage of the transformer is controlled to be constant.

Then voltage pulse width βshould be

$$\beta = 2arcsin\left(\frac{\pi U_1}{\sqrt{2}U}\right) \tag{7}$$

Dependency of battery voltage on voltage pulse width β of the inverter (and vice versa) is shown in Fig. 8.

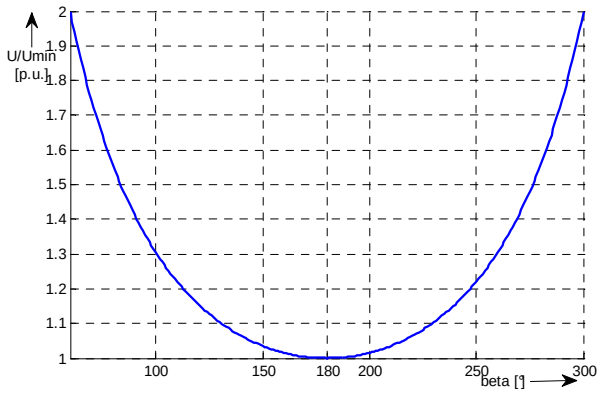

Fig.8. Dependency of battery voltage (p.u.) on pulse width $\beta$of the inverter output voltage

The operating range of battery voltage is supposed +20 % -30 %.

3. Conclusions

Design of LCLC typepower resonant filter parameters is presented in the paper.The filter has to remove higher harmonic components from the supplying voltage to reach the harmonic distortion roughly 5% in the whole range of the load (0-100%).Contrary to [3] simple DC/DC buck converter has been used as power supply. Non-symmetrical control of the converter makes it possible to hold the value of output voltage to be constant. Voltage transfer function has been derived using Laplace transform and Bode MatLab command.Simulation results based on designed parameters and worked-out from Matlab and OrCad models confirm good quality of output quantities (Fig. 6a,b.), voltage and current.Harmonicanalysisof outputvoltagealsoconfirms thegoodquality of LCLC filter (Fig. 7a,b.).

Acknowledgement

The authors wish to thank for the financial support to R&D operational program Centre of excellence of power electronics systems and materials for their components No. OPVaV-2008/2.1/01-SORO, ITMS 26220120046 funded by European regional development fund (ERDF) and VEGA Agency for the project No. 1/0470/09.

References

[1] BATARSEH I., *Resonant Converter Topologies with Three and Four Storage Elements.* IEEE Transaction on Power Electronics, Vol. 9, No.1, January 1994, pp. 64-73.

[2] ANG,Y.A., FOSTER,M.P., BINGHAM,C.M., STONE,D.A., SEWELL,H.I., HOWE,D..*Analysis of 4th-Order LCLC Resonant Power Converters*. Proc. of IEE Electrical Power Applications, Vol. 131 (2004), No. 2, pp.169-181.

[3] DOBRUCKY, B.,BENOVA, M., KASCAK,S., *Transient Analysis and Modelling of 2nd- and 4th-Order LCLC Filter under Non-Symmetrical Control*. Electronics and Electrical Engineering, Vol. 4(110), 2011,pp. 7 -12.

[4] RADVAN, R., DOBRUCKY, B., FRIVALDSKY, M., RAFAJDUS, P., *Modelling and Design of HF 200 kHz Transformers for Hard- and Soft- Switching Application.* Electronics and Electrical Engineering, Vol. 4(110), 2011, pp.7-12.

Transcom 2011, 27-29 June 2011
University of Žilina, Žilina, Slovak Republic

Design Analysis of Two-Stage Power Electronic Converter for Feeding of 2-Phase PMSM

[*]Jan Kassa, [**]Peter Sekerak, [*]Michal Prazenica,
[*]University of Žilina, Faculty of Electrical Engineering, Department of Mechatronics and Electronics,
Univerzitna 1, 01026 Žilina, Slovakia, {jan.kassa, michal.prazenica}@fel.uniza.sk
[**]University of Žilina, Faculty of Electrical Engineering, Department of Power Electrical Systems,
Univerzitna 1, 01026 Žilina, Slovakia, {peter.sekerak}@kves.uniza.sk

Abstract. The paper deals with power electronic two-phase motor drive system with two-stage converter and PMSM motor. The proposed system consists of two-stage converter comprises: input resonant/boost converter with AC or DC output, two-phase matrix converter commutated by HF AC input voltage or VSI inverter, and two-phase synchronous motors. Such a system with AC interlink, in comparison with currently used conventional system configurations features a good efficiency of electronic converters (due to soft switching of both converters) and also good torque overloading of two-phase AC synchronous motors (more than 3-times). Results of simulation experiments are given in the paper.

Keywords: Two-stage electronic converter, resonant LLC converter, direct matrix converter, two- phase AC motor, computer simulation.

1. Introduction – Basic Concepts of Two-Stage Power Electronic Converter (PEC)

The concept of classical AC controlled electric drive is based on PEC feeding AC motors (synchronous or induction ones). Usually, 3-phase VSI inverter and 3-phase AC motors are used. There is shown as example for electric vehicle drive [1] in Fig. 1.

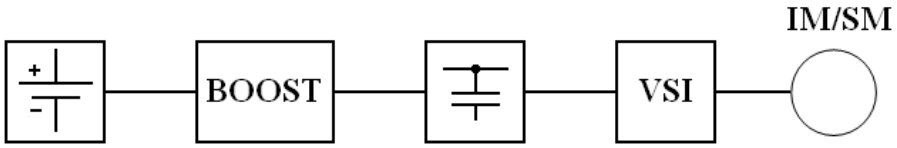

Fig. 1. Block diagram of electric drive with boost converter, DC link, 3-phase VSI inverter and 3-phase AC motor [4].

In case of AC network supply (industrial-, home appliances) the first stage can be created by increasing or compensating rectifier with power factor corrector (PFC), Fig. 2.

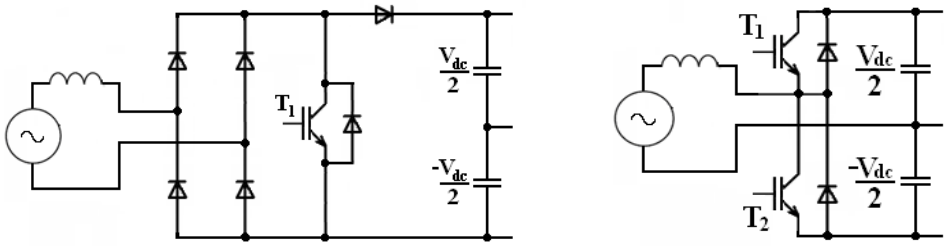

Fig. 2. Increasing rectifier with compensating PFC corrector in full-bridge (a)- and half-bridge (b) connections.

In spite of good properties of three-phase systems, the 2-phase propulsion system offers also some further advantages. Such a two-phase system denotes by much higher transferred power (2.6-times) and by better utilization of semiconductor switches (~ 2-times), [2], [3] under the same input

voltage. There is no need a boost converter, since the phase voltage of each of single-phase inverters is exactly 2-times higher that of 3-phase inverter phase voltage. Also, 2-phase AC induction motor has starting torque 4- times higher than nominal one [4], since 3-phase motor just one. Two single-phase inverters instead of one 3-phase inverter have, of course, drawback of higher number of semiconductor switches (8 instead 6). Therefore, there are in the next text, presented further modification of two-phase converter system to neglect or to decrease mentioned disadvantage.

The first change is using of half-bridge connection where number of semiconductor switches is just 4 instead of 6. Its phase voltage is equal to phase voltage of three-phase connection. For the first (fundamental) harmonic component

$$U_{1\mathrm{FAZ}} = \frac{4}{\pi}\frac{U_{\mathrm{DC}}}{2\sqrt{2}} = \frac{2}{\pi\sqrt{2}}U_{\mathrm{DC}} = \frac{\sqrt{2}}{\pi}U_{\mathrm{DC}}$$

the same value as for 3-phase VSI inverter, but number of phases is 2 instead of 3. So, when increasing DC voltage by the value of √(3/2) (~22 %) the output power will be the same as in case of 3-phase system (‘cause power is related to square value of voltage). Contrary to [2], [3], a new point of view is using of synchronous AC motor instead of induction one as referred in Chap. 3. Basic block scheme of converter chain is depicted in Fig. 3.

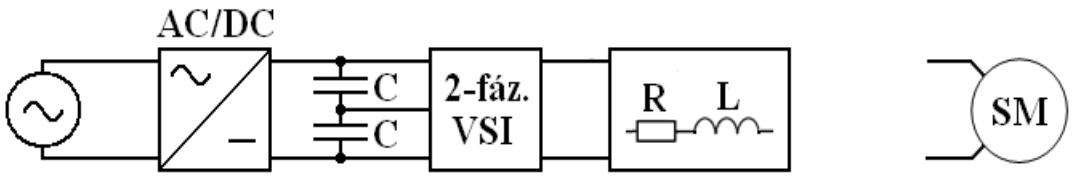

Fig. 3. Block scheme of 2-stage 2-phase converter chain with VSI inverters in half-bridge connection and RL/PMSM load.

Power circumstances under RL load are shown in Fig.4.

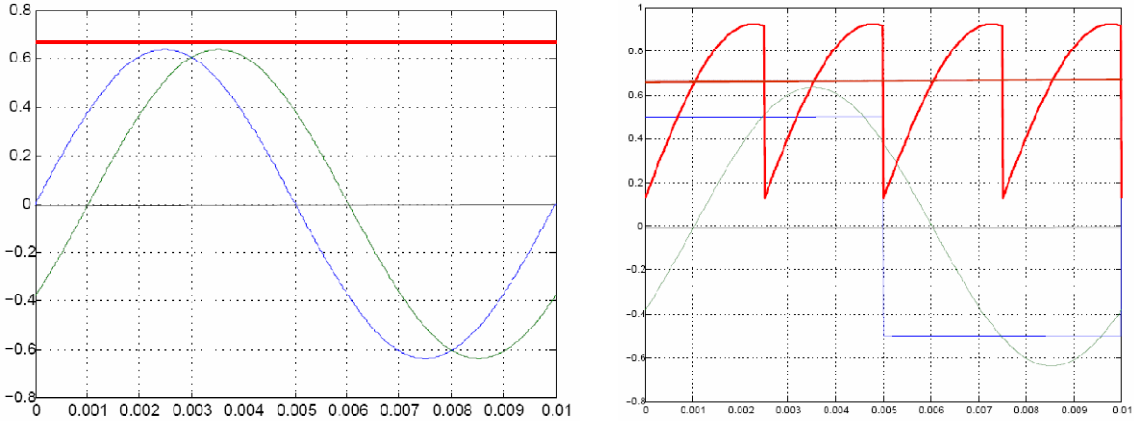

Fig. 4. Time-waveforms of instant first harmonics active power of 2-phase converter (a) and instant power of phase voltage and first harmonic current (b) under RL load.

Output power of 2.phase converter under RL load is

$$S_{2\mathrm{F}} = 2\left(\frac{\sqrt{2}}{\pi}U_{\mathrm{AB}}\right)^2 \cdot \frac{1}{|Z|} = \frac{4}{\pi}\frac{U_{\mathrm{AB}}^2}{|Z|} \qquad [V.A]$$

thus just 2/3 of 3-phase converter power. For reaching of full power is necessary to increase DC voltage to the value

$$\frac{S_{2F}}{S_{3F}} = \frac{2}{3} \text{ teda, ak } U_{1FAZ} = 230\,V \rightarrow U_{AB} = \sqrt{\frac{3}{2}}.\frac{\pi}{\sqrt{2}}.230 = 517\,V.$$

2. Designing Two-Stage PEC

2.1. Choice of the First Stage Converter

There are some suitable types of converter which can be used as input part of 2*stage converter system:

- switched mode converter, Fig. 5a,
- resonant pole converter, Fig. 5b,
- resonant LCC converter, Fig. 5c
- asymmetric duty cycle converter, Fig. 5d.

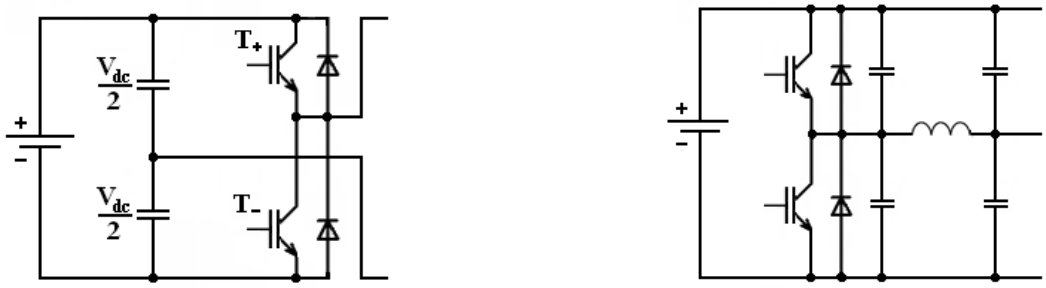

Fig. 5a,b. Principle circuit diagram of switched PWM (a)- and resonant pole (b) inverters [7] in half-bridge connection.

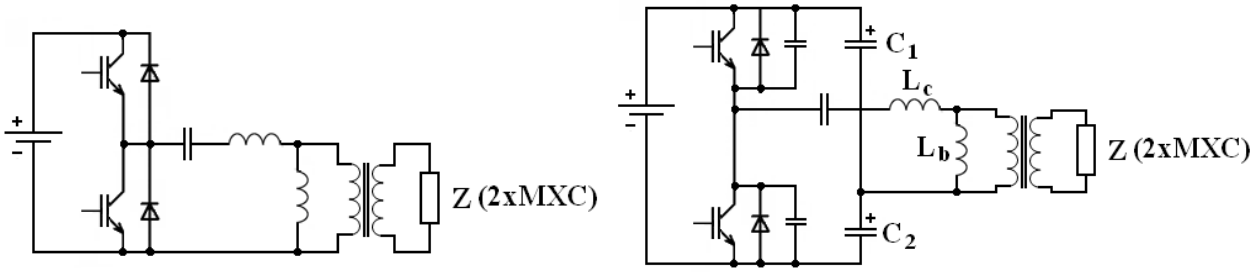

Fig. 5c,d. Principle circuit diagram of resonant LLC (a)- and asymmetric duty cycle (b) converters [8] in half-bridge connection.

Evaluation of these four types is done in [8]:

Switched Mode Converter: PWM switch mode converters have among the lowest conduction losses of all the converter circuits. On the down side, PWM converters are “hard switch” circuits that suffer from high switching losses, which limit their usefulness at high frequencies.

Resonant Pole Converter: Resonant pole or phase shift converters also switch losslessly, and their operation seems in many respects to mimic switch mode converters. The one feature they do not mimic, however, is the low conduction loss of switch mode converters. This fact is an undesirable result of the freewheeling idle current required to flow in the primary side circuit during the dead-time between conduction intervals.

Resonant LLC Converter: The undesirable switching losses of switch mode converters lead designers to the resonant class of converters that eliminate switching losses, opening the door to higher frequencies and physically smaller converters. However, these converters pay a heavy price in high conduction loss and large peak currents and voltages.

Asymmetric Duty Cycle Converter: The asymmetric duty cycle converters combine the best features of these circuits. Their conduction losses are as low as switch mode circuits, and they switch losslessly like resonant circuits. Timing difficulties can limit their maximum frequency to something less than that which is attainable by true resonant circuits, and the boundary condition

requirements for lossless switching are somewhat more restrictive than for resonant pole converters. In many cases, however, these drawbacks are acceptable because of the benefit of low conduction loss and the elimination of switching loss.

Based on above evaluation we choose the asymmetric type of input converter for the 2-stage converter system for further description and analysis of the system. Design equations are given in [8] (simpler forms of them see appendix).

2.2. Choice of the Converter Second Stage of the Converter

Focusing on half-bridge connection of second stage converter (see above) there are two suitable scheme of the converter. The first one is with DC voltage interlink and two single-phase VSI inverters, Fig. 6.

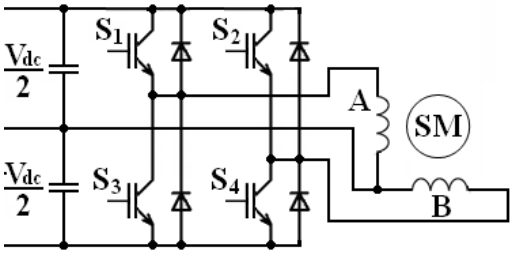

Fig. 6. Circuit diagram of second stage inverter: 2 single phase VSI inverters in half-bridge connection.

The second one uses HF transformer with AC voltage interlink and two matrix half-bridge converters, Fig. 7.

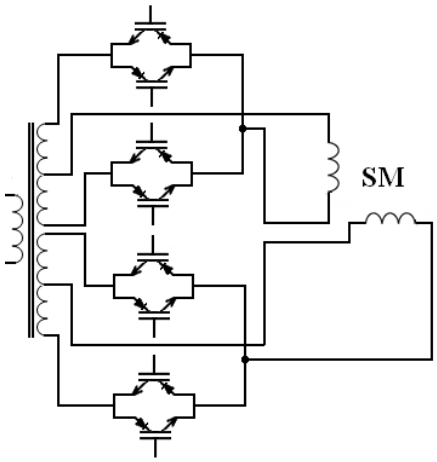

Fig. 7. Circuit diagram of second stage inverter: 2 single phase matrix converters in half-bridge connection.

Let's aware the output voltages of both types of converter will be, under the same switching frequency, the same. According to half-bridge the bipolar PWM modulation have to be used, Fig. 8.

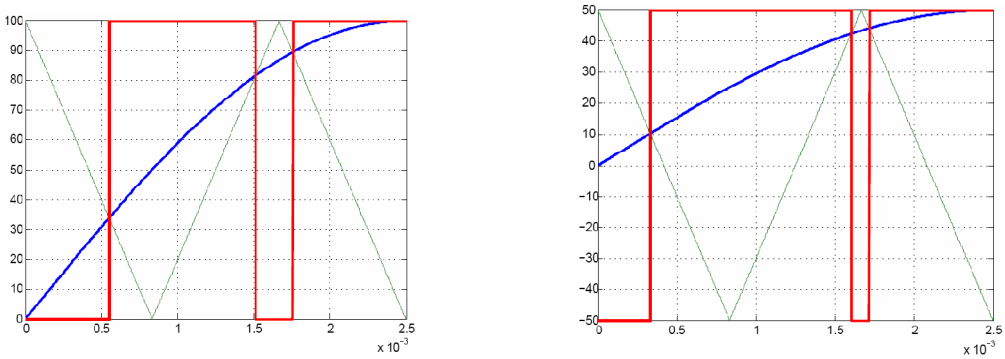

Fig. 8. Principle waveforms of phase voltage of VSI or matrix half-bridge converters under PWM modulation..

The magnitudes of the first fundamental harmonics of each pulse can be calculated when knowing the width of each pulse (t_I, t_{II}, t_{III}) given by coincidence of triangle and sinusoidal reference curves.

Then

$$U_{1\mathrm{MI,II,III}} = \frac{4}{\pi} U_{\mathrm{DC}} \sin \frac{\omega t_{I,II,III}}{2} \cos\left(w_{I,II,III}\right)$$

where t_I, t_{II}, t_{III} are width of pulses, and w_I, w_{II}, w_{III} are angles between axes of pulses and symmetry axis in the middle of half-period, respectively.
Total magnitude of the first (fundamental) harmonic is given [..]

$$U_{1M} = 2\, U_{1MI,II} + U_{1MIII}$$

and its RMS value

$$U_{1RMS} = U_{1M} / \sqrt{1}.$$

The total RMS value of the pulses

$$U_{\mathrm{RMS}} = \sqrt{2U_{\mathrm{RMSI,II}}^2 + U_{1\mathrm{RMSIII}}^2}$$

where $U_{\mathrm{RMSI\text{-}III}}$ are RMS value of single pulses.

Switching frequency will be of coarse higher than in Fig. 8. It is supposed to be about 5 kHz for VSI inverter with hard commutation, and 20-40 kHz for matrix converter schemes.

2.3. Considering Power Losses - Evaluation and Comparison

Average value of total power losses can be determined [11]

$$P_{tot(AV)} = f \cdot (W_{on} + W_{cond} + W_{off})$$

where W_{on} is loss energy during switching-on
W_{cond} loss energy during conduction state
W_{off} loss energy during switching-off
f working frequency of the switches

Pre výpočet spínacích strát som použil nasledovné katalógové údaje [12]:

- zapínací/vypínací čas IGBT tranzistora 130/445 ns
- úbytok napätia na IGBT tranzistore/dióde v režime vodivosti 3/0,8 V
- dynamický odpor spätnej diódy IGBT tranzistora 18 mΩ
- doba záverného zotavenia diódy 0,4 ms
- komutačný náboj diódy 7 µC

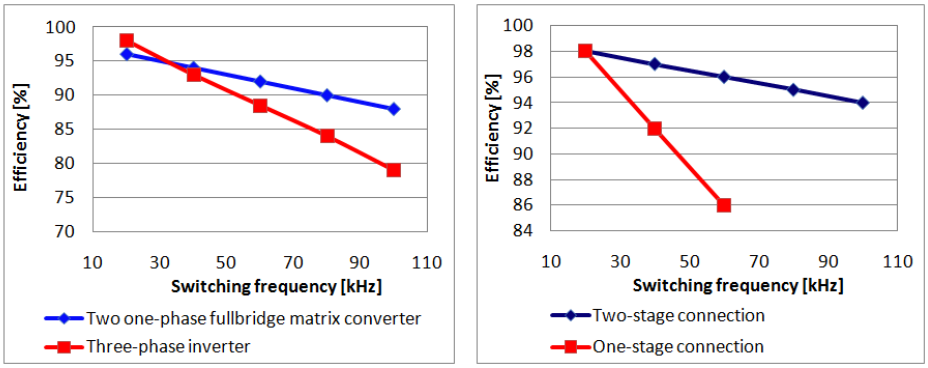

Fig. 9. Comparison of matrix half-bridge converters and 3-phase VSI (a) and two- and single stage converters (b) .

3. Feeding of 2-Phase PMSM by 2-Stage PEC

Simulation Results

The simulation was done using two-phase synchronous motor with PM (SMPM) supplied into two-phase. Parameters of the disk PM synchronous motor:

R_S = 3.93 [Ω], L_d = 43 [mH], L_q = 62.3 [mH] p = 6, J = 50.10^{-3} [kg.m^2], ψ_{PM} = 0.828 [Wb], T_N = 10 [Nm], ω_d = 38 [rad.s^{-1}].

Dynamic model of SMPM for simulation analysis was taken from [9], Fig. 10c. Results of simulation experiments in Matlab-Simulink environment are given in following Figs. 10a,b.

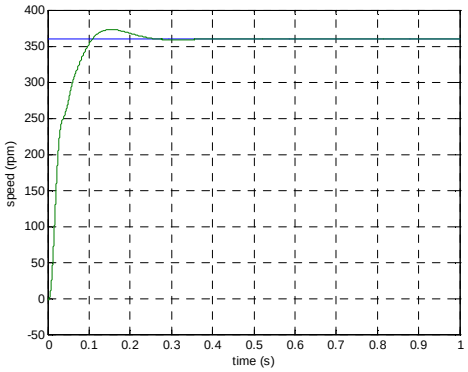

Fig. 11. Simulated start-up of the PMSM up to nominal speed: real (green line) and demanded (blue line)

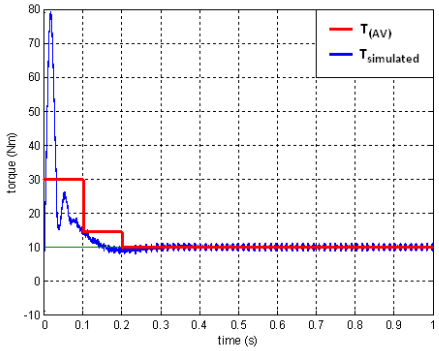

Fig. 12. Instant waveform of SMPM real (blue line) and demanded (green line) torque

Simulation diagram of PM synchronous motor under 2-phase supply with bipolar PWM modulation is depicted in Fig. 11 (next page).

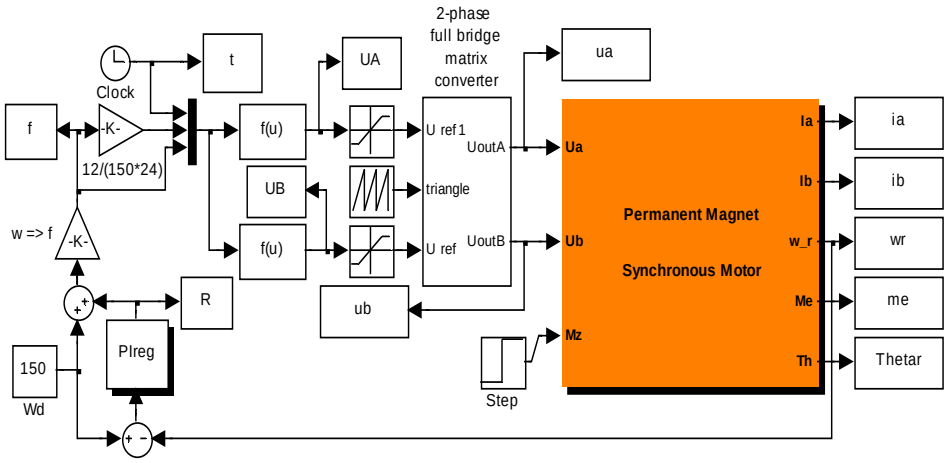

Fig. 11. Simulation diagram of PM synchronous motor controlled 2-phase supply

Single *V/f* = const.- control was used during simulation with speed control and sinusoidal PWM modulation. It's supposed that field/oriented control and SVM modulation will be used in application.

4. Conclusion

As mentioned the AC link version of propulsion electronic system (see Figs. 6,7,8) need not smoothing filter (input capacitor); due to soft switching of both converters. The configuration features a better efficiency of the converters (depending on switching frequency [3]) and also good torque-speed characteristics of two-phase AC motor [9]. Its output voltage values are not restricted. Another connection schemes of 2-phase drive have been chosen for industrial-, home- and residential application (Fig. 9a,b). Regarding to output voltage of the both conceptions it's the same. Simulation results confirm their good properties, and they are in accordance with supposed waveforms and functions.

Appendix

Based on Fig. 5d (Chap. 2) and Fig. A the design equations are:

Conduction of Q1: duty cycle: $t_{Q1}/\Delta T \quad \in <0;0.5>$
Conduction of Q2 duty ratio: $1- t_{Q1}/\Delta T$

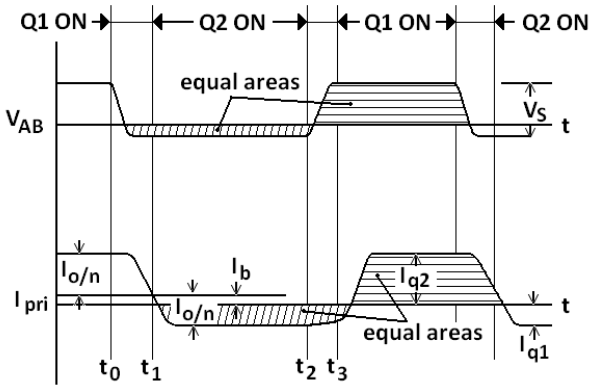

Fig. 12. Half-bridge asymmetric controlled converter waveforms [7]

Transformer voltage balance: $U_{C1} + U_{C2} = U_{DC}$

$$U_{C1} = U_{DC}.(t_{Q1}/\Delta T)$$
$$U_{C2} = U_{DC}.(1 - t_{Q1}/\Delta T)$$

Output voltage balance: $U_0.N = U_{C1}.(t_{Q1}/\Delta T) + U_{C2}.(1 - t_{Q1}/\Delta T)$

Current equations: $I_{Q1}.(t_{Q1}/\Delta T) = I_{Q2}.(1 - t_{Q1}/\Delta T)$

$$I_0.N = (I_{Q1} + I_{Q2})/2 = I_{Q1} - I_{LB} = I_{Q2} + I_{LB}$$
$$I_{LB} = (I_{Q1} - I_{Q2})/2$$

Current RMS values of Q1 and Q2 in time interval of ΔT:

$$I_{Q1RMS} = I_{Q1}\sqrt{(t_{Q1}/\Delta T)}$$
$$I_{Q2RMS} = I_{Q2}\sqrt{(1 - t_{Q1}/\Delta T)}$$

where I_0 is average value of current in each switching interval on the output side.

Acknowledgement

The authors wish to thank for the financial support to R&D operational program Centre of excellence of power electronics systems and materials for their components No. OPVaV-2008/2.1/01-SORO, ITMS 26220120046 funded by European regional development fund (ERDF) and VEGA Agency for the project No. 1/0470/09.

References

[1] EHSANI, M., GAO Y., EMADI, A. *Modern Electric, Hybrid- and Fuel Cell Vehicles.* CRC Press, Boca Raton, USA, 2010.

[2] KASSA, J.. *Connection Choosing of Two/Stage Converter for 2-Phase Drive Application from the Point of View of Efficiency Parameter Increasing*. Written part of PhD exam, Department Mechatronics and Electronics, Zilina (SK), 2011.

[3] DOBRUCKY, B., *et al*. *Two-Phase Power Electronic Drive with Split - Single- Phase Induction Motor*. Proc. of IECON'10 Conf., 2010, IEEE-IES, Phoenix (AZ, USA), pp. CD-ROM.

[4] GONTHIER, L., *et al*. *High-Efficiency Soft-Commutated DC/AC/AC Converter for Electric Vehicles*. Electro-Motion, Vol. 5 (1998), No. 2, pp. 54 – 64.

[5] MHANGO, L.M.C., CREIGHTON, G.K. *Novel Two-Phase Inverter-Fed Induction-Motor Drive*. IEE Proceedings, Vol. 131 (1984), No. 3, pp. 99-104.

[6] BLAABJERG, F., *et al*. *Evaluation of Low-Cost Topologies for Two-Phase IM Drives in Industrial Application*. Record of 37th IEEE IAS Annual Meeting on Industry Application, Vol. 4 (2002), pp. 2358-2365.

[7] DE DONCKER R.W., LYONS J.P. *The Auxiliary Resonant Commutated Pole Converter*. Proc. of IEEE Conference, 1990, pp. 1228-1235

[8] IMBERTSON, P., MOHAN, N. *Asymmetrical Duty Cycle Permits Zero Switching Loss in PWM Circuits with No Conduction Loss Penalty*. IEEE Transactions on Industry Applications, Vol. 29, No. 1, Jan/Feb 1993, pp.

[9] SEKERAK, P., HRABOVCOVA, V., RAFAJDUS, P., KALAMEN, L. *Interior Permanent Magnet Synchronous Motor Parameters Identification*. Proc. of ISEM Conf. on Electric Machines, Prague (CZ), Sep. 2010, pp.107-116

[10] ZASKALICKY, P., ZASKALICKA, M. *Behaviour of the Two-phase Permanent Magnet Synchronous Motor Supplied by Rectangular Voltage.* Acta Technica CSAV 50 (2005), pp. 195-206.

[11] Dobrucký B., Špánik P.: Modelovanie a simulácia výkonových polovodičových štruktúr (1999), s. 4.1-4.6.

[12] *SEMIKRON SKM50GB123D.* Zdroj: website (http://www.alldatasheet.com/ datasheet-pdf/pdf/217665/SEMIKRON/SKM50GB123D.html)

Transcom 2011, 27-29 June 2011
University of Žilina, Žilina, Slovak Republic

Two-dimensional model of induction heating of 60E1 rail

[*]Kamil Kiraga, [*]Elżbieta Szychta,
[*] Technical University of Radom, Faculty of Transport and Electrical Engineering, 26-600 Radom, Malczewskiego 29, Poland, {k.kiraga, e.szychta}@pr.radom.pl

Abstract. A two-dimensional model of a rail (60E1) executed in FEMM software is presented in the article. The model allows for complex calculations of distribution of magnetic induction and magnetic field intensity both in the rail itself and in its environment, which is necessary for designing of an effective heating system for rail turnouts.

Keywords: induction heating, magnetic induction, magnetic field, FEMM.

1. Introduction

Railway rails are fundamental design elements of a turnout beside switch points, sliding chairs or switching closure assemblies. Rails are principally designed to set the proper travel direction of rolling stock wheel sets. The shape of a rail comprises the so-called head (the part along which rolling stock wheels move), web (centre), and foot (the part supporting the whole and carrying the load on to sleepers) [4, 2].

Two main rail types are used on routes administered by Polish State Railways PKP PLK: 49E1 and 60E1. Rail 49E1 are used on routes with light rolling stock load whereas. Rail 60E1 are used on heavily loaded routes where speeds reach over 100 km/h [6].

As part of research into development of a method of turnout induction heating, the following elements must be emphasised in particular:

- structure of rail material, its resistivity and magnetic permeability,
- skin effects and penetration depth of the magnetic field into the rail structure,
- value of active power arising in the zone of magnetic interactions with the rail.

These parameters depend, inter alia, on magnetising current frequency and are not clearly defined by rail manufacturers (rails may come from different charges, may be produced by means of diverse rolling, straightening, and hardening technologies), and require experimental determination of their value, e.g. as part of computer simulation or laboratory testing [1, 3].

The authors propose a structural (2D) rail model in order to determine the above parameters and to follow the entire process of turnout induction heating. The model helps to analyse magnetic and electric effects of magnetic field on a rail.

2. Two-dimensional model of 60E1 rail

Normalised dimensions of the normal-gauge 60E1 rail [5] are presented in Figure 1. Based on these dimensions, a two-dimensional rail model was generated for purposes of simulation testing in FEMM software (by means of MES – finite elements method).

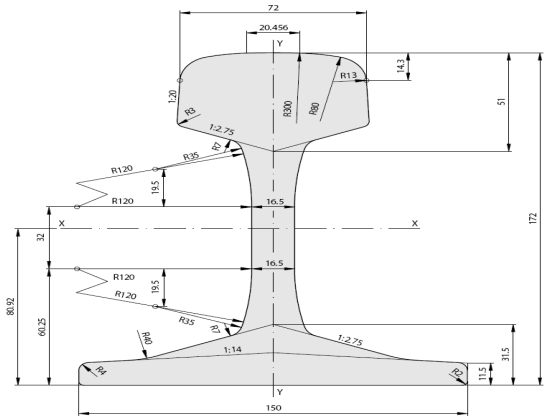

Fig. 1. Geometrical dimensions of the normal-gauge 60E1 rail [5].

Figure 2 illustrates a rail model considering the geometrical dimensions in Fig. 1 as executed in FEMM. This model considers the varied internal structure of a rail arising in the engineering process and its fundamental electric and magnetic parameters, determined by means of laboratory testing.

Fig.2. A simulation model of 60E1 (MES) rail in FEMM.

The essential electric and magnetic parameters of a rail which can be employed to simulate induction heating of 60E1 rail in both two and three-dimensional space include:

- electrical resistivity $\boldsymbol{\rho}$,
- magnetising prime curve $\boldsymbol{B}$ = f($\boldsymbol{H}$), maximum rail permeability $\boldsymbol{\mu_{max}}$ as dependent on magnetic field variations $\boldsymbol{H}$ and initial permeability $\boldsymbol{\mu_{pocz}}$ across a broad range of frequency variations $\boldsymbol{f}$,
- intensity of the coercive force $\boldsymbol{H_c}$,
- magnetising curve $\boldsymbol{J}$ = f ($\boldsymbol{H}$) and saturation $\boldsymbol{J_s}$,
- loss factors of eddy currents $\boldsymbol{w}$ and of magnetic hysteresis loop $\boldsymbol{h}$.

3. Properties of induction heating of 60E1 rail in the two-dimensional model in FEMM environment

The following assumptions underpin simulation testing of an 60E1 rail at the time of induction heating in 2D space:

- density of the current across the heating wire is constant,
- magnetic field is described by means of magnetic vector potential,
- electric and magnetic parameters employed in simulation calculations:
  - electrical resistivity $\boldsymbol{\rho}$,
  - magnetising prime curve $\boldsymbol{B} = f(\boldsymbol{H})$ maximum rail permeability $\boldsymbol{\mu_{max}}$ as dependent on magnetic field variations $\boldsymbol{H}$ and initial permeability $\boldsymbol{\mu_{pocz}}$ across a broad range of frequency variations $\boldsymbol{f}$,
- zero boundary conditions (setting of a vector potential equal to 0 along a selected boundary).

A series of simulations were conducted on the basis of the above assumptions to find an optimum placement of a heating wire inside the rail, comparing values of magnetic field intensity $\boldsymbol{H}$ generated along the edge of the rail where the wire was placed. Various methods of placing the wire are shown in Figure 3. The results presented in this article were obtained in simulations of induction heating by means of rotational currents at a frequency of 650 Hz.

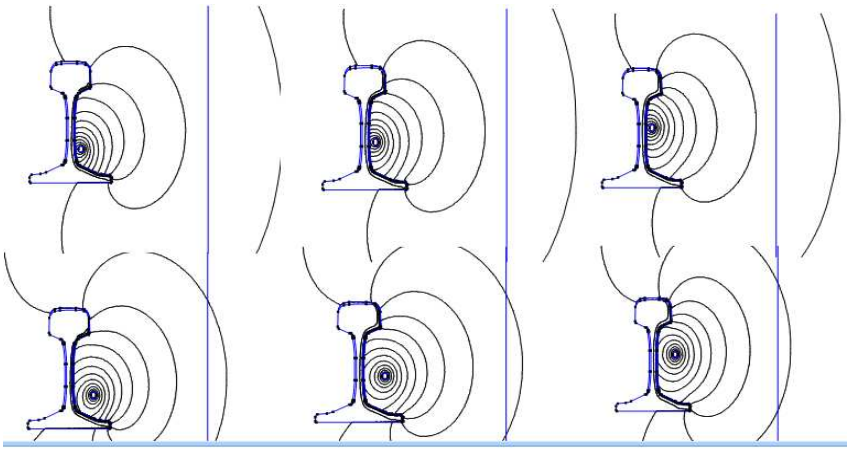

Fig.3. Varying placements of the heating wire inside the rail.

Position of the heating wire obtained in 2D simulations is optimum where the wire is placed near the edge of the rail web. Distribution of magnetic field intensity $\boldsymbol{H}$ in the rail and its environment for the optimum placement of the heating wire are illustrated in Figure 4.

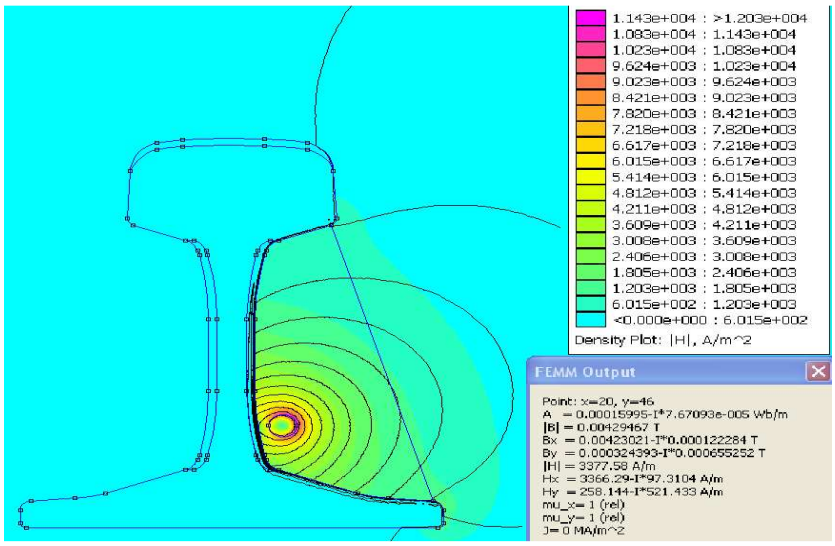

Fig.4. Distribution of magnetic field intensity $\boldsymbol{H}$ for the optimum placement of the heating wire.

Figure 5 shows distribution of magnetic induction intensity ***B*** generated on the lateral surface of the rail web with the optimum placement of the heating wire.

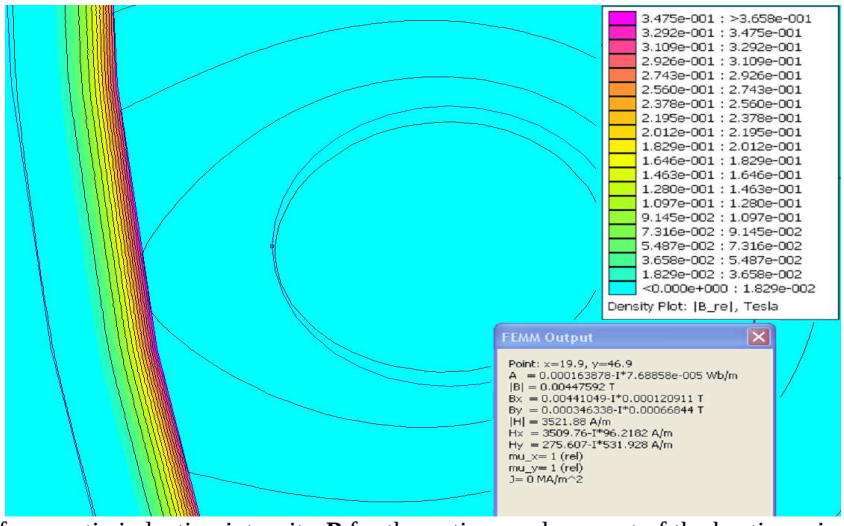

Fig.5. Distribution of magnetic induction intensity ***B*** for the optimum placement of the heating wire.

Distribution of rotational currents intensity induced inside the rail web and depth of their penetration are shown in Figure 6.

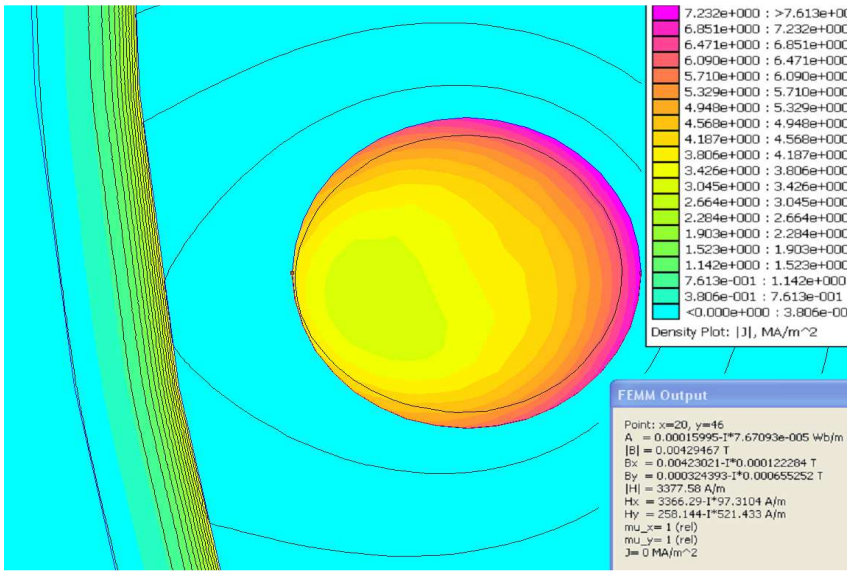

Fig.6. Eddy currents inside the rail web for the optimum placement of the heating wire.

4. Conclusion

An accurate knowledge and interpretation of electric, magnetic, and thermal effects in the internal structure of a rail are necessary to develop an effective method of induction heating for turnouts (that would efficiently melt snow and ice from key parts of turnouts). A model representing the internal structure of a rail, with all its electrical and magnetic properties, is useful and necessary to this purpose. The 2D model discussed in the article and simulation results of the induction heating need to be verified in operational testing of actual induction heating systems in order to eliminate possible errors due to development of certain simulation assumptions. Efficiency, functionality, and safety of the new method will be verified in comparative testing of electric and magnetic turnout induction heating in a climatic chamber.

References

[1] BRODOWSKI D., ANDRULONIS J.: Effectiveness of heating crossover railway system, CNTK Warsaw 2000.

[2] GROBELNY M.: Building, Modernisation, Repairs, and Maintenance of Railway Surfaces – Equipment and Elements RYNEK KOLEJOWY, 2009-03-09.

[3] KIRAGA K., SZYCHTA E., ANDRULONIS J.: *Chosen methods heating crossover railway system – inspection article,* PRZEGLĄD ELEKTROTECHNICZNY, ISSN 0033-2097, R. 86 NR 2/2010.

[4] rail website: www. inzynieria-kolejowa.dl.pl.

[5] *The technical conditions of maintaining railway track surface*, PKP POLSKIE LINIE KOLEJOWE S.A., Warsaw 2005.

[6] WIELGOSZ R.: *Connecting Continuous Rails,* MECHANIKA CZASOPISMO TECHNICZNE, Technical University of Cracow, 2-M/2009, Notebook (6), Year 106.

Transcom 2011, 27-29 June 2011
University of Žilina, Žilina, Slovak Republic

Undervoltage Wave Propagation Speed on Three Phase Scale Model of 22 kV Power Line

[*]Miroslav Kováč
[*]University of Žilina, Faculty of Electrical Engineering, Department of Power Electrical Systems, Univerzitná 1, 01026 Žilina, Slovakia, miroslav.kovac@kves.uniza.sk

Abstract. The paper describes theoretical analysis of electromagnetic wave propagation speed on power line and provides expression for propagation speed calculation using RLCG parameters. Propagation speed's value is important input for fault location algorithm based on undervoltage wave detection. Measured RLC parameters of three phase scale model of power line were used to calculate the value of propagation speed. This value was then compared with experimental results obtained from model.

Keywords: electromagnetic wave, propagation speed, phase constant, scale model, three phase power line

1. Introduction

In order to perform fault location in medium voltage networks a method using undervoltage wave detection was developed [1]. Its accuracy depends on the most exact knowledge of wave propagation speed and time when undervoltage wave arrives to particular measuring point.

2. Analytical approach to wave propagation speed determination

2.1. Basic expression of propagation speed

There are basically two possibilities of wave propagation speed evaluation. The first is theoretical analysis leading to calculated result and the second is measurement on real system or physical model. Theoretical analysis is based on the two facts – voltage on the power line is in the form of wave with length given by RLCG parameters and applied voltage waveform changes its value in time at angular speed given by its frequency.

Angular distance φ in radians travelled by the complex vector of harmonic voltage is given as:

$$\varphi = \omega \cdot t \,, \tag{1}$$

where ω (rad.s^{-1}) is angular frequency, t (s) is time. Physical distance s (m) is defined as:

$$s = v \cdot t \,, \tag{2}$$

where v (m.s^{-1}) is translation speed. Solving differential equations for electromagnetic wave propagation defines phase constant α (rad.km^{-1}) [2] as:

$$\alpha = \frac{\varphi}{s} \,. \tag{3}$$

Substituting expressions (1) and (2) into (3) gives expression for electromagnetic wave propagation speed

$$v = \frac{\omega}{\alpha} \,. \tag{4}$$

This operation means in fact converting angular distance into physical distance, in other words converting angular speed into physical speed.

2.2. Propagation speed expressed by RLCG parameters

Phase constant α is defined as imaginary part of the expression for propagation constant γ defined as [2]

$$\gamma = \beta + j\alpha = \sqrt{(R + j\omega L)(G + j\omega C)}. \tag{5}$$

Squaring equation (5) and separating real and imaginary part we get

$$\beta^2 = \alpha^2 + RG - \omega^2 LC, \tag{6}$$

$$4\beta^2\alpha^2 = (\omega RC + \omega LG)^2. \tag{7}$$

Then we substitute equation (6) into (7) and modify resulting expression into the quadratic equation form

$$4\alpha^4 + 4\alpha^2(RG - \omega^2 LC) - (\omega RC + \omega LG)^2 = 0. \tag{8}$$

Expression (8) is quadratic equation with unknown α^2. Using well-known formula for roots extraction we get

$$\alpha^2 = \frac{-4(RG - \omega^2 LC) \pm \sqrt{16(RG - \omega^2 LC)^2 + 16(\omega RC + \omega LG)^2}}{8}. \tag{9}$$

It will be shown later that only plus sign in equation (9) has physical sense. After square rooting equation (9) and its modification, we get final expression of phase constant through RLC parameters

$$\alpha = \frac{1}{\sqrt{2}} \cdot \sqrt{\omega^2 LC - RG + \sqrt{(RG - \omega^2 LC)^2 + (\omega RC + \omega LG)^2}}. \tag{10}$$

Because phase constant has always positive value only positive square root of equation (9) is considered as well.

If we consider lossless power line then series resistance and leak conductance could be neglected and we can rewrite equation (9) with minus sign in numerator as follows

$$\alpha = \frac{1}{\sqrt{2}} \cdot \sqrt{\omega^2 LC - \omega^2 LC}. \tag{11}$$

Expression (11) means that phase constant would have zero value, what is impossible, because the speed of light in vacuum is limited as well as wave propagation speed on lossless line. However considering plus sign in equation (9) or using equation (10) we get phase constant for lossless line

$$\alpha = \omega\sqrt{LC}. \tag{12}$$

And finally substituting equation (10) into equation (4) we get electromagnetic wave propagation speed v (m.s^{-1}) expressed in terms of specific RLCG parameters

$$v = \frac{\omega\sqrt{2}}{\sqrt{\omega^2 LC - RG + \sqrt{(RG - \omega^2 LC)^2 + (\omega RC + \omega LG)^2}}}. \tag{13}$$

3. Description of scale model of three phase power line

Scale model of three phase power line is physical model developed in order to represent tree structure of medium voltage distribution network in laboratory environment [3]. Electrical parameters of the model are derived from power line with conductors placed on flat console on

concrete pillar with distance between phases 1.44 m and average height 10 m above ground, conductor type AlFe 95/15 was chosen.

	R ($\Omega.km^{-1}$)	L ($mH.km^{-1}$)	C ($nF.km^{-1}$)
Calculated	0,36	1,17	10,34
Measured	0,35	0,97	11,69

Tab. 1. Values of the model's specific RLC parameters.

After modules of the model were manufactured, measurement of specific RLC parameters were done, because they might differ from calculated values. Both results are shown in Tab. 1. The biggest difference is in the values of inductance because of coil construction complexity.

4. Wave propagation speed evaluation

4.1. Calculation using theoretical expression

Substituting measured specific RLC parameters into expression (13) we calculate values of wave propagation speed. It is suitable to express propagation speed as percentage value of light speed v_R, because values in kilometers or meters per second are very high and impractical to read.

Wave propagation speed on lossless power line is usually higher than 99% of light speed, for real line the speed decreases almost linearly according to expression (13) (Fig. 1).

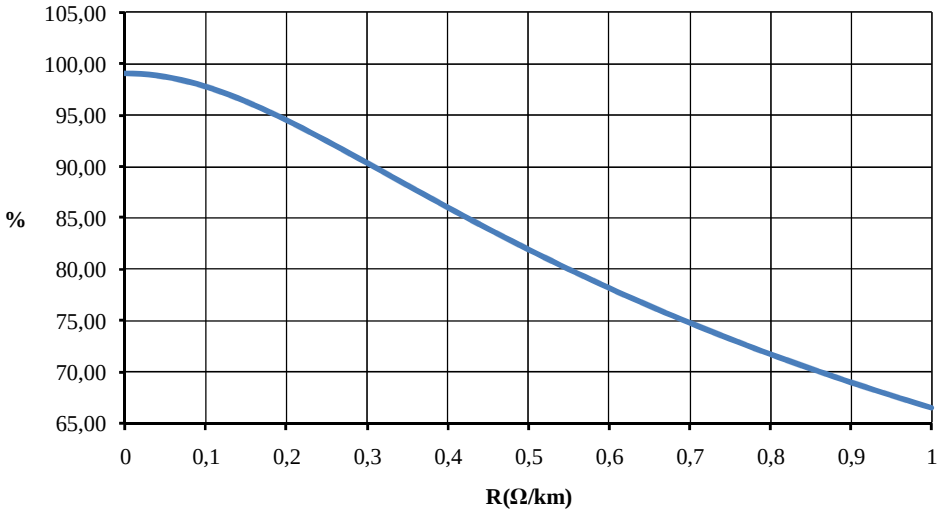

Fig. 1. Wave propagation speed v_R in terms of line's specific resistance.

4.2. Experimental evaluation

In order to experimentally evaluate wave propagation speed on scale model a line consisting of six modules was set up. According to measurements of RLC parameters of built modules [3] and comparison with specific values of the line with conductor AlFe 95/15, the series connection of six modules represented 27.61 km of the real line.

Single phase to ground fault at the end of the line was simulated using remote controlled electromagnetic switch. There were two measuring points, each of them was connected to separate oscilloscope channel and time delay between voltage drops was measured. Red (darker in black and white) waveform is measured at the beginning of the line and the green (lighter) waveform in location of the fault.

Substituting modeled length of the line and time difference detected by the oscilloscope (Fig. 2) into expression (2) we get the value of wave propagation speed on the scale model. Several measurements were made and results are shown in Tab. 2.

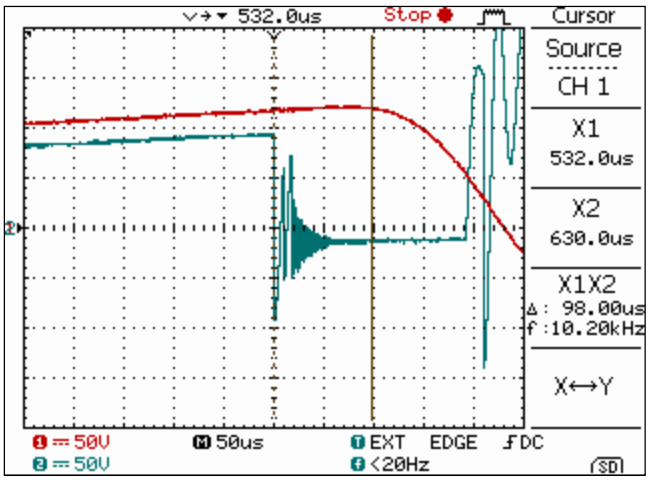

Fig. 2. Time difference between voltage drops.

	Δt (s)	v (km.s^{-1})	v_R (%)
Calculated		264407,68	88,20
Measured	98µs	281734,69	93,98

Tab. 2. Values of calculated and measured wave propagation speed.

5. Conclusion

Obtained experimental results show that real parameters of power line or a model may differ more or less from calculated values. Even though theoretical analysis is correct its results strongly depends on primary RLC parameters accuracy. In order to perform fault location is more appropriate to evaluate propagation speed for particular system by measuring time difference at specified points along power line to calibrate fault locating devices. This could be made for example by forced breaker manipulation or after first real fault occurrence.

Acknowledgement

This work was supported by the Slovak Research and Development Agency under the contract No. APVV-0560-07.

References

[1] HÖGER, M., BRACINÍK, P., ALTUS, J., OTČENÁŠOVÁ, A. *Fault location in medium voltage networks by the help of adapted triangulation principle*. Innovative Smart Grid Technologies Conference Europe (ISGT Europe), 2010 IEEE PES , pp.1-5, 11-13 Oct. 2010

[2] KOLCUN, M. a kol. *Analýza Elektrizačnej Sústavy*, TU Košice, 2005, 419 s., ISBN 80-89057-09-8

[3] KOVÁČ, M., BRACINÍK, P. *Realizácia trojfázového modelu úseku vedenia 22 kV*, Časopis pre elektrotechniku a energetiku EE, ročník 16. číslo 1, 2010, str.: 36 - 39, ISSN 1335-2547

Transcom 2011, 27-29 June 2011
University of Žilina, Žilina, Slovak Republic

Correction Method of Processing Characteristics of the Measuring Transducer

[*]Mirosław Luft, [*]Elżbieta Szychta, [*]Radosław Cioć, [*]Daniel Pietruszczak
[*]Kazimierz Pułaski Technical University of Radom, Faculty of Transport and Electrical Engineering, Malczewskiego 29, 26-600 Radom, Poland, {m.luft, e.szychta, r.cioc, d.pietruszczak}@pr.radom.pl

Abstract. The paper presents a method of correcting the processing characteristics of the measuring transducer by using a software equalizer described the integral-differential calculus (fractional orders). The characteristics of the transducer response correction and without correction are compared.

Keywords: measuring transducer, fractional calculus, ARX method.

1. Introduction

While describing dynamic characteristics of measuring transducers, usually in the form of classical differential equations, it is necessary to consider all kinds of occurring elements as well as relationships among them [4], [5], [8], [10]. Most frequently the measuring transducer is presented as a device measuring an input signal and processing it into an output signal [10]. It is a simplified assumption because in reality many input signals affect the transducer. They can be either the measuring signals or disturbances. A source of disturbances can be the transducer itself due to its processing characteristics or external factors. Disturbance signals are processed by the transducer and thus they affect the reproduction of the measured quantity. The concept of signal processing by the measuring transducer is shown in Figure 1.

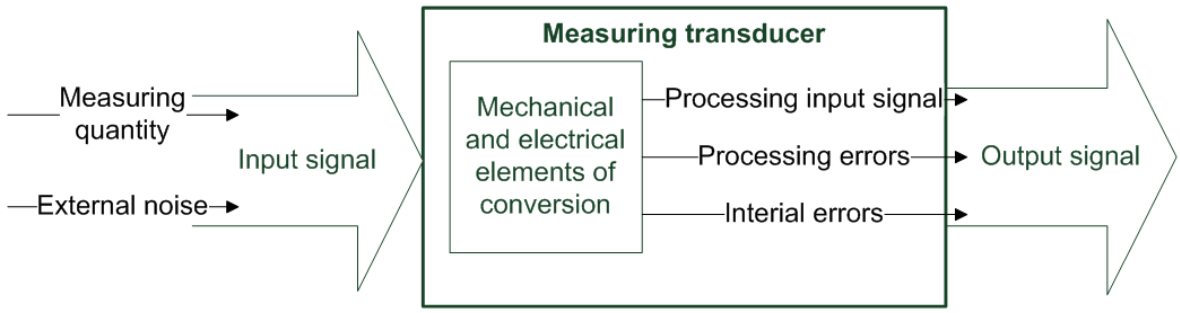

Fig. 1. The process of signal processing by the measuring transducer.

Correction of the processing characteristics of the measuring transducer is to provide conformity between the characteristics of the measured quantity waveform and its reproduction by the transducer as a result of introducing a correction element into the measurement chain [6], [8], [9], [10].

2. Correction method of the measuring transducer characteristics

The study of fractional calculus reveals that in some applications it describes the object dynamics more accurately than classical differential equations [1], [14]. The enhanced computational power of a computer allows its practical application. In our study we attempted to use this calculus to correct processing characteristics of the measuring transducer model described by a second order differential equation. A derivative and an integral of arbitrary order open unimaginable possibilities in the field of dynamic system identification, and creation of new, earlier inaccessible, algorithms of feedback system control. Orders can also be considered as time functions. This also leads to differential equations of variable, time dependent orders [3], [4], [11], [13].

The accelerometer model is described by a differential equation:

$$\ddot{w}(t) + 2\zeta\omega_0\dot{w}(t) + \omega_0^2 w(t) = -\ddot{x}(t)\,. \tag{1}$$

where: ω_0 – natural angular frequency, ζ – damping.

Equation (1) – after some suitable parameters for the transducer have been applied, can be presented in the form of operational transmittance:

$$G(s) = \frac{-s^2}{s^2 + 51s + 255}\,. \tag{2}$$

Transducer model (2) is treated as a real measuring transducer model. Most often it is not known. For this reason, in order to identify a description of its dynamics it is necessary to use an identification method. In this particular case the ARX (AutoRegressive with eXogenious input identification method) method was applied [6], [7], [10].

While examining the response of the transducer model (2) to the sinusoidal input waveform with the use of the ARX method, the record of its dynamics is obtained in the form of discrete transmittance:

$$G(z) = \frac{-0.9937z^2 + 1.002z - 0.0062}{z^2 - 0.9795z + 0.0025}\,. \tag{3}$$

The ultimate record of the transducer dynamics in the fractional calculus form looks as follows:

$$G(z) = \frac{-z^2 + 1.0205z + 0.0231}{-0.9937z^2 + 0.9864z + 0.0021}\,. \tag{4}$$

The responses of the transducer (2) transmittance and the transmittance determined by the fractional calculus method (4) were compared. Simulation tests were carried out in the MATLAB-SIMULINK package [8]. Figure 2 presents the block diagram of the system.

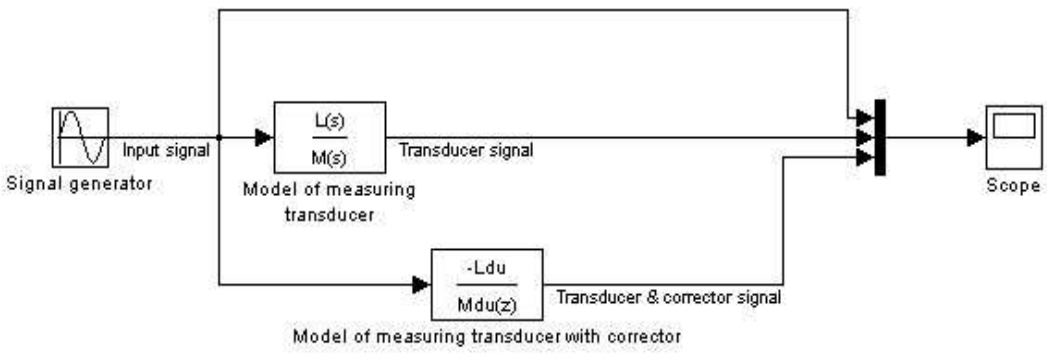

Fig. 2. Block diagram of the measurement system for the measuring transducer.

Figure 3 compares responses to the input signal of the transducer described by equation (2) and derivative-integral transmittance (4).

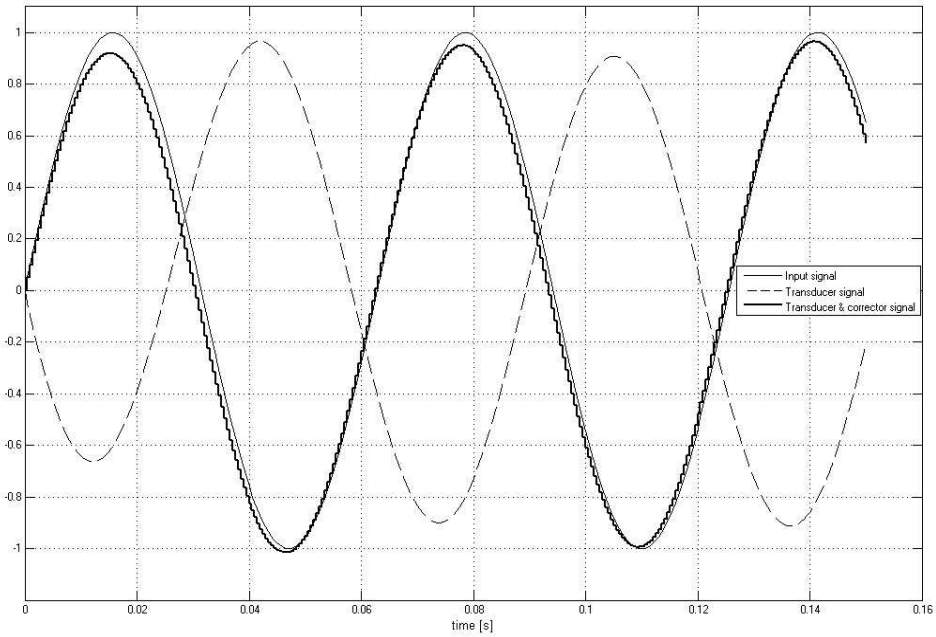

Fig. 3. Comparison of responses of the measuring transducer models.

Transmittance (4) brings its response to the input signal closer in relation to transducer (2). For this reason it is treated as a notation of its dynamics together with the correction improving its dynamic responses. The waveforms shown in Figure 3 allow us to infer that the application of the derivative-integral method reduced the time lag of the transducer model (2) response and removed the errors from the input signal amplitude processing caused by its transient state at the beginning of its operation. A similar effect is obtained when the input signal transducer we add Gaussian noise. Figure 4 depicts responses of all models of the measuring transducer to the sinusoidal input signal with Gaussian noise

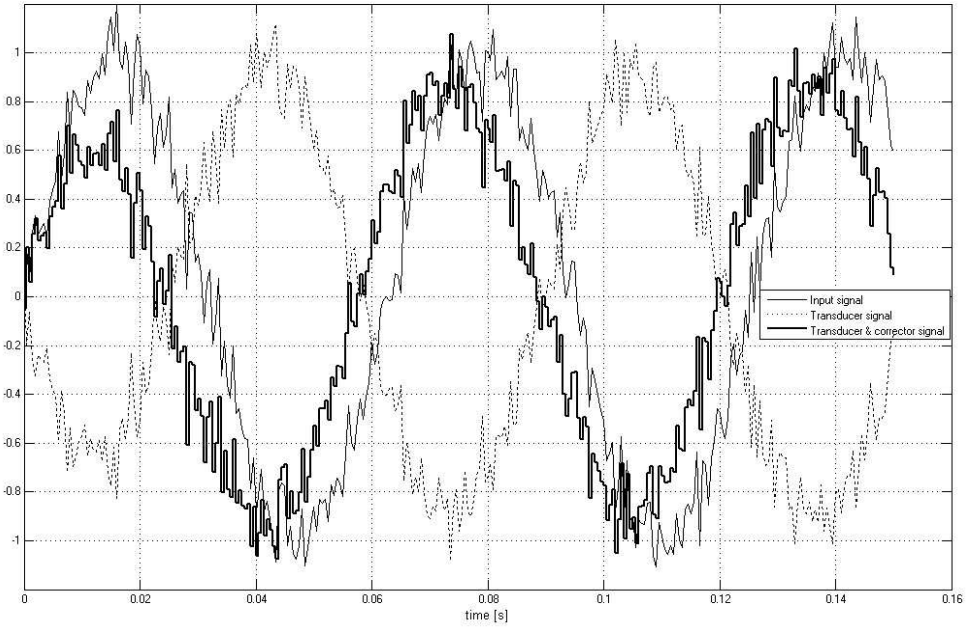

Fig. 4. Comparison of responses of the measuring transducer models with Gaussian noise.

3. Conclusion

Application of fractional calculus in modelling measuring transducers allows a more accurate reproduction of their model dynamics in comparison to classical differential equations. When combined with the ARX identification model it is possible to obtain notations of the measuring transducer model dynamics taking into account and reducing errors resulting from processing the input quantity into the output quantity.

The method outlined refers to simulation tests. In order to use it in real measurement systems it is necessary to establish a method of obtaining equations describing dynamics of the correction itself.

References

[1] KACZOREK, T.: *Wybrane zagadnienia teorii układów niecałkowitego rzędu*, Oficyna Wydawnicza Politechniki Białostockiej, ISSN 0867-096X, Białystok 2009. (in Polish)

[2] LUFT, M., CIOĆ, R., PIETRUSZCZAK, D.: *Porównanie klasycznego i różniczkowo-całkowego modelu systemu pomiarowego*, LogiTrans 2011, Szczyrk 2011. in press, (in Polish)

[3] LUFT, M., CIOĆ, R., PIETRUSZCZAK, D.: *Fractional calculus in modelling of measuring transducers*, ELECTRONICS'2011, Kaunas and Vilnius, Lithuania, 17 -19.05.2011. in press

[4] LUFT, M., CIOĆ, R., PIETRUSZCZAK, D.: *Porównanie klasycznego i różniczkowo-całkowego modelu przetwornika pomiarowego*, Logistyka nr 6/2010. (in Polish)

[5] LUFT, M., CIOĆ, R., PIETRUSZCZAK, D.: *Measurement transducer modelled by means of classical integer-order differential equation and fractional calculus*, Proceedings of the 8th International Conference ELEKTRO 2010, pp TA5_88-TA5_91, ISBN 978-80-554-0196-6, Slovak Republic, Zilina 2010. in press

[6] LUFT, M., CIOĆ, R., PIETRUSZCZAK, D.: *Correction of measuring track processing errors in vibration measurements of coal wagon*, Proceedings of the 4th International Conference on Electrical and Control Technologies, Kaunas University of Technology, Lithuania, pp 87-92, ISSN 1822-5934, Kaunas 2009.

[7] LUFT, M., CIOĆ, R., PIETRUSZCZAK, D.: *Increasing the accuracy of non-linear measuring transducers processing*, Advances in Transport Systems Telematics, pp 189-196, (ISBN 978-83-206-1715-3), WKŁ, Warszawa 2008.

[8] LUFT, M., KRZYSZTOSZEK, K., CIOĆ, R., PIETRUSZCZAK, D.: *Analiza właściwości i synteza przetworników z dynamiczną korekcją błędów – dla badania i diagnostyki środków transportu*, Praca naukowo-badawcza PRad, nr tematu: 2268/47/P, Radom 2005-2007. (in Polish)

[9] LUFT, M., PIETRUSZCZAK, D., OLSZOWIEC, P.: *Correction of transducers dynamic characteristics in vibration research of railway coal wagon Faals type*, Proceedings of the III International Interdisciplinary Technical Conference of Young Scientists IntertTech 2010, pp 221-225, (ISBN 978-83-926896-2-1), Poznań 2010.

[10] LUFT, M., PNIEWSKI, R., CIOĆ, R., PIETRUSZCZAK, D.: *Sprzętowy układ korekcji błędów dynamicznych przetworników pomiarowych w zastosowaniu do badań i diagnostyki środków transportu*, Praca badawcza, nr tematu: 2651/47/P, Radom 2008-2009. (in Polish)

[11] LUFT, M., SZYCHTA, E., CIOĆ, R., PIETRUSZCZAK, D.: *Application of fractional calculus in identification of the measuring system*, Gdynia 2011, TransNav 2011. in press.

[12] LUFT, M., SZYCHTA, E., CIOĆ, R., PIETRUSZCZAK, D.: *Application of fractional calculus in modelling of the transducer and the measurement* system, Przegląd Elektrotechniczny, Warszawa 2011. in press.

[13] LUFT, M., SZYCHTA, E., CIOĆ, R., PIETRUSZCZAK, D.: *Measuring transducer modelled by means of fractional calculus*, Communications in Computer and Information Science 104, pp.286-295, ISBN 978-3-642-16471-2, Springer-Verlag Berlin Heidelberg, 2010.

[14] OSTALCZYK, P.: *Zarys rachunku różniczkowo-całkowego ułamkowych rzędów. Teoria i zastosowanie w automatyce*, Wydawnictwo Politechniki Łódzkiej, ISBN 978-83-7283-245-0, Łódź 2008. (in Polish)

Transcom 2011, 27-29 June 2011
University of Žilina, Žilina, Slovak Republic

Magnetic Probes Used in Eddy Current Testing

[*]Viera Maťková
[*]University of Žilina, Faculty of Electrical Engineering, Department of Electromagnetic and Biomedical Engineering, Univerzitná 1, 01026 Žilina, Slovakia, matkova.viera@fel.uniza.sk

Abstract. This paper deals with evaluation of conductive materials by electromagnetic non-destructive testing (eNDT) with emphasize on eddy current testing (ECT). Also it describes probes for eddy current sensing mainly by means of magnetic sensors e.g. giant magneto-resistance (GMR) and spin dependent tunneling (SDT). These sensors are characterized by frequency range, sensitivity, relatively low cost, small size and low power consumption.

Keywords: Eddy current testing, probe, magnetic sensors, GMR sensors, SDT sensors

1. Introduction

Nowadays are very important quality, reliability and security therefore nondestructive testing of materials is very important not only in industry but also in transport and medicine. Various NDT techniques from a wide group use different tools whose base consists in various physical phenomena and they are characterized by different and specific requirements and applications. NDT is used in many areas of the inspection e.g. inspection of metal pipes, in air maintenance, to control prosthetic and implants in medicine, etc.

One of the most popular eNDT methods is eddy current testing (ECT). Eddy current testing is an effective way to detect fatigue and corrosion cracks in conductive materials. The principle of ECT can be described as follows. Eddy current coil is fed by alternating sinusoidal current (AC) of frequencies in the range 50 Hz to 10 MHz. This coil generates primary magnetic field which is in accordance with Ampere's law. This primary magnetic field induces eddy currents in the controlled conductive material object according to the Faraday's law. Then eddy currents generate secondary magnetic field, which has the opposite direction as the primary field, it follows that any significant change in the material (defects) will change the impedance of the coil. The impedance change is measured, analyzed and correlated with defect dimensions. The locations impedance changes obtained during the movement of an eddy current probe coil over material with a defect is called eddy current signal. Its amplitude provides information on defect size and the phase angle with respect to lift-off provides information on the defect location or thickness.

Eddy current density in the material isn't uniform in the material depth direction. It is the largest one on the surface and it decreases monotonously with depth (skin effect) according to the relation of effective depth of penetration which decreases with increasing frequency, permeability and conductivity. It means that ECT is used for measuring thickness of thin surfaces using very high frequencies and on the contrary also for detection of sub-surface buried defects and for testing highly conductive materials by very low frequencies. Usually the driving current is constant (few hundreds of mA) and the impedance changes occurred due to perturbation of eddy currents at defect regions are to be measured. These changes are very small (μΩ) and therefore high precision AC bridge is used.

ECT device usually consists of an oscillator (the excitation frequency) constant AC supply, AC (Maxwell) bridge, amplifier and screen (to display the changes in a 2D graph or as a vector). In modern systems there a computer with the necessary hardware (plug-in card) and software is used

for measurements, adjustment, data storage, analysis and management. One of the most important parts of the ECT device is the sensing part called probe which is crated obviously by probe coils or other sensors.

Because security of critical systems depends on early detection of cracks to prevent major defects, there is an increasing need for eddy current probes that can reliably detect very small defects. Also the increasing demands for probes that can detect deep defects to avoid disassembling structures are discussed. There are also other applications where ECT is used, e.g. material thickness measurements, conductivity measurements for material identification, etc, [1].

2. Enhancing Eddy Current Probes Characteristics

Eddy current testing probes combine an excitation coil that induces eddy currents in a specimen and a detection element that identifies the perturbation of the eddy currents caused by cracks or other defects. The detection elements can be coils, superconducting quantum interference detectors, or solid-state magnetic sensors (e.g., Hall effect, magnetoresistive, and spin-dependent-tunneling sensors).The use of low-field solid-state magnetic sensors represents a significant advance over more traditional inductive probes in use today. Two key attributes will open opportunities for increased use of magnetic sensors for eddy current testing: constant sensitivity over a wide range of frequencies and development of smaller sensors.

Probes that detect eddy current fields using inductive coils have less sensitivity at low frequencies. Unfortunately, this is where the device would have to operate to detect deep flaws. Small sensing coils, which are required to detect small defects, also have low sensitivity. In contrast, small, high-sensitivity thin film sensors can locally measure a magnetic field over an area comparable to the size of the sensor itself (tens of micrometers). A limitation of conventional eddy current probes is the difficulty of detecting small cracks originating at the edges of a specimen. This defect is the most common type encountered in practice. An example is the cracks that appear around the fastener or rivet holes in aircraft multilayered structures. Most inductive coil probes are sensitive to both the edge and the cracks initiating from or near the edge. The edge creates a large signal that obscures the small signal from the crack. GMR and SDT magnetic sensors can be oriented to eliminate the edge signal. With this orientation, the presence of the edge enhances the signal from the crack.

To achieve high resolution for detecting small surface and near-surface defects, it must be reduced the dimensions of the excitation coil. The minimum length of a detectable crack is roughly equal to the mean radius of the coil. Sensor developers have successfully developed and tested probes incorporating small, flat, pancake-type coils or planar excitation coils deposited on the sensor substrate. Developers fabricated the first fully integrated eddy current probes using planar technology to precisely position and align the excitation coil with respect to the sensor. This makes large-quantity, high-reproducible probe production economically viable. The technology makes it possible to produce integrated arrays of eddy current probes for fast inspection and—in some applications—to eliminate the need of mechanically scan the probe during inspection [3].

2.1. GMR and SDT Sensors

Recent development of thin film magnetic technology has resulted in films exhibiting a large change in resistance with magnetic field. This phenomenon is called giant magneto-resistance to distinguish it from conventional anisotropic magneto-resistance (AMR). Whereas AMR resistors exhibit a change of resistance of up to 3%, various GMR materials achieve about a 10 ÷ 20% change in resistance. GMR films have two or more soft magnetic layers of iron, nickel and cobalt alloys separated by a nonmagnetic conductive layer such as copper. The resistance has maximum value when the magnetic moments of the layers are anti-parallel (fig. 1*a*) and minimum when they are parallel (fig. 1*b*).

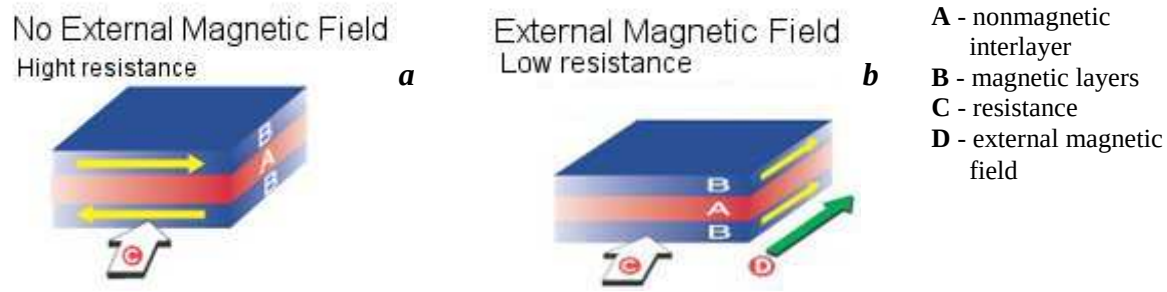

Fig.1. Principle of GMR sensors, [5]

The main components of an eddy current probe for non-destructive testing are pancake-type coil and an AC bridge of GMR or SDT sensors. Arrangement of coil and GMR sensor for eddy current detection of defects in conductors is shown in the fig. 2. When measuring along the sensing axis, it must be kept the GMR probe coplanar with the surface of specimen. The excitation field on the coil axis, being perpendicular to the sensing axis of the GMR, has no effect on the sensor. In this way, the detected field, which is the result of the perturbation of the eddy current flow paths caused by the crack, is separated from the excitation field.

Eddy current induced in the surface of a defect-free specimen are circular because of the circular symmetry of the field produced by the coil [4].

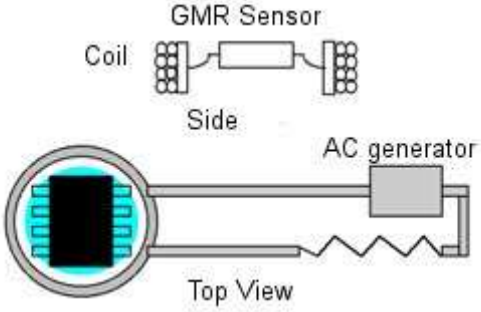

Fig. 2. Setup of ECT with GMR probe

The tangential component of the field created by the eddy currents is zero at the location of the sensor. In presence of defects, the eddy currents are no longer symmetrical and the probe provides a measure of the perturbed eddy currents caused by underlying flaws. The size of the coil is related to the resolution necessary to detect the defects. For large defects and for deep defects, large coils surrounding the sensors are required. Small coils located close to the specimen are necessary to resolve small defects [1].

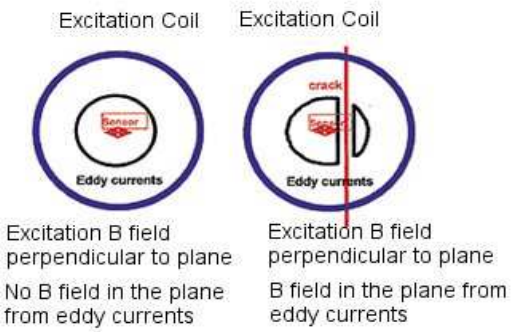

Fig.3. Magnetic fields from the excitation coils create circular eddy currents in the conducting surface below the coils. These eddy currents form along the sensitive axis of the sensor, which is parallel to the conducting surface. A crack or defect alters the eddy current paths, resulting in magnetic fields parallel to the conducting surface and along the sensitive axis of the sensor.

Eddy currents shield the interior of the conducting material with the skin depth related to the conductivity and the frequency. By changing the frequency it is possible to probe differing depths

of the material. GMR sensors with their wide frequency response, from DC to the MHz range, are well suited to this application. The small size of the sensing element increases the resolution of defect location while the detector is raster-scanned over the surface [2].

More rapid scans can be performed using an array of detectors. There were built the optimized EC probe prototypes to detect and map different types of defects encountered in practice. Short surface cracks can also be reliably detected using small excitation coils. The unidirectional sensitivity of GMR sensors enables the detection of cracks perpendicular to the edge of a specimen. This discrimination is possible because the sensitive axis of the sensor can be oriented parallel to the edge. Consequently, the output signal of the sensor is caused only by the crack.

SDT sensors are particularly attractive for nondestructive evaluation, low-frequency applications, such as the detection of deeply buried flaws. In contrast, inductive probes have poor sensitivity at low frequencies because they are sensitive to the time derivative of the magnetic field rather than to the magnitude of the magnetic field created by the flaw. To detect deep cracks, it is necessary to use large diameter excitation coils to increase the penetration of the eddy currents in the material under test. SDT structures create a recent addition to the materials exhibiting a large change in resistance. In these structures, an insulating layer separates two magnetic layers. Quantum tunneling through the insulator allows conduction. The angle between the magnetization vectors in the two magnetic layers modulates the magnitude of the tunneling current between the two layers, [1].

3. Conclusion

In this paper there were described the basic principles of nondestructive testing of materials by eddy currents and also there have been referred some types of magnetic sensors. For these sensors there are characterized by a constant sensitivity over a wide frequency range, their small size and the possibility of low magnetic field measurement. These sensors are suitable due to their properties to detect very small defects and defects on the edge of the scanned objects. These facts have great influence on early detection of smaller failures and thus they can prevent major accidents.

Acknowledgement

This work was supported by grants of the Slovak Grant Agency VEGA, projects No. 1/0927/11 and 1/0765/11.

References

[1] ČÁPOVÁ, K., ČÁP, I., JANOUŠEK, L., GOMBÁRSKA, D.: *Advanced probes for electromagnetic non-destructive testing.* In 54th Internationales Wissenschaftliches Kolloquium: proceedings: proceedings. [CD-ROM]. Ilmenau: Impressum, 2009, BRD, 10 pages. ISBN 978-3-938843-45-1

[2] ČÁPOVÁ, K., ČÁP, I., JANOUŠEK, L., SMETANA, M.: *Recent trends in electromagnetic non-destructive sensing.* In ADVANCES in Electrical and Electronic Engineering, Vol. 7, 2008, No. 1-2, p. 322-325. ISSN 1336-1376

[3] DOGARU, T., SMITH, C., SMITH, S.: *New directions in eddy current sensing.* In: Sensors Magazine, vol. 18, No. 6, 2001

[4] SMITH, C., SCHNEIDER, R.: *GMR and SDT sensors and arrays for low-field magnetic applications.* In Sensors EXPO, 1999, Baltimore

[5] http://www.gmrsensors.com (15. 03. 2011)

Transcom 2011, 27-29 June 2011
University of Žilina, Žilina, Slovak Republic

The Impact of Coil Dimensions on Crack Resolution in Pulsed Eddy Current Non-destructive Inspection

*Maria Michniakova
*University of Zilina, Faculty of Electrical Engineering, Department of Electromagnetic and Biomedical Engineering, Univerzitna 1, 01026 Zilina, Slovakia, michniakova@fel.uniza.sk

Abstract. Pulsed eddy current non-destructive inspection of conductive structures is concerned in the paper. Influence of a circular exciting coil's dimensions on a current flowing in the coil under a step voltage excitation is numerically investigated. The coil is positioned in free space as well as over a conductive plate. Orientation of the coil concerning the plate surface is changed to evaluate strength of induction coupling between the coil and the plate. The presented results clearly show that the coupling is the strongest when the coil axis is perpendicular to the surface, while it increases with enlarging the coil diameter. Resolution of defects with various depths based on the sensed responses is then investigated for various diameters of the coil to highlight importance of this parameter for obtaining sufficient information about an inspected structure.

Keywords: Non-destructive testing, pulsed eddy currents, induction coupling, defect resolution.

1. Introduction

Non-destructive inspection is a process or a procedure for determining the quality or characteristics of materials, structural components, or assemblies without altering the subject or his properties. Eddy current testing (ECT) is one of the useful non-destructive inspection methods working based on the principle of electromagnetic induction. Nowadays, this method is widely used in practice for inspection of conductive materials in the energy, aircraft or petrochemical industries.

In ECT, a time-varying current is made to flow in an exciting coil which, in turn, produces an alternating magnetic field around the coil. If the coil is close to a surface of inspected metallic material, eddy currents are induced in the material due to the electromagnetic induction. These eddy currents generate an alternating magnetic field in opposite direction comparing to the exciting field which may be detected either as a voltage across a separate detecting coil or as the impedance variation of the exciting coil. Any discontinuity that appears in the material alters the resulting electromagnetic field and hence the exciting coil's impedance or the back electromotive force (induced voltage) in the detecting coil through the induction coupling. Discontinuities can be detected and possibly evaluated by sensing those changes [1].

The conventional ECT uses the harmonic excitation signal. However, in recent years many R&D activities are concerned on non-harmonic, especially on pulsed eddy current (PEC), excitation. The pulsed driving produces an inherently wideband frequency spectrum, permitting extraction of more selective information that cannot be obtained by performing the inspection using a single frequency. This provides an opportunity for better resolution of defect signals from interfering signals and also more complex information about specimen under inspection can be obtained.

In view of further enhancing of PEC an optimal excitation system has to be selected. In ECT a test piece is coupled to an exciting coil through the electromagnetic induction. Efficiency of the induction coupling is related to lift-off (the distance between the coil and the surface of material under inspection) and also to dimension of the coil. Small-diameter surface coils are primarily used to pinpoint and determine the magnitude of small discontinuities [2].

The impact of particular parameters of a circular exciting coil on the induction coupling is investigated in the paper. The investigation is done indirectly through a time constant of the coil. Influence of the coil diameter on the resolution of cracks with different depths is then evaluated.

2. Numerical model

Numerical simulations are carried out to examine the influence of changes in circular exciting coil dimensions on the time constant of the response current signal under a step voltage excitation. Commercially available software for numerical analyses of electromagnetic fields based on the finite element method has been employed for the purpose. The simulations are performed for three different positions of the coil. At first, the coil is positioned in the air. Then the coil is placed over surface of an inspected plate with a clearance, so called lift-off, of $lf = 1$ mm. Two positions of the coil over the plate are considered; in normal position the coil's axis is perpendicular to the plate surface and in the tangential position the coil's axis is parallel to the plate surface. Influence of the coil position over the plate on the induction coupling is evaluated for different dimensions of the coil.

A plate specimen having the electromagnetic parameters of a stainless steel INCONEL 600 with a conductivity of $\sigma = 1\ \mathrm{MS \cdot m^{-1}}$ and a relative permeability of $\mu_r = 1$ is used in this study. The dimensions of the material are 100x100x10 mm. The shape of the driving voltage signal is unit step with maximum value $U = 10$V. Current in the coil is considered as the response signal. The time constant of each response signal is computed and analyzed for different positions of the coil and for its various dimensions.

The resolution of defects with different depths according to the response signals is then investigated. The defect has a shape of cuboid with a width of $w = 0.2$ mm, a length of $l = 10$ mm and its depth changes in a range $d = 1 \div 10$ mm with a step of 1 mm. The defect is situated in the middle of the material and the coil is situated just over its centre. Two circular coils in the normal position are used for the inspection. The first one has a diameter of $a = 3$ mm, a winding width of $b = 1$ mm and a winding height of $c = 2$ mm. The second coil has dimensions: a diameter $a = 50$ mm, a winding width $b = 1$ mm and a winding height $c = 1$ mm. The coil current is sensed as a response signal; however, the changes in signal due to different depths of the defect are relatively small, therefore the difference signals obtained by subtraction of the response signals with crack and without crack are evaluated. Maximum values of difference signals in relative scale depending on defect's depth are compared for the two coils.

3. Numerical results

Influence of the exciting coil dimensions on the induction coupling between the coil and the plate for the normal as well the tangential positions of the coil are investigated at first. The coil's diameter, winding width and winding height are varied, respectively.

Variations of the coil diameter are shown in Fig. 1. Dependences of the response signals' time constant on the coil diameter for different locations of the coil are displayed in Fig. 2. With increasing the coil's diameter the time constant rises. For small diameters of the coil it is quite difficult to observe differences between plots for various positions of the coil; however with increasing of coil's diameter the differences gets larger. It can be observed that for the coil with diameter of $a = 50$ mm the difference between the time constant for the normal position of the coil and the coil in air is larger comparing to the tangential position and the air. It means that the induction coupling is stronger for the normal position of the coil comparing to the tangential one while the coupling increases with increasing the coil's diameter.

Figure 3 displays variations in the winding width of coil. In this case the diameter of coil is set to $a = 30$ mm. Dependences of the time constant of response signals on the winding width for

different locations of the coil are shown in Fig. 4. By increasing the winding width the time constant decreases and hence also the induction coupling.

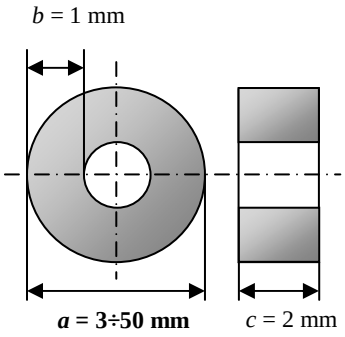

Fig. 1. Coil dimensions

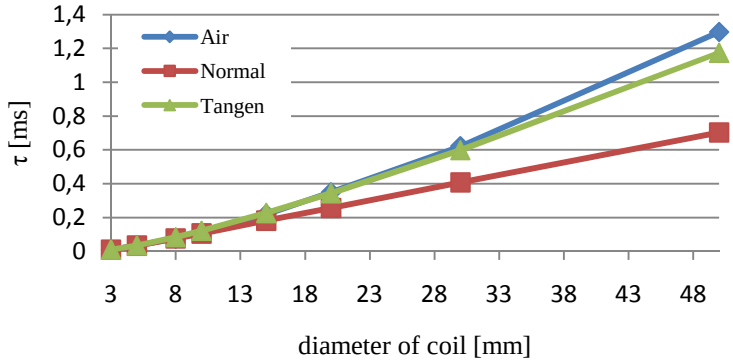

Fig. 2. Time constants depending on the diameter of coil

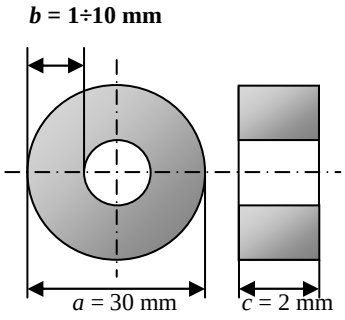

Fig. 3. Coil dimensions

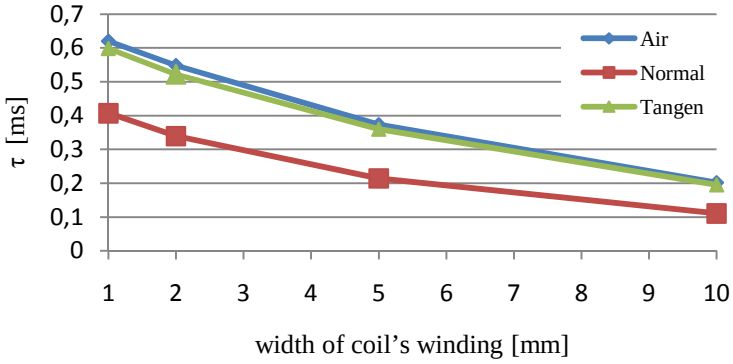

Fig. 4. Time constants depending on the width of coil's winding

The height of coil's winding is changed according to Fig. 5. The dependences of the time constant on the winding height for various positions of the coil shown in Fig. 5 demonstrate that increasing height of the coil's winding decreases the time constant and the induction coupling as well.

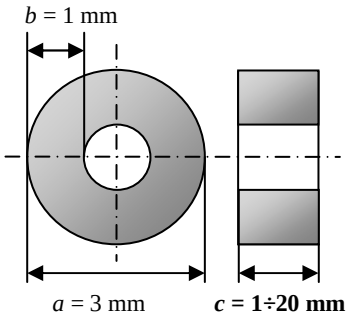

Fig. 5. Coil dimensions

Fig. 6. Time constant depending on height of coil's winding

It can be concluded from the results shown above that the coil oriented in the normal position with large diameter and small winding cross section provides stronger induction coupling with the plate and accordingly more information can be gained about the inspected plate.

In order to confirm these findings resolution between the cracks with different depths from the response signals is studied. Two coils are used for the inspection. The first one has the largest value

of the diameter and the second coil has the smallest diameter according to the considered range shown in Fig. 1. At first, the response signals for a case without crack are calculated. Then, the calculations are repeated for each crack's depth as stated in section 2. Difference signals for each crack's depth are calculated as a difference between the response signal of a crack with particular depth and the response signal without crack. Maximum values of the difference signals for each crack's depth are then determined. Figure 7 displays the maximum values of difference signals in relative scale for the two coils. Using a coil with a diameter of 3 mm the signal gets saturated when the crack is deeper than 4÷5 mm. However, with the 50-mm-diameter coil almost linear relationship between the maximum value of difference signal and the crack depth is obtained. This finding will be further investigated.

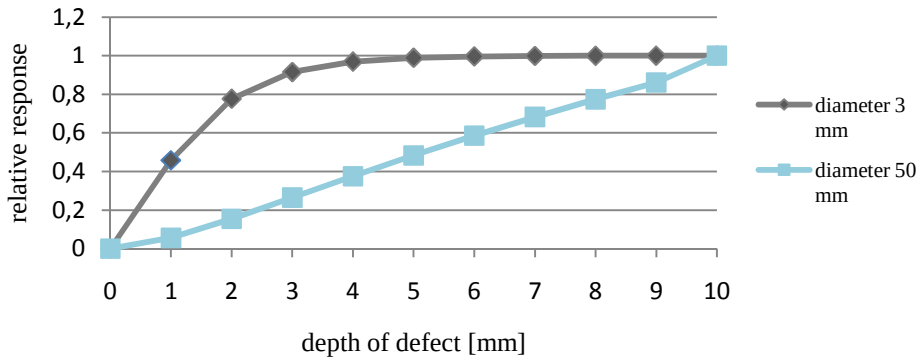

Fig. 7. Dependences of difference signals maximum values in relative scale on the crack's depth

4. Conclusion

The impact of exciting coil's dimensions on the response signal in pulsed eddy current non-destructive inspection was concerned in the paper. Variations of the coil's diameter, width and height of its winding were investigated in view of time constant of response signal and its changes. Three positions of the coil were considered: coil in the air, the normal position of the coil and the tangential one with respect to the surface of an inspected plate specimen in order to evaluate induction coupling between the coil and the plate.

The presented results proved that the normal position of the coil provides stronger induction coupling with the plate comparing to the tangential position. The coupling depends also on the coil dimensions and it gets stronger for larger diameters and smaller winding's cross section of the coil.

The induction coupling has impact on information content of the response signals and therefore it influences the resolution of detected defects. Accordingly, cracks with different depths were inspected with two coils having different diameters. Using a 3-mm-diameter coil the response signal gets saturated with increasing the depth of defect over 4 mm while by using the 50-mm-diameter coil the response signal does not saturate within an investigated range.

Acknowledgement

This work was supported by the Slovak Research and Development Agency under the contract No. APVV-0194-07. This work was also supported by grant of the Slovak Grant Agency VEGA, project No. 1/0765/11.

References

[1] JANOUSEK, L., CAPOVA, K., GOMBARSKA, D., SMETANA, M.: *Progress in eddy-current non-destructive evaluation of conductive materials*. In: ACTA TECHNICA CSAV, Vol. 55, No. 1, April 2010, ISSN 0001–7043, p. 13-28.

[2] MIX, P.E.: *Electromagnetic testing method*. In: Introduction to nondestructive testing: A training Guide, Second Edition, John Wiley & Sons, Inc., Hobokend, NJ, USA, 2005.

Transcom 2011, 27-29 June 2011
University of Žilina, Žilina, Slovak Republic

Friction Respecting Energy Saving PMSM Position Control

[*]Peter Minarech, [*]Jan Vittek, [*]Jan Faber
[*]University of Žilina, Faculty of Electrical Engineering, Department of Power Electrical Systems,
Univerzitná 1, 01026 Žilina, Slovakia, Peter.Minarech@kves.uniza.sk

Abstract. This paper presents a new type of energy saving control algorithms for exact position control of permanent magnet synchronous motor. These algorithms are based on three main parts: prescription, advancer and main control algorithm. Prescription can be created by minimum energy generator, by ramp or any algorithm which can achieve demanded position for maneuver time. Minimum energy generator creates a special type of acceleration profile, where the magnitude and time of acceleration resp. deceleration can be changed. The three known types of acceleration profile can be created: square, sinusoidal and triangle. The other significant part of new control scheme is advancer. Advancer can be created by feed – forward component or pre – compensator. The role of advancer is, that the rotor will follow the prescribed reference position with zero lag. Vector control in cascade structure, forced dynamics control (FDC) or sliding mode control (SMC) can be applied as main control algorithms. Also all position control algorithms respects PMSM vector control condition.

Keywords: Minimum energy generator, Zero dynamics lag pre-compensator, Position control, Acceleration profile, Velocity profile, Energy expenditure

1. Introduction

Savings of electrical energy consumption can limit negative influence and bring substantial profit to environment. New types of control for electrical motors (rotating and also linear) can save part of input energy consumption for rotor position change request. New type of drives control can be applied to all servosystems controlled on prescribed position. Implementation of such control algorithms can save up to 50% of input energy when the same inverter and the same machine are used. To minimize energy demand a specified velocity-time profile is derived to achieve prescribed dynamics for reference position.

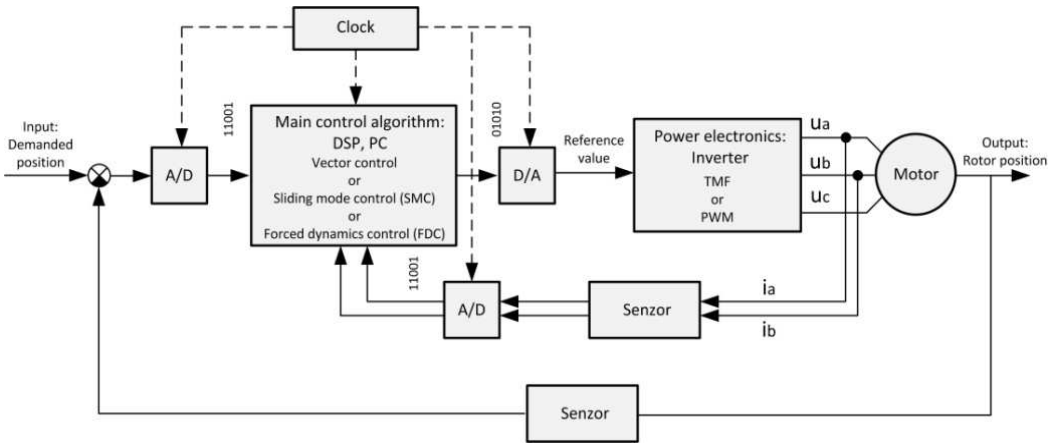

Fig.1. Basic concept of AC electric drives controlled on prescribed position

2. Control system development

2.1. Basic concept of position control

The basic concept of AC drives controlled on prescribed position is shown in Fig. 1. The input of the control diagram is demanded position and rotor position is controlled output. Main control algorithm can respect principles of vector control in cascade structure, sliding mode control (SMC), forced dynamics control (FDC) or any other algorithm for position control of the rotor. If FDC as main control algorithm is applied, then the observer is necessary. Fig. 2 shows block diagram of PMSM q – axis for feedback position vector control taking into account frictional losses. Position loop consist of position P – controller and compensator (*first order filter*) for input of speed loop, which compensate zero in closed-loop transfer function. Speed PI controller and saturation creates inner velocity loop. Saturation limits demanded PMSM q - axis stator current component. Current loop is represented by the first order transfer function. Total electromagnetic torque created by machine is product of q - axis stator current and torque constant K_M, if vector control condition ($i_{d\_dem} = 0$) is satisfied.

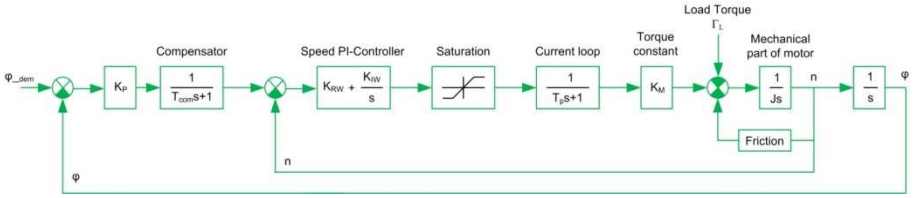

Fig.2. General block diagram of PMSM q – axis feedback position control

2.2. Friction respecting

Friction in electrical rotating machines consists of several components. The total friction consists of static friction, Coulomb friction, viscous friction and Stribeck´s effect. Static friction is friction between two solid objects at zero speed. The coefficient of static friction, denoted as μ_s, is usually higher than the coefficient of Coulomb friction. The effect of static friction must be overcome by a torque before an object starts to move. Static friction can be calculated as (1), where F_n is normal force. Static friction coefficient μ_s for dry and clean steel – steel contact is *0,80* and for lubricated steel – steel contact is μ_s *0,16*.

$$F_s = \mu_s . F_n \tag{1}$$

Coulomb friction, F_c is independent of speed value, but it changes its signum with direction of motion. The Coulomb friction may take any value from zero up to $f_c F_n$ and usually is less than static friction F_s. For the same materials can be calculated as (2).

$$F_c = f_c . F_n . sgn(\Omega) \tag{2}$$

Viscous friction occurres between two solid surfaces and lubricant can decrease its value. Viscous friction is direct proportional to the velocity and can be expressed as (3).

$$F_v = f_v . F_n . \Omega \tag{3}$$

All types of friction (F_c, F_s, F_v), form together total friction F_t. This function and its components used for verification of control algorithms is shown on Fig. *3a,b,c*.

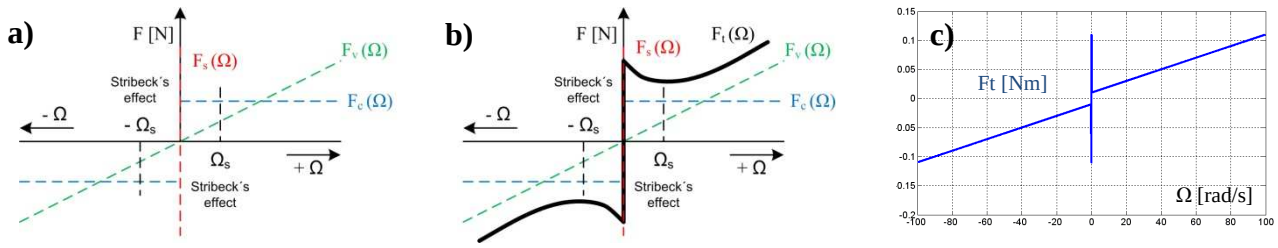

Fig.3a,b - Static, Coulomb, viscous and total friction as a function of mechanical angular speed
Fig.3c – Friction, which is used for simulation verification of energy saving position control

2.3. Energy saving concept of position control

For position control with best energy strategy it is necessary to create an algorithm minimizing the velocity peak for a given position change. The goal of a new position control strategy is to minimize energy consumption. In general reference position without peaks in its derivative is the solution. Trapezoidal speed profile is good solution to correspond to this theory. From speed profile then acceleration profile, which takes into account load torque is derived. It means that the magnitude and time of acceleration or deceleration is changed such a way that new position control algorithm is energy optimal and load torque is completely compensated. Concept of main control algorithm generation for energy saving is shown in Fig. 4.

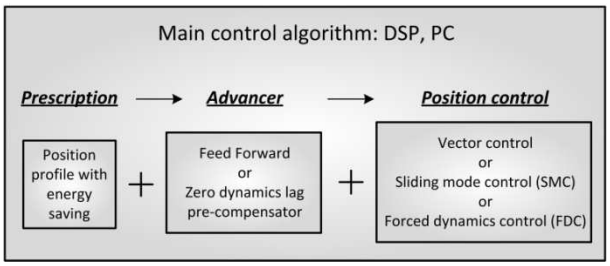

Fig.4 – Energy saving control algorithm

2.4. Generator of energy saving position profile

The best position control strategy is to minimize the velocity for a given position change. Many different speed profiles can be created, which can achieve demanded position at specified settling time. Some of them are shown in the Fig. 5.

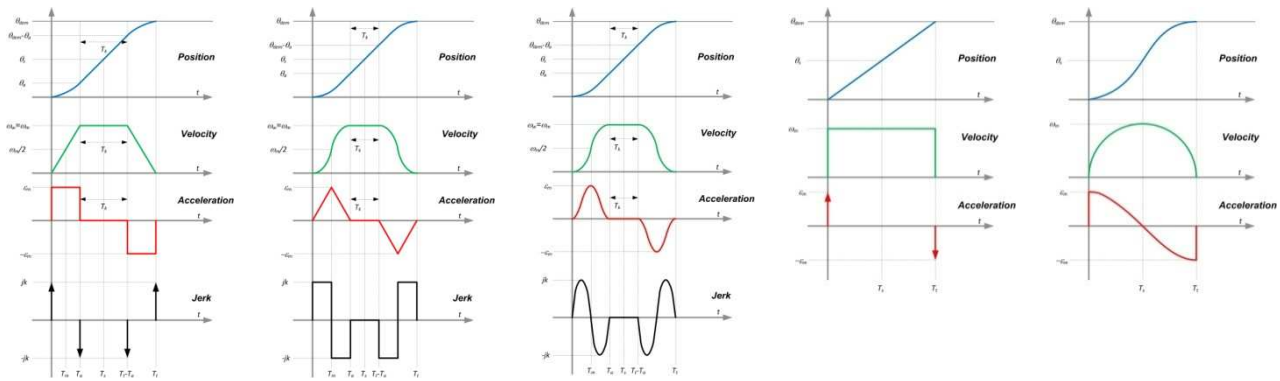

Fig. 5 – Position, velocity and acceleration energy saving profiles

Energy saving generator creates three types position profiles of S – curve family where square, triangle and sinus acceleration profiles are used. If square acceleration profile is created, then trapezoidal velocity profile is obtained. On the other hand, if control algorithm creates triangle acceleration profile corresponding velocity profile called canonical is obtained. Further possibility for energy saving position profile is ramp. This position profile creates long constant velocity zone with small magnitude. The other energy saving position profile is half ring velocity profile, which creates typical S – curve for prescribed position. Energy expenditures for different types of PMSM position control are shown in Fig. 6. Final position change was set to *3* revolutions (*18,85* radians)

for maneuver time *0,1*s. Time optimal position control with decrease torque has the highest energy expenditure and therefore its value is assigned as *100%* for comparison.

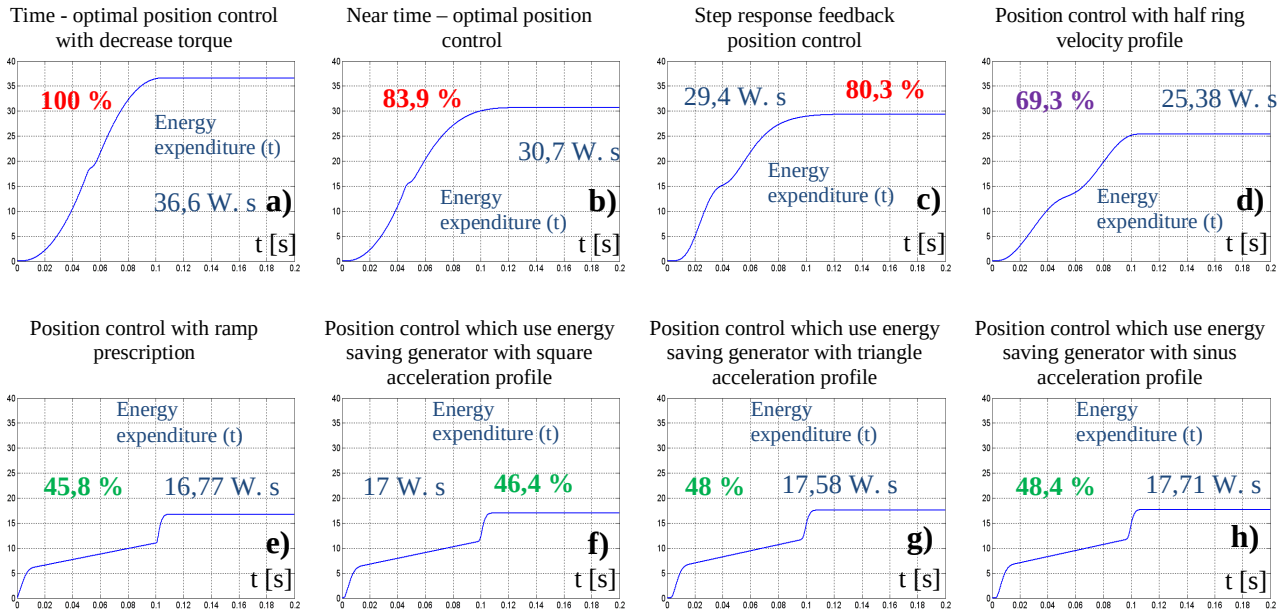

Fig. 6 – Simulation verification results of energy expenditure for different types of position control with PMSM

3. Conclusion

Presented simulation results confirmed that a new energy optimal position control algorithm can save a significant portion of drive's input energy. These algorithms are based on position and speed profile generation, feedforward precompensation and suitable position control algorithm. Acceleration, constant speed and deceleration of a new energy saving algorithm complies with prescribed time for position maneuver. This way the velocity of the drive is reduced and therefore less energy is dissipated due to position maneuver. Simulation results confirm that proposed control algorithm can save substantial portion of input energy if compared with time optimal position control or position step response control.

Acknowledgement

The authors wish to thank for support the Slovak Grant agency VEGA

References

[1] AREVALO, V.M., OPTICOS, A., ENSENADA, B.C.: *Sinusoidal Velocity Profiles for Motion Control*, Mexico 22830

[2] VITTEK, J., BRIŠ, P.: *Experimental Verificatiopn of Energy Saving Position Control Algorithm Applied to the Drives with PMSM*, University of Žilina, Faculty of Electrical Engineering, Žilina, Slovak Republic

[3] MINÁRECH, P., VITTEK, J.: *Energy Demands of the Position Drives employing PMSM Control by Forced Dynamics*, Department of Power Electrical Systems, Faculty of Electrical Engineering, University of Žilina, ISBN: 978-80-554-0196-6

[4] MINÁRECH, P., MAKYŠ, P., VITTEK, J.: „ *PI-Controllers Determination for Vector Control Motion* ", 18th Annual Conference Technical Computing Bratislava 2010, Bratislava, Slovakia, 2010, October, 20, p.: 70-77, 978-80-970519-0-7

[4] DODDS, S. J., SOORIYAKUMAR, G., PERRYMAN, R.: *Minimum Energy Forced Dynamics Control of PMSM*. Energy And Environmental Engineering Series, Proc. of the 3rd IASME/WSEAS Int. conf. on Energy & Environment, Cambridge, United Kingdom, pp.: 173-179.

Transcom 2011, 27-29 June 2011
University of Žilina, Žilina, Slovak Republic

Dynamics of RC circuit with Esaki's diode

*Anna Najmanova
*University of Žilina, Faculty of Humanities, Department of Mathematics, Univerzitná 8215/1, 01026 Žilina, Slovakia, anna.najmanova@fpv.uniza.sk

Abstract. Target of the article is the application of mathematical analysis and theory of differential equations in physical-technical models. We are interested in dynamic properties of RC circuit with Esaki diode, which has nonlinear volt-ampere characteristics. We are studying time characteristics of voltage in circuit. By phase diagram we are following the stability of critical points of circuit and bifurcation means the change of stability.

Keywords: Differential Equations, critical point, RC circuit, Esaki diode, volt-ampere characteristics, stability, bifurcation.

1. Introduction

This paper is studying dynamics RC circuit with Esaki diode, this problem can be used in education at university as a didactics process. Connection between differential equation and some physical or technique problems is greatly proof.

Course of RC circuit is characteristics of nonlinear differential equation and this equation is resolving as ordinary separation differential equation. Solution this equation gives us information about circuit – critical points, bifurcation point and with their help we can study characteristics of voltage in circuit.

2. Mathematics model RC circuit with Esaki diode

In mathematical RC circuit, which diagram is on the picture, there is resistance R and condensator C. Suppose that, on condensator in the time τ is electrical charge and in the condensator is voltage ζ . Then the condensator is beginning discharge in resistance R and in circuit is electric current . Voltage in condensator begins to fall. We study time behaviour of voltage $u(t)$.

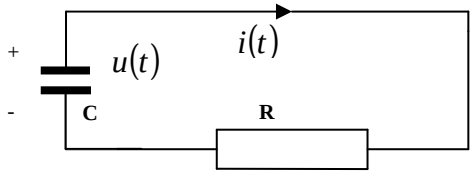

Fig. 1. Electrical RC circuit

From physics is noted, that between voltage on condensator $u(t)$ and time behaviour intensity of electric current $i(t)$ the next relative is valid

$$\left.\begin{aligned} \frac{du(t)}{dt} &= -\frac{1}{C}i(t) \\ i(t) &= \frac{1}{R}u(t) \end{aligned}\right\} \Rightarrow \frac{du(t)}{dt} = -\frac{1}{RC}u(t). \tag{1}$$

The time behaviour voltage on condensator we give as solution of Cauchy problem

$$\dot{x} = -\frac{1}{RC}x,\ x(\tau) = \zeta\ . \tag{2}$$

Then solution is function

$$u(t,\tau,\zeta) = \zeta e^{-\frac{t-\tau}{RC}},\ t \geq \tau\ . \tag{3}$$

Now we change in RC circuit the resistance R with Esaki diode

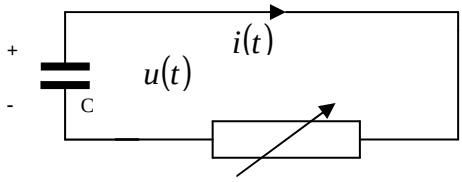

Fig. 2a. Electrical circuit with Esaki diode

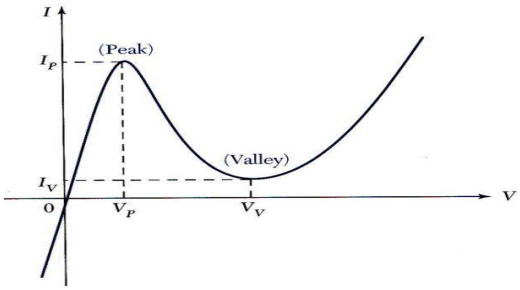

Fig. 2b. Volt-amper characteristic of Esaki diode

In circuit with Esaki diode is noted from physics, that between voltage $u(t)$ and intensity of electric current $i(t)$ is valid the next relative

$$\left.\begin{aligned} \frac{du(t)}{dt} &= -\frac{1}{C}i(t) \\ i(u) &= -u(t)\left[1-u^2(t)\right] \end{aligned}\right\} \Rightarrow \frac{du(t)}{dt} = \frac{1}{C}u(t)\left[1-u^2(t)\right]. \tag{4}$$

Then function u we can search as solution general differential equation

$$\dot{x} = \frac{1}{C}x\left(1-x^2\right) \Rightarrow \frac{dx}{x\left(1-x^2\right)} = \frac{1}{C}dt,\ x \neq 0, x \neq \pm 1\ . \tag{5}$$

Thus for time behavior of voltage $u(t)$ we get

$$\ln\frac{u^2(t)}{1-u^2(t)} = \frac{2}{C}t + 2c_1,\ u(t) \neq 0, u(t) \neq \pm 1, c_1 \in R\ . \tag{6}$$

3. Dynamics properties RC circuit with Esaki diode

In general we do not know to solve nonlinear differential equations, but important information we get from critical point, stability through the use of phase diagram and bifurcation.

Time behaviour of electric intensity $x(t)$ in circuit RC, where resistor R is replaced by Esaki's diode is realised by differential equation

$$\dot{x} = \frac{1}{C} x\left(1 - x^2\right). \tag{7}$$

Equation (7) is particular case of differential equation

$$\dot{x} = \alpha x + a x^3,\ a \neq 0, \tag{8}$$

where $\alpha \in (-\infty, \infty)$ is a parameter and is important for following change of stability.

3.1. Bifurcation in differential equations

If differential equation includes parameter, that parameter can way trough of critical value. It will set qualitative change in character of critical point or in relevant trajectory. This change is called bifurcation and point is point of bifurcation.

In some kind of bifurcation come situation, when the critical point lost stability. The qualitative change of stability shouldn't always means change from stability to instability (or opposite).

3.2. Critical points and phases diagrams of differential equation

The phase's diagram of (8) means relation between function x and his derivation $\dot{x}$. Critical point we get from relation $\dot{x} = 0$, i. e. it is solution of equation

$$\alpha x + a x^3 = 0,\ a \neq 0. \tag{9}$$

The diagram of bifurcation means relation between parameter α and critical point x.

For $\alpha = 0$ (8) has one critical point, which we get from equation $ax^3 = 0$.
Critical point $x = 0$ for $a > 0$ is unstable and for $a < 0$ is stable, as we can see on phase and bifurcation diagram.

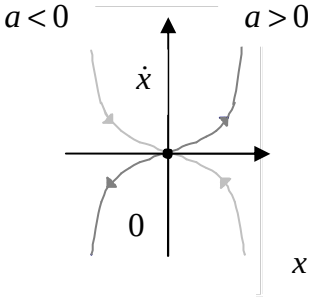

Fig. 3. The phases diagram for $\alpha = 0$

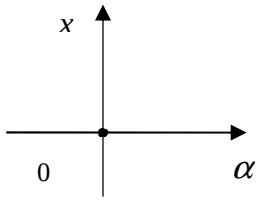

Fig.4. The bifurcation diagram for $\alpha = 0$

Case $a > 0$**:**

If $\alpha > 0$ then (8) has one critical point, which we get from (9).
Because equation $\alpha + ax^2 = 0$ hasn't solution in set of real numbers. Critical point $x = 0$ is unstable.

If $\alpha < 0$ then (8) has three critical points $x = 0$ and $x = \pm\sqrt{\frac{-\alpha}{a}}$.

The critical point $x = 0$ is stable and critical points $x = \pm\sqrt{\frac{-\alpha}{a}}$ are unstable, which show diagrams on picture.

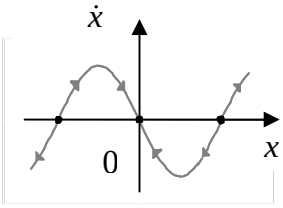

Fig. 5. The phases diagram for $a > 0, \alpha < 0$

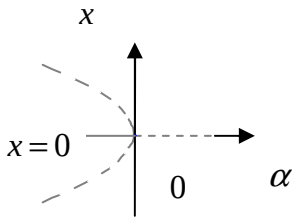

Fig. 6. The bifurcation diagram for $a > 0$, $\alpha < 0$

Case $a < 0$**:**

If $\alpha > 0$ then (8) has three critical points $x = 0$ and $x = \pm\sqrt{\frac{-\alpha}{a}}$.

The critical point $x = 0$ is unstabile and critical points $x = \pm\sqrt{\frac{-\alpha}{a}}$ are stable, which show diagrams on picture.

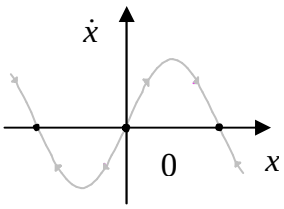

Fig. 7. The phases diagram for $a < 0, \alpha > 0$

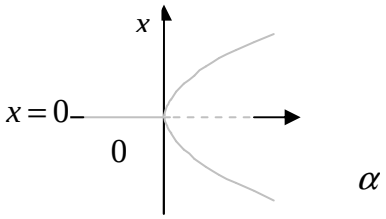

Fig. 8. The bifurcation diagram for $a < 0, \alpha > 0$

If $\alpha < 0$ then (8) has one critical point $x = 0$, which is stable and equation $\alpha + ax^2 = 0$ hasn't solution in set of real numbers.

Time behavior of voltage $x(t)$ in RC circuit with Esaki diode is realized by (7), where

$$a = -\frac{1}{C} < 0,\ \alpha = \frac{1}{C} > 0.$$

Thus solution of (8) has three critical points: $x = 0$ is unstable,
$x = \pm 1$ are stable.

Equation $f(x) = \frac{1}{C}x(1 - x^2)$ has derivation $f'(x) = \frac{1}{C}(1 - 3x^2)$, which in critical point $x = 1$ is negative thus poin $x = 1$ is asymptotic stable, i. e. voltage $x(t)$ in circuit will be convergent to 1 volt. So voltate in circuit will move around value 1volt.

4. Conclusion

Aim of paper is alanysis of dynamics properties of RC circuit with Esaki diode, which has nonlinear volt-amper characteristic. We found that in circit are thee critical point, two are stable and one is unstable.

References

[1] NAGY, J.: *Elementární metody řešení obyčejných diferenciálních rovnic*. SNTL, Praha, 1978.

[2] HANUŠTIAKOVÁ, L. – OLACH, R.: Asymptotic and oscillatory properties of neutral differential systems, Studies University of Žilina, Math. Series 19 (2005), p. 9-18.

[3] ILAVSKÁ, I., NAJMANOVÁ, A., OLACH, R.: Existence of nonoscillatory solution of nonlinear delay differential equations, Journal of Applied Mathematics, Vol. 2, No. 2 (2009), p.83-88, ISSN: 1337-6365.

[4] *ILAVSKÁ, I., NAJMANOVÁ, A.*: *Oscillatory properties of nonlinear neutral differential systems*, TRANSCOM 2009, University of Žilina, p. 23-27, ISBN: 978-80-554-0036-5.

[5] KREYSZIG, E.: *Advanced Engineering Mathematics*, J. Wiley and Sons, New York, 1983.

[6] WIGGINS, S.: *Introduction to Applied Nonlinear Dynamical Systems and Chaos*, Springer-Verlag, New York, Berlin, London, Paris, Tokyo, 2003.

Transcom 2011, 27-29 June 2011
University of Žilina, Žilina, Slovak Republic

The measurements of the chopper supplied tram electromagnetic field emission

*Marek Patoka
*Warsaw University of Technology, Faculty of Electrical Engineering, Institute of Electrical Machines, Electric Traction Division, Pl. Politechniki 1, 00-662 Warszawa, marek.patoka@wp.pl

Abstract. This paper describes electromagnetic field measurements according to EN-50121-3-1 standards. Apart from the methodology of the measurements, it consists of the limits of electromagnetic disturbances from the trams. The measurements of the power electronics supplied tram were taken real conditions. The paper includes a proper comparison between radiated emission of the tram, ambient noise and the threshold values. The conclusion whether the tram has obtained the positive or negative opinion was also carried out.

Keywords: electromagnetic field, electric field, magnetic field, EMC, electric traction, tram, railway.

1. . Introduction

Nowadays, when the sustainable development is a goal, the environmental problems become more significant. Due to a huge growth of the amount of electrical devices people begin paying attention not only to the common environmental aspects such as electrical corrosion or vibration, but also to electromagnetic field (EMF) emission. The more powerful the device is the more EMF emission in its surroundings appears. Common knowledge is that magnetic field (MF) is related to current, whereas electric fields (EF) to voltage. One of the most important branches of the industry, which uses high voltages (so produces EMFs), is the electric traction. In bigger metropolis, the most comfortable way of communication is electric transport – trams, trains or underground. Well-developed tram network makes communication easier, but also causes the EMF emission from the rolling stock, to appear almost everywhere.
The set of the EN-50121 standards provides limitation for the EMF emission of the railway as a whole to the outside world. Part 3-1 considers Rolling stock – "Train and complete vehicle"
and specifies the emission and immunity requirements for all types of rolling stocks. [1]

2. Crucial information about the EN-50121-3-1 standards.

H field			E field		
Subrange [Hz]	BW [kHz]	Sweep time [ms]	Subrange [Hz]	BW [kHz]	Sweep time [ms]
9k – 59k	1	300	30M – 230 M	100	42
50k – 150k	1	300			
150k - 1,15 M	9	37	200M – 500 M	100	63
1M – 11 M	9	370			
10M – 20 M	9	370	500M – 1 G	100	100
20M – 30 M	9	370			

Tab. 1. Guideline for the test (BW -Bandwidth)

The EN-50121-3-1 standard describes the method of the proper measurements and specifies the limits in important frequency subranges. The measurements have to be carried out from the

frequency 9 kHz to 1 GHz and they have to consist of two tests: stationary (when the vehicle is standing), and slow moving (when the vehicle is moving with low speed). To follow the standard requirements, measurements have to be done in 9 subranges (Tab.1).

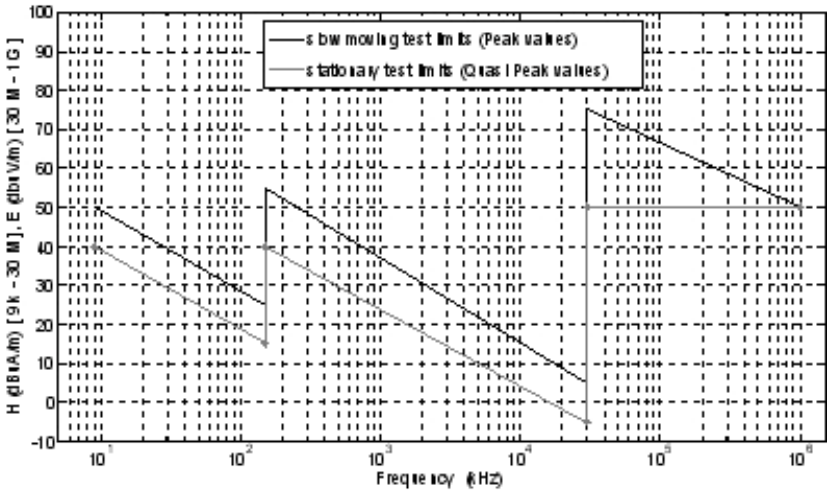

Fig. 1. The limits for the electric and magnetic field emission according to EN-50121-3 for "stationary" and "slow moving" tests.

To cover full frequency range, three types of antennas should be typically used:

- for magnetic field in the range 9kHz – 30MHz, loop antenna
- for electric field in the range 30MHz – 300MHz, biconical dipole
- for electric field in the range 300MHz – 1GHz, log-periodic antenna

Biconical and log-periodic antennas could be replaced by the biological antenna, which covers whole range of the electric field frequency.

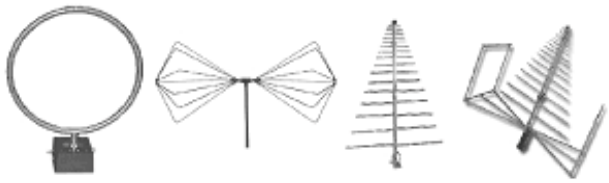

Fig. 2. Antennas used for the EMF measurements (from the left: loop antenna, biconical antenna, log-periodic antenna, biological antenna) [source: www.ahsystems.com]

The threshold values for the emission are specified in field strength units (Fig. 1.). That is the reason why the antenna factors (AF) and cable losses (CL) should be used to convert the terminal voltage of the antenna to the field strength.

$$\frac{dBuV}{m} = dBuV + AF + CL, \tag{1}$$

$$\frac{dBuA}{m} = \frac{dBuV}{m} - 51.5dB. \tag{2}$$

Antennas should be placed at the distance of 10m from the track axis. The height of the antenna centre above the rail level has to be:

-for loop antenna from 1 to 2 meters
-for the dipole, log-periodic or bilogical antennas, within 2,5 m to 3,5 m.

The norm specifies what have to be considered during measurement to fulfill the test requirements:

- in the distance of 10 m there should be no bridges, tunnels or vehicles
- the measuring point should be in the midpoint between catenary supporting masts
- in case of double track place the antennas on the side of the track which is being used
- the catenary should be an “infinite” line on both sides of the measurement point, minimum clear length should be 500 m for urban vehicles
- discontinuities of the catenary should be avoided: section insulators, substations
- proximity of the power lines including underground cables should be avoided
- on the same feeding section no other vehicles should be operating or within the distance of 2 km
- measurements of ambient noise should be made
- if at specific frequencies ambient noise is higher than the limit less 6 dB the measurements at these frequencies should not be considered- they should be noted in the test report [1,2].

3. Measurements

The emission test was taken from the dc motor tram with the nominal power of 4 x 45 kW fed from 600 V catenary via the chopper converter.

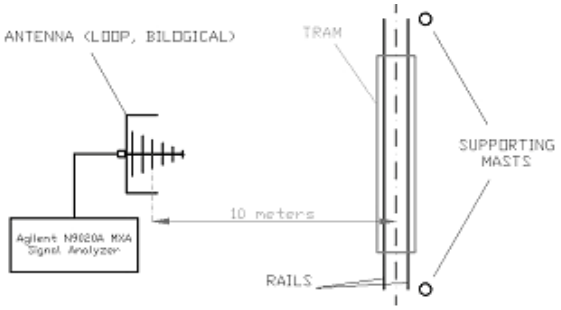

Fig. 3. View of the measurement place.

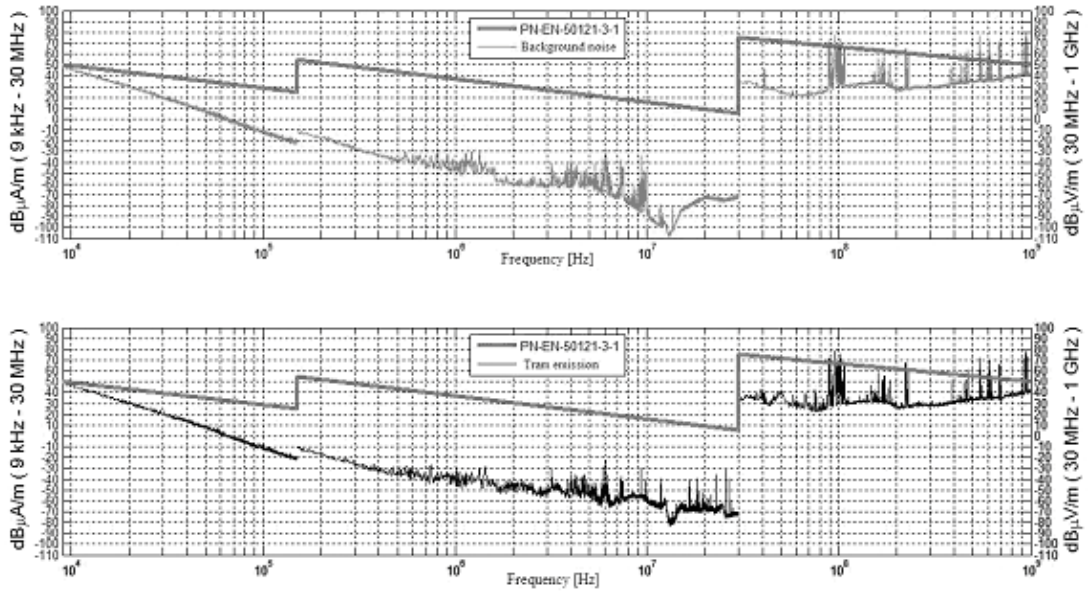

Fig. 4. The comparison of the background noise and tram emission with the limits specified in PN-EN-50121-3-1, for the “slow moving” test.

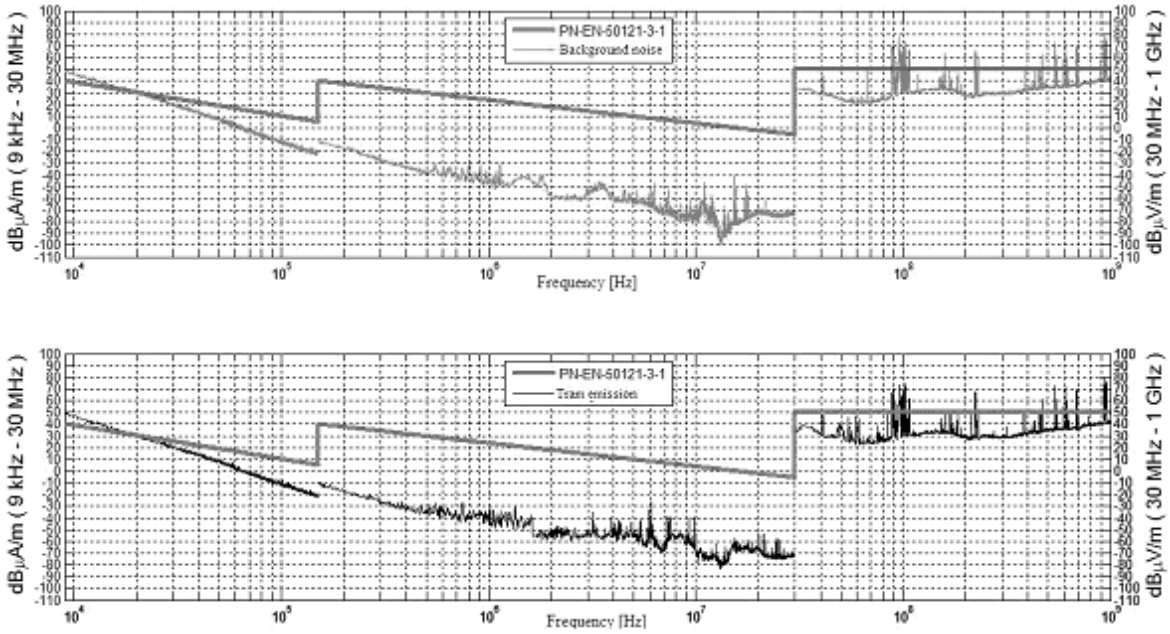

Fig. 5. The comparison of the background noise and tram emission with the limits specified in PN-EN-50121-3-1, for the "stationary" test.

Before proper measurements were taken, the background noise had been registered.
As it is shown in Fig. 4, 5, the results could be divided into 3 parts. First two parts (9k - 150k and 150k – 30M) are responsible for magnetic field emission, the last part – for the electric field emission (30M - 1G). In the lowest and the highest frequencies the ambient noise and the disturbances caused by the tram are almost the same, but within the middle frequencies (10M – 55M) the differences are visible – the tram emission is about 10-30 dBuV(A)/m higher.
Above mentioned relationship is the same in both "slow moving" and "stationary" test.

4. Conclusions

The measured tram acquired positive opinion according to the EN-50121-3-1 standard. All values of EMF, which have crossed the limit threshold, were caused by the ambient noise. The limits for the "stationary" test are more restrictive than for the "slow moving" test, due to this fact the ambient noise has exceeded the limit for the lower frequencies only in one case. All transgressions of the EN-50121-3-1 limits in higher frequencies were caused also by the ambient noise particularly by GSM devices. All disturbance values of EMF caused by tram are lower than limits specified in the above-mentioned standard.

5. References

[1] Series of European Norms, *Railway Applications – Electromagnetic Compatibility*, PN-EN-50121:2008

[2] SZMIGIERA G. Measurements of electromagnetic fields generated by the different type of tram rolling stock owned by the Warsaw Tramways, *Bachelor of Science in Engineering Thesis, Warsaw 2010.*

Transcom 2011, 27-29 June 2011
University of Žilina, Žilina, Slovak Republic

Measurement techniques of cell membrane electrical quantities

[*]Roman Radil
[*]University of Zilina, Faculty of Electrical Engineering, Department of Electromagnetic and Biomedical engineering, Univerzitna 8215/1, 01026 Zilina, Slovakia, radil@fel.uniza.sk

Abstract. The article reviews recently used measurement techniques of cell membrane bioelectric quantities and properties. It deals with principles of a single cell recording method, specifically with patch-clamp techniques. This review provides also brief information about roles of membrane voltage and its relationship with voltage gated ion channels. According to the publications summarized in this paper it can be concluded that described techniques could provide important information about electrical processes on the cell level, and thus could be used for recording of bioelectrical responses to external applied low frequency electromagnetic field.

Keywords: membrane voltage, membrane channel currents, patch clamp, voltage clamp, current clamp.

1. Introduction

Electrical properties of biological cells have become a very interesting field of research in recent years. One of the most important bioelectrical quantities is a cell membrane voltage, which is aligned with an activity of ion channels and thus with the cell proliferation processes. From this point of view cell membrane voltage measurements are necessary for understanding the bioelectrical processes, which are related with the whole cell life.

The invention of microelectrodes allowed measurement of electric properties and quantities, especially voltages, in such small objects as it is in case of biological cells. The method of measurement was firstly published in 1949 by G. Ling and R.W. Gerard in [1]. This started further investigations of bioelectric cell properties. The development of measurement methods and techniques has rapidly grown. Principles of the modern measurement techniques are described in the following text.

2. Single cell measurements

There are several methods used for bioelectric measurements on a cell level, i.e. methods using voltage sensitive dyes, methods with membrane penetrating microelectrodes. One of recently most used methods is a patch-clamp, which was invented at the end of 70's by E. Neher and B. Sackmann and published in [2]. This method was a step forward in research of bioelectrical membrane properties. Patch-clamp technique provides information about currents through membrane channels as well as membrane voltage.

Principle of the method is in electrical isolation of membrane patch from the external solution and recording current flow into the patch. This is achieved by pressing a fire-polished glass pipette, which has been filled with a suitable electrolyte solution, against the surface of a cell and applying light suction. Providing both glass pipette and cell membrane are clean, a seal whose electrical resistance is more than 10 GΩ is formed. The higher the seal resistance, the more complete is the electrical isolation of the membrane patch. Secondly, a high seal resistance reduces the current noise of the recording, permitting good time resolution of single channel currents, currents whose amplitude is in the order of 1 pA [3]. As it is illustrated in Fig.1a, it is necessary that the area of patch from which recordings are made be small in comparison with the area of whole cell membrane. An equivalent circuit for the recording set-up is shown in Fig. 1b.

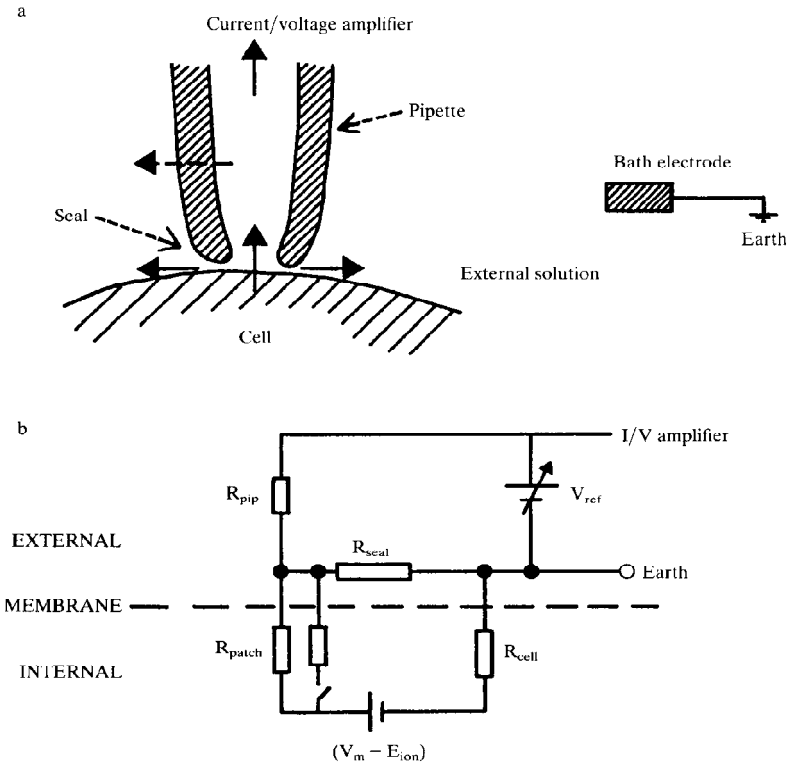

Fig. 1. The relation of pipette to cell and the equivalent electrical circuit during patch clamp recording.

The opening of an ion channel is represented as the closing of the switch. The pipette resistance and seal resistance are in series between the amplifier and earth (the external solution) and the patch and cell resistances are in parallel with the seal resistance in this path. The background noise level is also minimized by a high seal resistance. The variance of the current noise (in A^2) through a resistor (R, Ω) is related to the Johnson voltage noise due to the resistance, being given by:

$$s_i^2 = 4kTf_c/R, \quad (1)$$

where k is Boltzmann's constant, T is temperature (°Kelvin), and f_c is the bandwidth (Hz) i.e. the low pass filter setting. Thus, for a 10 GΩ resistor at 20°C, the standard deviation of the current noise at 1 kHz will be 0.04 pA, but for a resistor of 100 MΩ it will be 0.4 pA. In the recording situation used in patch clamp (Fig. 1), resistor current noise will depend on all the resistive paths to ground from the amplifier input, decreasing as resistance increases. In the earliest experiments the seal resistance was less than 100 MΩ and the noise prevents good resolution of currents smaller than 4 or 5 pA. The achievement of gigaseal radically improved the signal-to noise ratio.

Currently, the patch-clamp technique is still being developed, and resulted in improvements of modern single cell measurement methods. The patch-clamp technique is used in various modes as it is shown in Fig.2. These modes can be summarized and briefly described as follows:

Cell-attached recording

This mode is used to study single channel currents. It is necessary to keep good mechanical and vibrational stability for long enough to record sufficient data. Opening of voltage-activated channels may be achieved by stepping the potential inside the pipette. Often the pipette solution will have the same ionic composition as the bath solution; substitution of ions may be made for studies of permeability properties of channels.

The membrane potential of cell-attached patches (V_{patch}) is determined by that of the cell interior (V_{cell}) as well as by the pipette (V_{ref}). The membrane potential is therefore:

$$V_{patch} = V_{cell} - V_{ref}\,. \quad (2)$$

Cell-attached patch-clamp current recording reveals messenger-mediated mechanisms by which agonists cause opening or closure of single ion channels. The cell-attached configuration of patch clamp is recently used in researches such as [4] and [5].

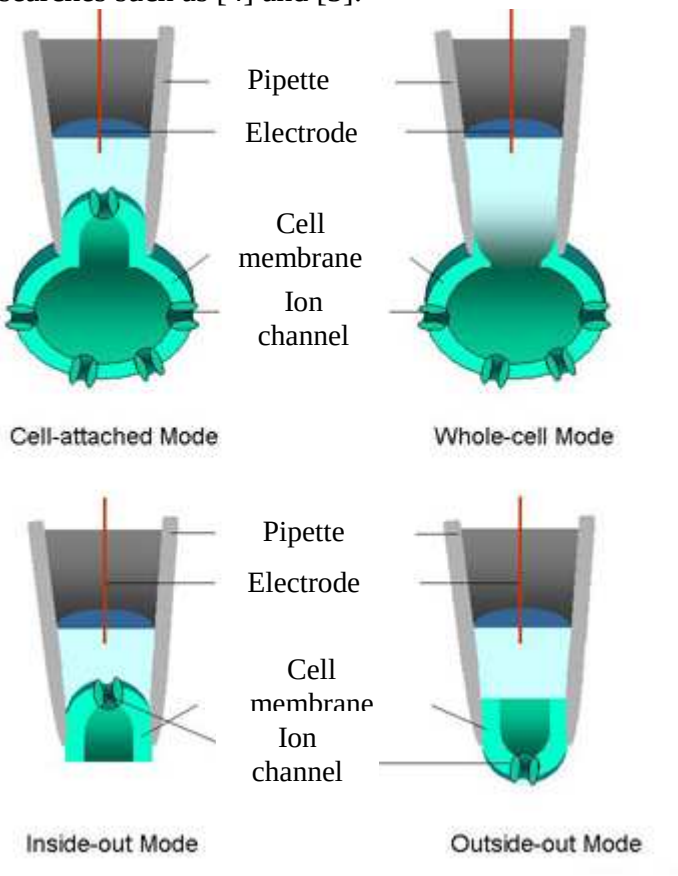

Fig. 2. Main modes of the patch-clamp technique

Cell-free, excised patches

Much work is done using patches in the cell-attached mode, but the resting potential of the cell is not known and neither intra- nor extracellular ionic concentrations can be changed easily. For these reasons, it is sometimes essential to work using a cell-free mode, with excised or ripped-off patches. There are two kinds:

Inside-out - made by pulling the membrane patch off the cell into the bath solution.

Outside-out - made by applying suction to destroy the membrane isolated by the patch pipette and then pulling the pipette away from the cell. The membrane should reseal to give a patch of membrane whose intracellular face is in contact with the pipette solution.

Whole-cell recording

Whole-cell recording is achieved by destroying the membrane patch using suction so that the cell, whose interior then comes into contact with the solution in the pipette, may be voltage or current-clamped. The principle of this mode is illustrated in Fig. 3. Practical application of this technique is in research of ion channel activation/ inhibition and current flow through the ion channels as it is in case of the publications [6, 7]. Most of applications of mentioned techniques are in research laboratories, where investigations about bioelectric cell properties take place, as it is illustrated in Fig. 4.

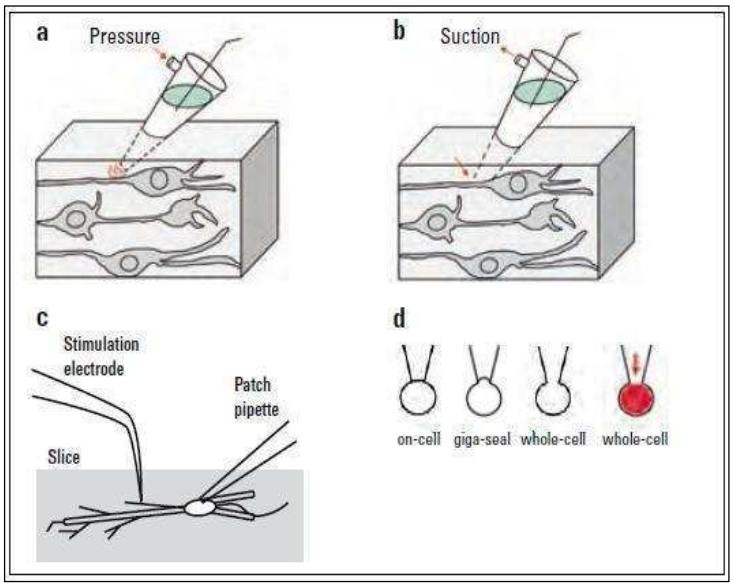

Fig. 3. Principle of whole cell recording [8]

Fig.4. An example of applied patch-clamping

3. Conclusion

Modern techniques in bioelectric cell properties research tend to be noninvasive or mini invasive. The patch-clamp method described in this article is currently frequently used for a single cell recording and provides important information about cell membrane, cell membrane structures, and their bioelectric properties. Development of mentioned techniques allowed study of such small membrane structures as it is in case of ion channels and current flow through these structures, or voltage changes across the cell membrane. Acquired values of electric currents were in order of pA and voltages in order of mV. It is proven, that the cell membranes and their ion channels significantly influence the whole cell life and plays important role in cell proliferation. According to this, it could be concluded, that such small values of electric currents and voltages act as a control signal for cell differentiation and proliferation.

References

[1] LING, G., GERARD, R. W. *The normal membrane potential of frog sartorius fibers*. Journal of cellular and comparative physiology, vol. 34, p. 383-396, December 1949

[2] NEHER, E., SAKMANN, B., STEINBACH, J. H. *The extracellular patch clamp: A method for resolving currents through individual open channels in biological membranes.* Pflugers archive European journal of physiology, vol. 375, p. 219-228, 1978

[3] OGDEN, D., STANFIELD, P. *Patch clamp techniques*. Available online 14.3.2011 at : http://www.utdallas.edu/~tres/microelectrode/microelectrodes_ch04.pdf

[4] KLEMIC, K. G., KLEMIC, J. F., REED, M. A., SIGWORTH, F. J. *Micromolded PDMS planar electrode allows patch clamp electrical recordings from cells.* Biosensors and Bioelectronics, vol. 17, p. 597-604, 2002

[5] GENTET, L. J., STUART, G. J., CLEMENTS, J. D. *Direct measurement of specific membrane capacitance in neurons.* Biophysical journal, vol. 79, p. 314-320, 2000

[6] ZHANG, L., WIENER, J. L., VALIANTE, T. A., VELUMIAN, A. A., WATSON, P. L., JAHROMI, S. S., SCHERTZER, S., PENNEFATHER, P., CARLEN, P. L. *Whole-cell recording of the Ca^{2+}-dependent slow afterhyperpolarization in hippocampal neurones: effects of internally applied anions*. Pflugers archive European journal of physiology. Vol. 426, p. 247-253, 1994

[7] JONES, K. A., GARBATI, N., ZHANG, H., LARGE, CH. H. *Automated patch clamping using the Qpatch*. Methods in molecular biology, vol. 565, p. 209-223, 2009

[8] STEINMETZ, I. *New standard in electrophysiology and deep tissue imaging*. Available online 14.3.2011at: http://www.leica-microsystems.com/press-media/newsletters/research-resolution/march-2009-test/new-standard-in-electrophysiology-and-deep-tissue-imaging/

Transcom 2011, 27-29 June 2011
University of Žilina, Žilina, Slovak Republic

FEM Analysis of Linear Switched Reluctance Machine

[*]Pavol Rafajdus, [*]Peter Sekerak, [*]Lukas Kalamen, [**]Xing Wang, [*]Valeria Hrabovcova,
[*]University of Žilina, Faculty of Electrical Engineering, Department of Power Electrical Systems, Univerzitná 1, 01026 Žilina, Slovakia, pavol.rafajdus@kves.uniza.sk
[**]China University of Mining and Technology, School of Information and Electrical Engineering, Xuzhou 221116, China, wxstarwx@163.com

Abstract. This paper deals with parameters investigation of Linear Switched Reluctance Machine (LSRM) by means of Finite Element Method (FEM). The analysis is carried out on the basis of input geometrical dimensions and materials of the real LSRM. The calculation of the LSRM static parameters such as phase inductance, flux linkage and force versus phase current and position were carried out.

Keywords: linear switched reluctance machine, finite element method, static parameters.

1. Introduction

An optimization of electrical machines design is an actual task from the point of view of input electrical energy consumption (motoring mode) and production of electrical energy (generating mode) [1]. The main aim of the optimization is to increase efficiency of electrical machines and to decrease losses. The efficiency optimization of electrical machines can be carried out during their design. There are several methods for the design process, mainly the analytical calculation [2], [3]. A very useful tool for the design of electrical machines is Finite Element Method (FEM). This method is also convenient to calculate the parameters and performance of electrical machines [4]. This paper deals with static parameters calculation of the LSRM, such as phase inductance, electromagnetic force and flux linkage, needed for a deeper analysis of its performances.

The LSRM construction is very simple. Both stator and mover have salient poles and only the stator carries winding coils, which are suitably connected to create phases. The magnetic flux is provided by phase current to develop a reluctance force [1]. This machine can operate as a motor or a generator. The three phase basic structure of LSRM is shown in the Fig. 1.

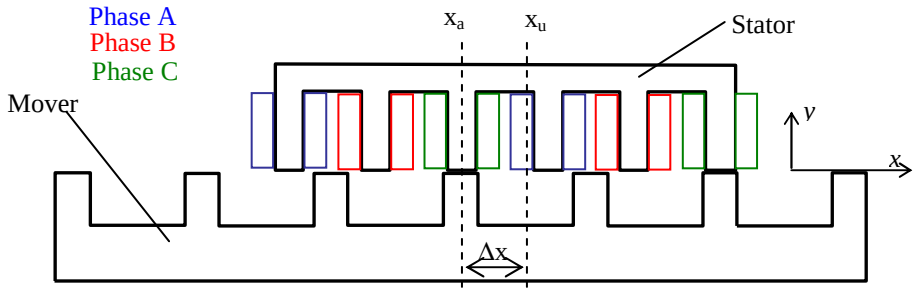

Fig. 1. The three phase LSRM

This paper is made in cooperation between the University of Žilina and the China university of Mining and Technology in Xuzhou, China, where the LSRM was developed and manufactured. In the future, this LSRM will be optimized from the point of view of power density and volume. In the Fig. 2 there is shown a real prototype of the LSRM where the moving and static parts are separated for illustration. The LSRM from the Fig. 2 is analyzed by means of FEM, especially with the FEMM 4.2 software using planar 2D system. The static parameters mentioned above have been calculated for different phase current and mover position.

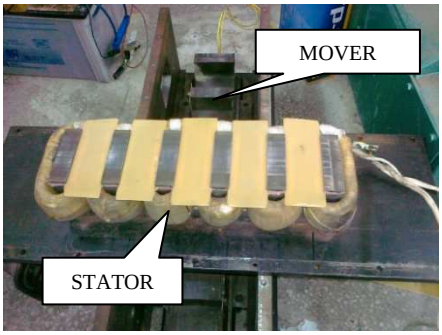

Fig. 2. The three phase LSRM prototype with separated stator and mover

2. FEM Analysis of the LSRM

For the FEM magnetostatic analysis the following input data are necessary: geometrical dimensions of the machine, current density of one phase, material constants (winding conductivity and relative permeability, B-H curve of LSRM ferromagnetic circuit material) and boundary conditions. The parametric model of LSRM has been created in LUA script in the FEMM 4.2 software for more convenient calculation with lower time consumption. The LUA script also enables the LSRM model optimization (changes of the geometry of the machine) during the execution of the script.

The accuracy of the result depends on the size of FEM mesh and accuracy of the input parameters. In our model, 17.000 nodes have been used. The calculation was carried out for each individual mover position and current under static condition. The mover position x was moved from aligned x_a to unaligned position x_u with step of 0.5 mm and in each position the current was changed within its working range from 1 to 35A. In the Fig. 3a the distribution of magnetic flux lines of LSRM for aligned position can be seen, in the Fig.3b for unaligned mover position. The phase current was kept constant 10A.

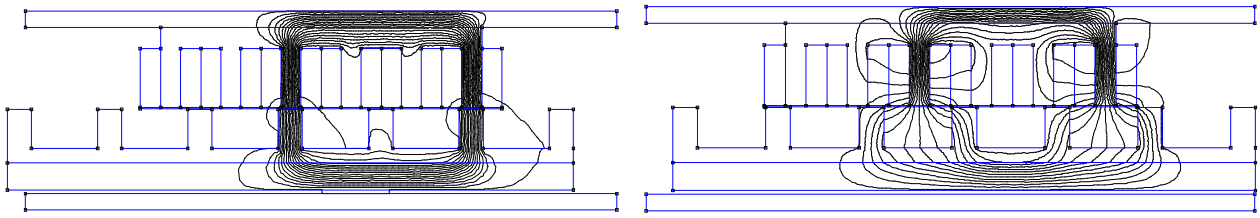

a) b)

Fig. 3. The distribution of magnetic flux in the LSRM for phase current 10 A, a) aligned mover position, b) unaligned mover position

The static parameters of LSRM are very important for its design, dynamic simulations, losses and efficiency calculations. We will deal with these issues in the future to improve some LSRM performances and parameters.

2.1. Magnetic flux linkage calculation

The first parameter which has been analyzed is the flux linkage versus phase current for different mover position $\psi = f(I,x)$. The area bounded by maximal phase current and by both ψ-I curves for aligned and unaligned position is equal to mechanical energy, which is converted to electromagnetic force [1]. In the Fig. 4 can be seen the curves obtained by means of FEM for different phase currents and mover positions.

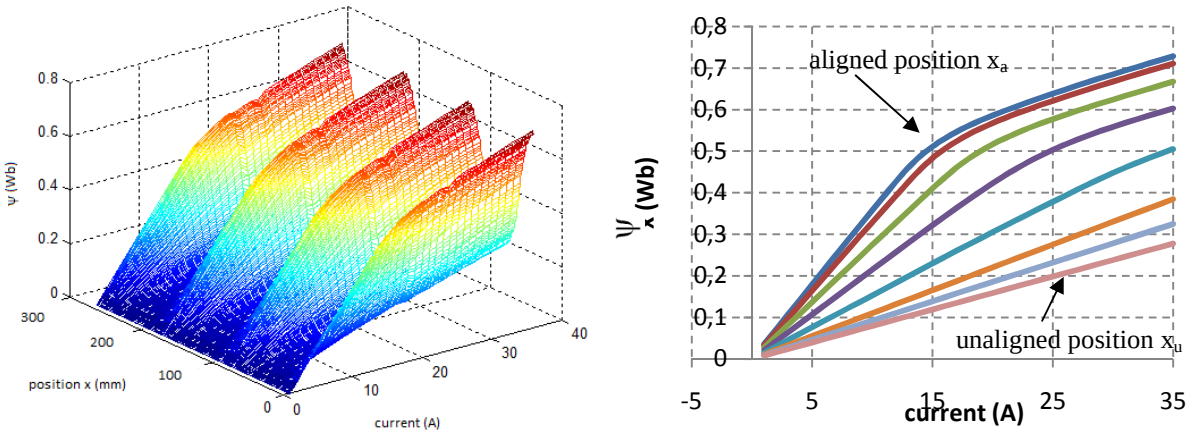

a) b)

Fig. 4. The flux linkage curves for different phase currents and mover positions: a) 3D view, b) 2D view.

2.2. Phase inductance calculation

The phase inductance L=f(I,x) versus mover position for full current range is a static parameter which is needed in LSRM mathematical model for dynamic simulations. The analysis was made for the whole working range. The phase inductance profiles are shown in the Fig. 5. Presented analysis neglects end effects.The origin of the position axis is set to aligned position and the inductance decreases its value for each phase current until the mover and stator are not in unaligned position (Fig 5b). The results are obtained by means of FEM for LSRM in accordance with the following equation:

$$L = \frac{\int A \cdot J dV}{I^2}. \qquad (1)$$

where A is magnetic vector potential, J is current density, V is volume and I is phase current.

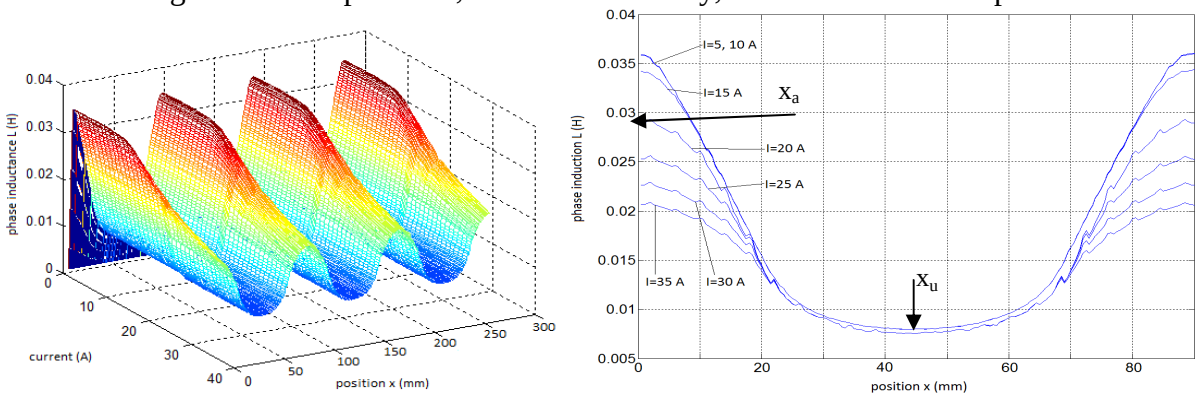

a) b)

Fig. 5. The phase inductance for different phase currents and mover positions: a) 3D view, b) 2D view

2.3. Electromagnetic force calculation

The electromagnetic force was also calculated by means of FEM. The static force characteristics were obtained for the whole working range. Maxwell's stress tensor prescribes the force per unit area produced by the magnetic field on a surface. The differential force produced is:

$$dF = \frac{1}{2}\left(H(B \cdot n) + B(H \cdot n) - (H \cdot B)n\right). \qquad (2)$$

where n denotes the direction normal to the surface at the point of interest, B is flux density and H is intensity of magnetic field.

The calculated values of electromagnetic force in x direction are shown in the Fig. 6a. For more complex analysis the average force F_{av} is necessary to be known. So the average force is given as:

$$F_{av} = \frac{1}{\Delta x} \int_{x_a}^{x_u} F dx \,. \tag{3}$$

where Δx is defined as $\Delta x = x_a - x_u$ and it is difference between aligned mover position x_a and unaligned mover position x_u. In this case the difference is 45 mm. The phase current was kept constant I=5,10,15, 20, 25, 30, 35 and average electromagnetic force for LSRM is shown in the Fig. 6b, calculated for interval Δx.

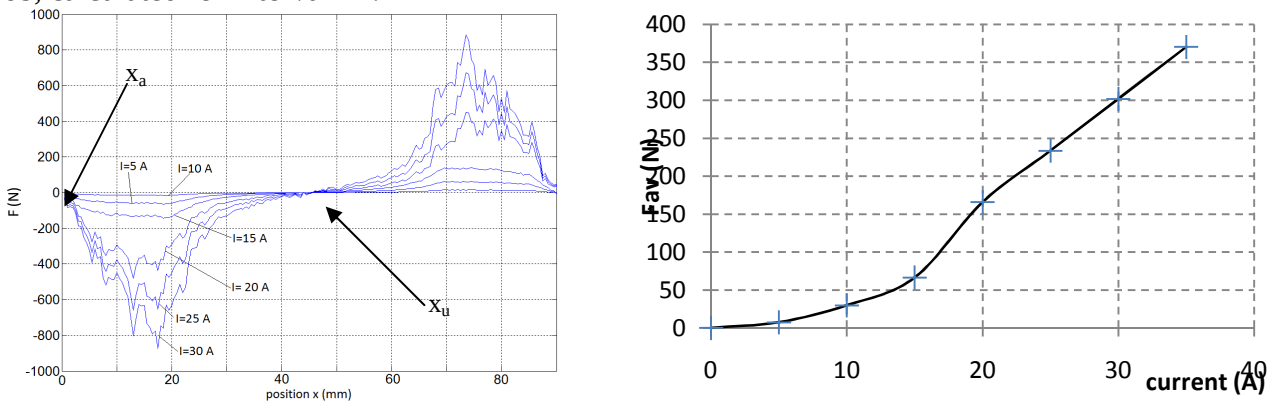

a) b)

Fig. 6. The LSRM electromagnetic force: a) static curves, b) average forces

3. Conclusion

The static parameters of the LSRM were investigated by means of FEM. Flux linkage, phase inductance and force of the machine were calculated for each mover position and phase current. The average force of the machine at the nominal current 25 A is 235 N. The investigated parameters will be compared with measurement in a future work. It is obvious that there are still some imperfections in the machine design and hence our future effort will be set on the efficiency improvement of the LSRM.

Acknowledgement

This work was supported by the Slovak Research and Development Agency under the Contract No. SK-CN-0020-09 and by VEGA (Scientific Grant Agency of the Slovak Republic) No. 1/0809/10

References

[1] MILLER, T. J. E.: *Switched Reluctance Motors and their Control*. Magna Physics Publishing, Oxford 1993

[2] BYEONG-SEOK LEE; HAN-KYUNG BAE; VIJAYRAGHAVAN, P.; KRISHNAN, R.: *Design of a linear switched reluctance machine*, Industry Applications, IEEE Transactions on Volume: 36, 2000 , pp: 1571 – 1580

[3] CHEN, H.; WANG, X.; GU, J.J.; LU, S.: *Design of bilateral Switched Reluctance linear generator*, Electric Power and Energy Conference (EPEC), 2010 IEEE, 2010 , Page(s): 1 – 5

[4] KRISHNAN, R.: *Switched Reluctance Motor Drives – Modelling, Simulation, Analysis, Design, and Applications*, CRC Press LLC, FLA, USA, 2000.

[5] CHEN, H.; ZHANG. CH.; ZHAO, X.: *Research on the Switched Reluctance Wind Generator System* // IEEE International Conference on Systems, Man, and Cybernetics, Tucson, 2001.

[6] **RAFAJDUS, P., HRABOVCOVÁ, V., HUDÁK, P.:** *Investigation of Losses and Efficiency in Switched Reluctance Motor* // 12th International Power Electronics and Motion Control Conference, EPE-PEMC 2006, Portorož, Slovenia, 2006, 08, pp.: T4-309

[7] PYRHONEN, J.; JOKINEN, T.; HRABOVCOVA, V.: *Design of rotating electrical machines*, John Wiley & Sons, 2008,

Transcom 2011, 27-29 June 2011
University of Žilina, Žilina, Slovak Republic

Real -Time Communication Between Programmable Logic Controller

[*] Andrej Rybovič, [**]Anna Bystričanová
[*] University of Žilina, Faculty of Electrical Engineering, Department of Mechatronics and Electronics, Univerzitná 1, 01026 Žilina, Slovakia, andrej.rybovic@fel.uniza.sk
[**] University of Žilina, Faculty of Electrical Engineering, Department of Mechatronics and Electronics, Univerzitná 1, 01026 Žilina, Slovakia, anna.bystricanova@siemens.com

Abstract. The aim of the present paper is to assess and experimental evidence in which tolerances varies of response between remote PLC at the process level through industrial network of controllers PLC . For the experiments we have chosen PLC from the manufacturer Siemens with communication via Industrial Ethernet.

Keywords: programmable logic controller, systems blocks, industrial ethernet

1. Introduction

Programmable logic controller (PLC) which has the advantages of high reliability, design flexibility, simple programming and higher cost performance has been widely applied in the industrial control field [1]. In small applications where suffices to control the one programmable logic controller the communication is not critical and is guaranteed by the manufacturer PLC with minimal response. Task of the communication is both mediate communication with the normal PC in order to create and transfer between the PLC and PC, and also transmit data to the master levels for operator control technology.

2. Management of PLC

For the direct control of the only PLC is possible to rely on the manufacturer prescribed reaction between the input and corresponding of output shown on Fig. 1a. This response is around 10 ms depending on the memory size, processor speed respectively longest time programming recurrent cycle (scan) of the processor. In compiling the distributed control system for managing large-scale industrial applications is always very important to address the issue of communication. There appears sometimes a requirement to control the output of the remote PLC accessible only through an industrial communication network shown on Fig.1b. Response in this case will be greater and will depend on many factors. Industrial networks provide on the procedural level particular control of the production process therefore require high reliability, deterministic mode of communication and high performance. On the other side, they allow connection with a centralized operator level (PC with SCADA / MES function) of the whole enterprise information system with top ERP system.

Conventional corporate (Proprietary) industrial networks use from the standard reference communications model (RM-OSI) only three layers - physical, line and applications (examples are protocols CAN, Profibus, DeviceNet and others). Modern networks based on the Industrial Ethernet (IE) technology TCP / IP uses five layers, where to physical and link layer adds transport and network layer to support TCP / IP [2]. Industrial Ethernet is the applications of IEEE 802.3 standards with requirements of factory equipment and network protocols [3]. Management of connections between remote PLC performs link layer with the use of transmission in real time, its most important function is addressing individual PLC´s nodes on the bus.

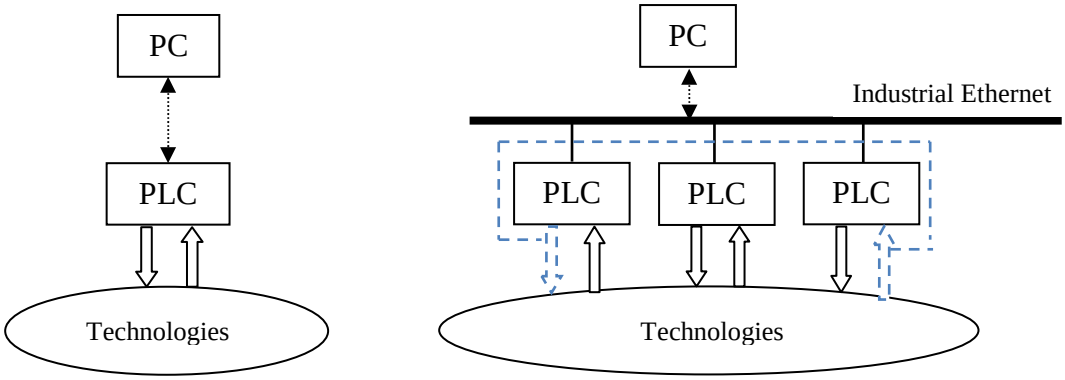

Fig. 1. Management of PLC: a) direct, b) through industrial communication network

3. PLC Configuration

If PLCs want to communicate in common industrial network, they must use the same communication protocol. It is actually a summary of the parameters and rules governing communication. Selection of the communication protocol is subject to network selection.

For practical verification of communication among the various PLC we used the communication model consisting of parts:

Hardware: Simatic S7-300 (CPU 315-2 PN/DP)
Simatic S7-300 (IM 151-8 PN/DP)
Software: Step 7 S7/M7/C7 (Version V5.4 + SP5 + HF1)
Network: Ethernet
Protocol: S7 communication (with system blocks BSEND, BRCV)

3.1. Mutual communication between PLC

After programmed systems blocks and after follow filling CPU both PLCs programmed blocks we can convince the running of communication between two PLCs. Block BSEND sends data to another PLC, where block BRCV accepts them. Setting system blocks can be seen from the figure below.

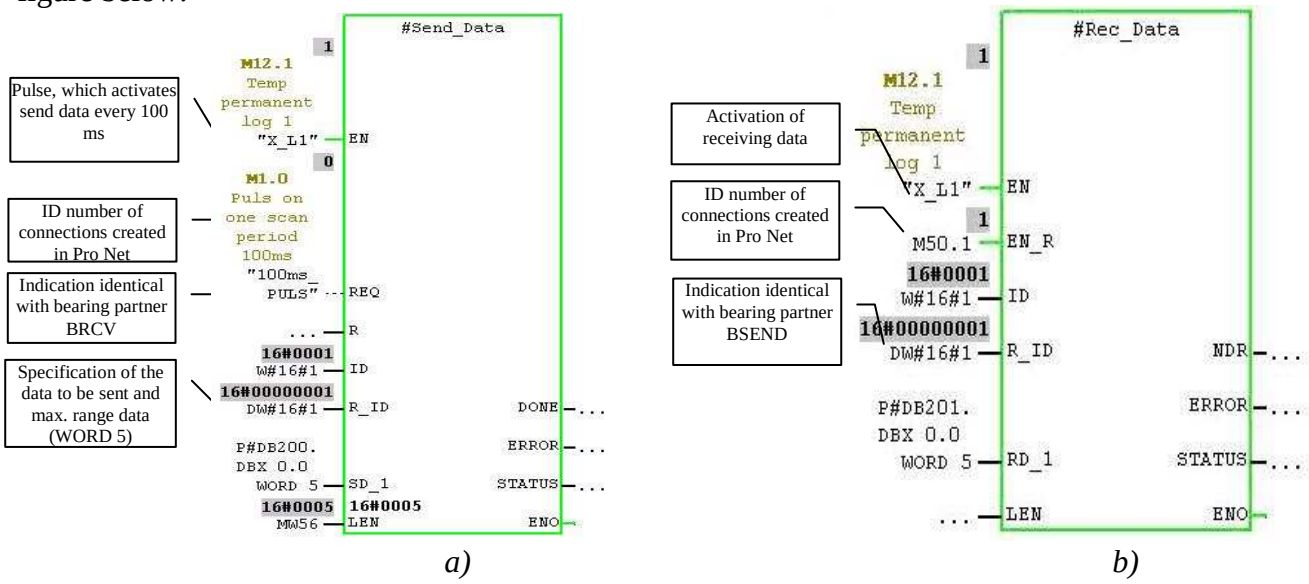

Fig. 2. Systems blocks: a) SFB 12 BSEND, b) SFB 13 BRCV

Data sent from the DB 200 by BSEND functions of PLC have been taken by another PLC by BRCV functions to DB 201. Data will be able to send and receive after each elementary types (bit, byte, word, int, real,...), or whole data fields (array,..) [4].

4. Experimental results

For experimental verification we linked two PLC automatons via Ethernet. For this idealized (channel without interference by other nodes and without industrial interference) configuration we observed for one minute cycles of data transmitted between PLCs:

1. resizing pulse parameter REQ block of BSEND,
2. change in volume of transmitted data.

From transmitted data block we observed one bit, which state (0,1) is changed each time you make cycle of data transfer for one minute. We used counter C1, which counted a state variable 1 and counter C2, which counted state for variable 0.

We detected that for size of transmitted data 10B and time100 ms the variable impulse in parameter REQ into block BSEND in both PLC was carried out 578 cycles of data communication over one minute for time scan of CPU 1 and CPU 2 (Fig. 3 a). The same experiment we conducted for 1s impulse in parameter REQ in block BSEND (Fig. 3 b). In this case, the number of cycles between two PLC during 1 minute fell to 60. This means that for 10 - fold reduction of frequency data communication between two systems blocks both PLC is also number of cycles carried out the data transmission decreased almost 10 fold. A marked change of both CPU times scan was not recorded.

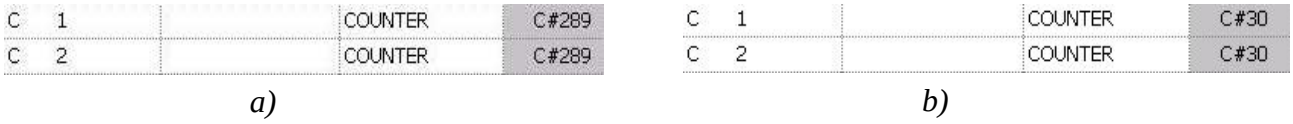

a) *b)*

Fig. 3. Counters cycles transferred data size of: a) 10 B and 100ms impulse, b) 10 B and 1s impulse

This time we increase the volume of communicated data to the maximum i.e. 32 kB. For pulses lasting 100 ms to during 1 minute transmission took place 338 times (Fig. 4a). Again kept previously mentioned times scan both CPU. We tried to reduce the frequency of transmission. Into REQ parameter of block BSEND both PLC we joined 1s pulse, which initializes sending data from one PLC to another. In this case the transmission carried out only 26 times (Fig. 4b).

a) *b)*

Fig. 4. Counters cycles transferred data size of: a) 32 kB and 100ms impulse, b) 32 kB and 1s impulse

For these experiments results that scan time of both processor significantly does not change either for condensed frequency transmission, either for larger volume data communicated. It means that tested data communication ran reliably and particularly without processors encumbrance in both logic controllers.

5. Conclusions

A practical example was demonstrated one of the ways of data communication between multiple PLCs. We chose a model where both processors are a type of SIMATIC. We chose IE network with the service S7 communication. System blocks SFB 12 and SFB 13 BSEND BRCV have been used to transfer data, which are capable of transmitting a maximum of 32 kB of data for S7-300 and 64 kB for S7-400.

As mentioned earlier and experimentally verified, speed data communications among multiple PLCs depends primarily on the used hardware (CPU type), industrial networks, for which takes place transfer date and parameter settings of systems blocks including the size of data transferred. In the future we expect verification of communication between PLCs from other manufacturers as Allen-Bradley, Schneider Electric, etc., namely using the channel with industrial interference.

Acknowledgement

The authors wish to thank for support to R&D operational program VEGA Agency for the project No. 1/0470/09

References

[1] XIUHAN J., *Principle and Application of PC* , 3rd ed.XiDian University Press,2003,pp.1-50GUPTA, K. C.,

[2] FRANEKOVÁ M., KÁLLAY F.; PENIAK P., VESTENICKÝ P.: *Komunikačná bezpečnosť priemyselných sietí*. Žilina 2007. ISBN 9078-80-8070-715-6

[3] MARSHALL P.,S., RINALDI J., S., *Industrial Ethernet: How to Plan, Install and Maintain TCP/IP Ethernet Networks, The Basic Reference Guide for Automation and Process Control Engineers, 2nd Edition*. United States of America: ISA-The Instrumentation, Systems and Automations Society, 2005.

[4] SIEMENS AG. *Help on Simatic Manager V5.4+SP5+HF1*. Siemens AG, 1995-2009

Transcom 2011, 27-29 June 2011
University of Žilina, Žilina, Slovak Republic

Demand Side Management (DSM) as an element of the energy efficiency

[*]Rafal Sobota
University of Częstochowa, Faculty of Electroenergetic, Electrical Department, Armii Krajowej 17, 42-200 Częstochowa, Poland, {szkutnik, rsobota}@el.pcz.czest.pl

Abstract: This article presents the problem of the development of management strategies demand for electricity. An important role of "DSM" is to maintain energy supplies to individual customers at the required level. This involves appropriate planning, execution, monitoring and analysis of various elements of the manufacturing sector and electricity distribution equipment and work with each end consumer. In addition, the article raises the issue of energy efficiency of the country, ways of its realization and implementation.

Keywords: power, strategy, DSM, demand side management, energy efficiency.

1. Introduction

We all want the convenience of using electricity. However, we do not realize that the supply of energy to our homes is a complex process, which uses hundreds of miles of wires and complicated equipment.

In the past, the main objective of most strategy of Demand Side Management (DSM) was to provide energy and power, so as to defer the need to build new sources of energy, including production facilities, purchase of additional power, its transmission and distribution. However, due to changes in the energy sector, electrical equipment are supported through programs "DSM" in order to improve relations with a potential consumer and obtaining the key information to improve the functioning of the system. "DSM" refers to the energy and charges affecting the shape of the action taken in response to new readings of the electrical equipment.

"Demand-side management (DSM) consists of planning, implementation and monitoring of electrical appliances that are designed to encourage consumers to change their level and structure of electricity consumption. It is a complex process in which planning, implementation and monitoring of electricity use by the consumer, depends on the available energy levels in the grid.

The main objective of Demand Side Management is to maintain the liquidity supply of electricity to consumers in relation to their energy needs, to avoid overloading the whole energy system. To achieve this aim the flow of electricity is constant, and therefore the most effective.

"DSM" refers to "actions taken by the consumer side of the meter to change the amount or timing of energy consumption through it, depending on the amount of energy produced by the plant.

2. Management strategies for a country DSM

Demand Side Management is essential for promoting energy efficiency because of the country: it decreases the demand on the electricity network, it delays the need to build additional power plants that would complement the growing demand for power by consumers, provides lower electricity costs, creates the possibility of new projects for energy producers.

Use of electricity by using effective strategies for "DSM"is one of the keys to improving our environment. Managing demand for electricity, in fact, means that less electricity to be generated. It uses a more reliable method of energy supply, greenhouse gas emissions be reduced, increasing the

protection of non-renewable resources, reduced environmental emissions, and increasing water savings in power. Demand Side Management supports solid, reliable supply of electricity.

Currently, many programs "DSM" offers a wide range of measures that can reduce energy consumption and its costs, and maximize end-use efficiency to avoid or delay construction of new power plants. These include:

- Reducing peak power consumption by the customers,
- Reducing overall energy demand,
- Increase the reliability of the power grid,
- To increase network efficiency,
- Increasing the efficiency of generating units,
- Managing the costs of electricity,
- Manage system loading,
- Efficient distribution of energy,
- Refit the fuel.

Energy Efficiency Plan and its effective use is becoming a national priority and a necessity for the future development of the country's economy. Many essential elements of the strategy of "DSM" is reflected in increasing the energy efficiency of state, including:

- Act, short-, medium-and long-term energy efficiency, which will support the economic development of the country.
- Creating a national consciousness that electricity is a precious commodity, which is to be applied universally.
- Promoting energy efficiency through legislation aimed at: preventing the use of inefficient equipment, to achieve high energy efficiency in its entirety with the natural resources used for electricity generation, the establishment of mechanisms for financing energy efficiency projects, ensuring adequate funding for energy efficiency projects of the country.
- Implementation of selected major projects to increase efficiency and reduce the efficiency of the country.
- Use of alternative sources of energy for heating.

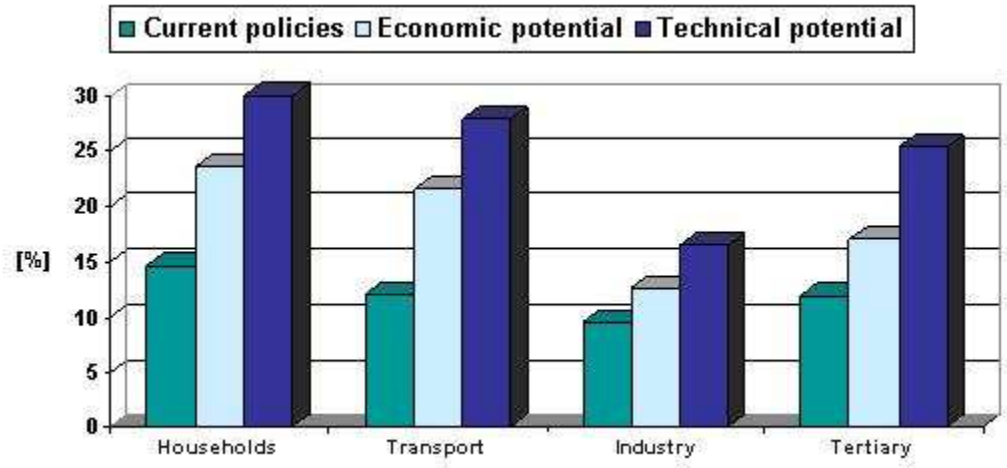

Fig. 1. Final energy savings in EU27 in 2020.Source: EU Policy and Legislation

3. National consciousness as an important factor to improve energy efficiency

Electricity consumers generally, whether it is trade, industry or households, play a key role in achieving energy efficiency. Looking at how energy is used, you can take steps to save energy by using efficient devices such as smart.

Achieving energy efficiency in homes is very simple. Apply a few basic steps you can take to save electricity. First look at the house and you can make sure all the air gaps are closed, the insulation is installed in the ceiling, and whether the house is made of suitable materials. Using everyday objects associated with the fundamental principle - "if you're not using, disable it. " Disabling saves money. Do not leave your TV, DVD player and other devices in standby mode. It is recommended that you use compact fluorescent lamps (CFL's) instead of incandescent bulbs. In addition, room temperature must be within the range from 18 ° C to 22 º C.

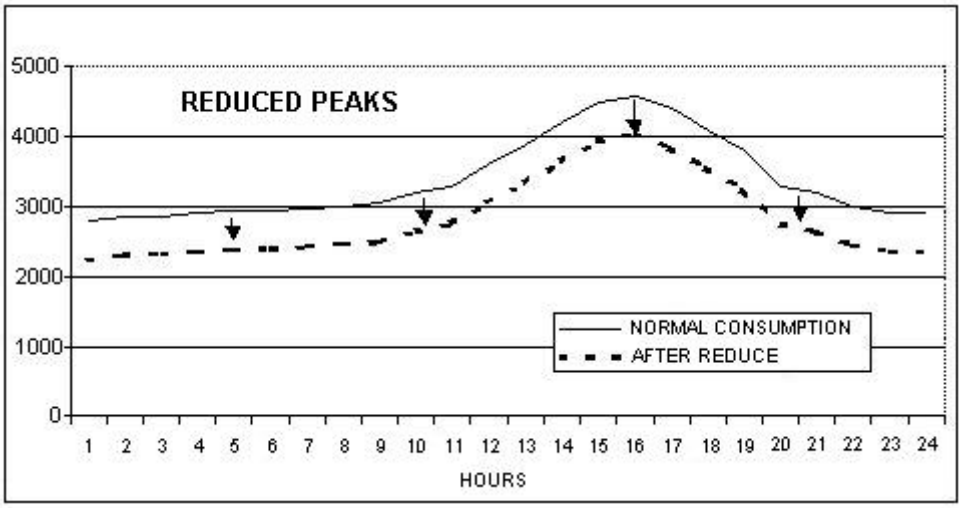

Fig. 2. The basic assumption of demand side management to improve energy efficiency.
Source: Own

Energy efficiency in thousands of offices and businesses can be achieved through energy conservation by the way in which business is carried on. In addition, managers of companies should ask themselves these questions:
- How much electricity is currently using the company?
- How much activity per month?
- What are the best ways to save energy in your daily business?
- How can savings plans to include the company's strategic plan to raise general awareness in the company?

Energy efficiency starts with good design of the building. Please check that the automatic doors and air curtains is correct. Cracks windows conducive conditioned air from escaping. In areas that have high levels of natural light, you should consider disabling electric lights. Is recommended to replace incandescent bulbs for compact fluorescent lamps. If there is an adequate flow of air in the building will be enforced on the equipment to work harder by heating, ventilation and air conditioning to achieve the desired temperature. It is important to install a building management system that automatically turn on and off lights, heating, ventilation and air conditioning.

Another essential factor is to maximize energy efficiency in electricity use in industrial facilities, particularly those that extensive use of electric motors. These units are the main consumers of electricity. Promoting and implementing energy efficiency programs, establishment and participation of workers is the first, yet most important step towards achieving substantial energy savings. Switching to energy-efficient engines, increase oversight of motor control will maximize the benefits. Turn off appliances that are not being used, helping to reduce energy and maintenance costs.

Agriculture is also an important area for action to improve energy efficiency of the country. By making small changes in the way the energy can be ensured of the highest quality products at low cost. For example, using irrigation, remember to properly fit the pipe and nozzles. Small-

diameter tubes operate at a higher level of friction. More electricity is needed to increase the rate of water supply and to overcome friction. Sprayer nozzles should be checked on a regular basis. You can also reduce water losses arising due to leaking pipes. Leaking pipe the result that the pump must provide more water, which increases energy consumption. By conducting regular maintenance can reduce energy costs and increase water conservation. In addition, you can use gravity flow, even when the supply power is not available, thereby saving energy for power pumps.

4. Conclusion

Demand Side Management defines the process of energy management in order to optimize available and planned its resources. "DSM" is trying to influence the way which industry, trade and individual customers consume electricity. The flagship goal is to help customers manage their energy consumption, particularly during peak periods, resulting in cost savings. DSM is mainly on improving the energy efficiency of the country and implementation of load management projects.

Electricity consumption will grow two times faster than the overall final energy consumption. Provides a substantial increase in worldwide electricity production in spite of the growth of consumption in developed countries. It is expected doubling of global electricity generation of 116 TWh in 1990 to 230 TWh in 2020. Generally, a significant increase in the share of electricity in total energy consumption. This increase will apply to a greater or lesser extent, all countries which highlights the importance of this sector and the need for its frequent updating. This also applies to the situation of Polish.

References:

[1]. Berełkowski P.: *„Sterowanie popytem na energię elektryczną w spółce dystrybucyjnej”* – Prace naukowe Instytutu Elektroenergetyki Politechniki Wrocławskiej nr 91 – Seria konferencje nr 34.

[2]. Jahnatek L., Szkutnik J.: *„The methodology of benchmarking in development of electricity distribution company”* – Przegląd elektrotechniczny 3’2009 – Wydawnictwo SIGMA-NOT Sp. Z o.o. – Warszawa 2009.

[3]. Nazarko J., Jurczyk A.: *„Wykorzystanie naturalnych preferencji klientów przy wdrażaniu programów DSM”* – Prace naukowe Instytutu Elektroenergetyki Politechniki Wrocławskiej nr 91 – Seria konferencje nr 34.

[4]. Tuma J., Martinek Z.: *„Security, quality and realiability of electrical energy”* – Wydawnictwo CONTE spol. S.r.o. CVUT Praha – Praga 2007.

[5]. Szkutnik J.: *„Współczesne problemy energetyki europejskiej”* – Efektywność w sektorze dystrybucji energii elektrycznej – Aspekty techniczne – Pod redakcją Anny Gawlak – Wydawnictwo TEKST sp. Z o.o. – Częstochowa 2009.

[6]. Szkutnik J.: *„Wpływ strategii DSM na sprawność i efektywność rozdziału energii elektrycznej w sieciach rozdzielczych spółki dystrybucyjnej.”*- Aktualne problemy w elektroenergetyce, IX Międzynarodowa Konferencja Naukowa. Tom V. Oficyna Wydawnicza Politechniki Gdańskiej, Gdańsk-Jurata, 1999.

[7]. Szkutnik J. : *„Wpływ strategii sterowania popytem na koszty rozdziału energii elektrycznej w spółce dystrybucyjnej*.” - Sieci elektroenergetyczne w przemyśle i energetyce. Sieci 2000, IV Konferencja naukowo-techniczna. Tom I. Oficyna Wydawnicza Politechniki Wrocławskiej, Wrocław, 2000.

[8]. Szkutnik J.: *„Smart metering jako decydujące uwarunkowanie wdrożenia strategii DSM w Polsce”* – Rynek Energii 1’2010 – Wydawnictwo KAPRINT – Lublin 2010.

[9]. http://ec.europa.eu

Transcom 2011, 27-29 June 2011
University of Žilina, Žilina, Slovak Republic

Harmonic reduction techniques using Multi-Pulse Rectifiers

*Paweł Stawczyk
*Kielce University of Technology, Faculty of Mechatronics and machine building, Al. Tysiąclecia Państwa Polskiego 7, 25-314 Kielce, Poland, pawel83ck@o2.pl

Abstract. AC/DC converters generate into the power system high harmonic currents and voltages, which causes a deformation of their shapes and increases active power losses. These article gives short review about basic methods of reduction higher harmonics in phase currents of AC /DC converters consisting of parallel connected 6-pulse bridges.

Keywords: AC/DC converter, power quality, *THD* (Total Harmonic Distortion), autotransformer.

1. Introduction

In recent years, the harmonics in the power system appear due to the widely applications of the electronic equipments in which the AC/DC converter are usually used. Therefore, it is very important to reduce harmonic components in supply currents of the AC/DC converters. The harmonic problems can be solved by using the active filters which usually operate at high switching frequency and are not suitable for high power applications. The power factor and total harmonic current distortion THD_i of the input line current can be improved by using of the multi-pulse AC/DC converter. The total harmonic current distortion THD_i is described by formula:

$$THD_i = \frac{\sqrt{\sum_{h=2}^{\infty} I_h^2}}{I_1} 100\% = \sqrt{\sum_{h=2}^{\infty} I_h^{*2}} \,. \tag{1}$$

where: I_h^* - relative current component of *h*- harmonic order

Multi-pulse AC/DC converters generate odd current harmonics order:

$$h = k \cdot q \pm 1 \,. \tag{2}$$

where *k*- number of parallel connected 6-pulse bridges, *q*- number of pulses

As results from (2) an increase in pulse number *q* is the basic method to eliminate high harmonic currents. One obtains an increase in *q* in classical solutions by series or parallel connection of *p* number of 3-phase bridges supplied by transformers with required phase shifting.

$$\phi = \frac{2\pi}{q\ p} \,. \tag{3}$$

Another method consists in the use of rectifiers with modulators in DC current circuits.

2. Multi-pulse AC/DC rectifiers

Fig. 1. shows modified systems consist of 6-pulse rectifiers they behave approximately as 24-pulse (Fig. 1a) and 36-pulse (Fig. 1b) rectifiers in consequence of alternate conducting of diodes and thyritors connecting to terminals of the interphase transformer. The depth of asymmetry

in load of each of component rectifiers depends of turn number of reactor segments in consequence improve the power quality.

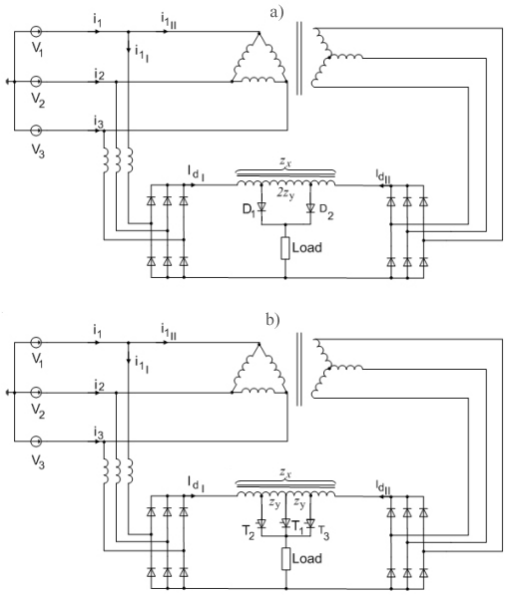

Fig. 1. Diode rectifiers with modulation in DC current: a) 24- pulse, b) 36- pulse [4]

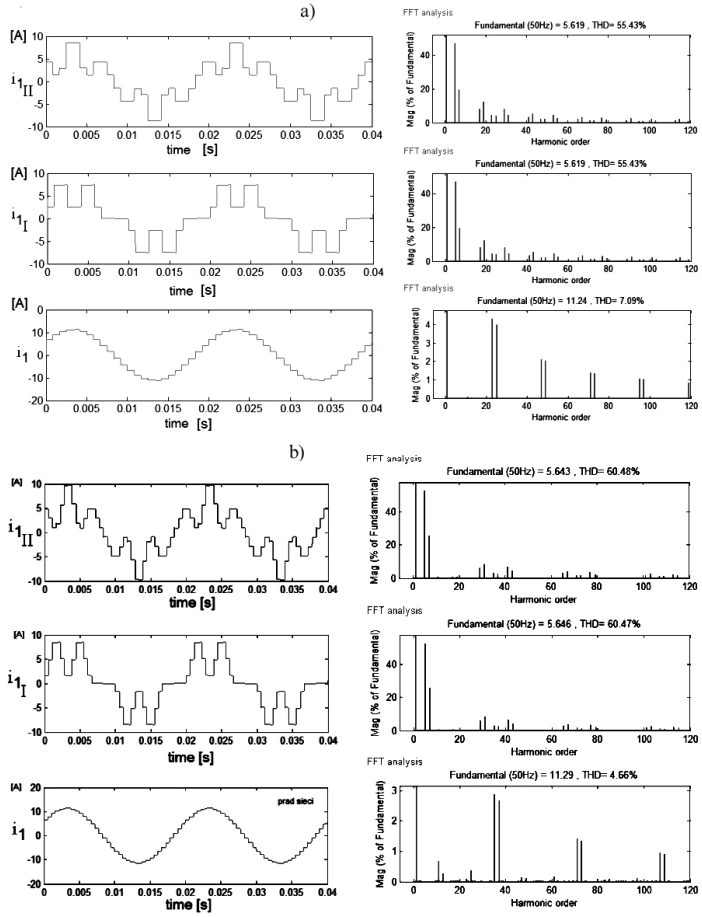

Fig. 2. Line currents of component bridges and rectifier and their *FFT* analysis in: a) 24- pulse, b) 36- pulse mode [1, 3]

The 36- pulse rectifier offers a higher quality input current (line current) while that of the 24- pulse rectifier is distorted. The *THD* of the 24- pulse rectifier equals 7.09% but for 36- pulse rectifier 4.66%.

Another type of modulation in DC current circuit in the form of interphase transformer is presented in Fig. 3 [7]. Primary winding of the transformer is supplied from AC current modulator. The shape and magnitude of AC current transformed from primary to secondary winding determines the depth of load asymmetry of rectifier component bridges.

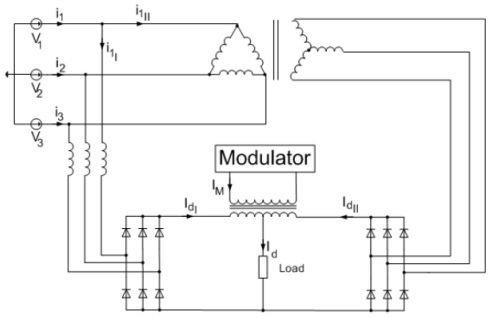

Fig. 3. 12- pulse rectifier with modulation in DC circuit [3]

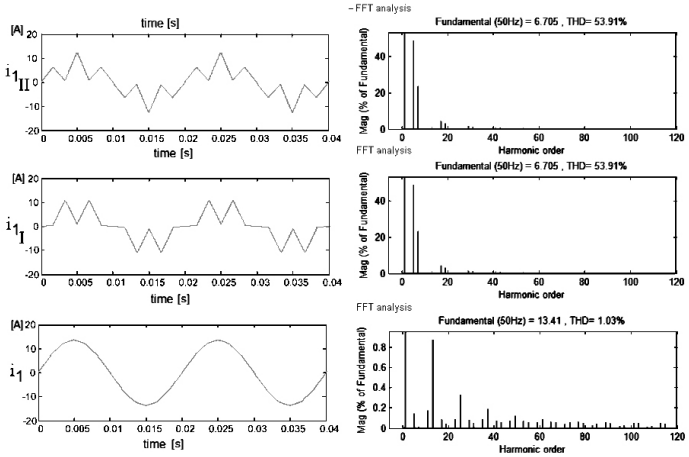

Fig. 4. Line currents of component bridges and rectifier and their *FFT* analysis [3]

The shape of line current of the converter is close to sinusoidal one. The total harmonic current distortion THD_i in this case is equal to 1.03 %.

3. Conclusion

Conventional AC/DC converters are developed using diodes and thyristors to provide controlled and uncontrolled unidirectional and bidirectional dc power, however, these converters have problems of poor power quality in terms of injected current harmonics, resultant voltage distortion and slowly varying rippled DC output at load end, low efficiency, and large size of AC an DC filters.

High-power applications use AC/DC converters based on the concept of multipulse mode (namely: 12-, 24-, 36-pulse) to reduce the harmonics in AC supply currents, to overcome presented drawbacks and to fulfil contemporary power quality standards. The variation of harmonics in the input current for different pulse numbers is shown Tab. 1.

Pulse number	*THD* [%]
6	34.5
12	14.5
24	7.09
36	4.66

Tab. 1. Variation of *THD* with pulse number

It is possible to further improve the *THD* using the modulator in the DC circuit shown in Fig. 3. The value of *THD* for this case is 1.03%, which is a very good result. Multi-pulse rectifiers with modulation in DC current circuit meets the standards specified for connecting devices I and II quality [8].

References

[1] ROLEK, J. *Układy prostowników wielopulsowych z modulacją w obwodzie prądu stałego*. Przegląd elektrotechniczny, ISSN 0033-2097, R. 84 NR 5/2008.

[2] ANRVINDAN, A, N., PUSHPAKARTHICK, P. *24- pulse rectifier realization b 3-phase to four 3-phase transformation using conventional transformer.* NPEC 2010.

[3] KAPŁON, A., ROLEK, J. *Analysis of Multipulse Rectifiers with Modulation in DC Circuit in Vector Space Approach*. 2008 13th International Power Electronics and Motion Control Conference (EPE-PEMC 2008).

[4] MIYAIRI, S., IIDA, S., NAKATA, K., MASUKAWA, S. *New Method for Reducing Harmonics Involved in Input and output of Rectifier with Interphase Transformer*. IEEE Trans. On Industry Applications, IA-22 (5), 790-797.

[5] PAICE, D ,A. *Power Electronic Converter Harmonics Multipulse Methods for Clean Power*. IEEE PRESS New York 1996.

[6] YOUNIS, M., RAHIM, N., MEKHLEF, S. *Harmonic reduction in a three-phase rectifier with sinusoidal current.* Power System Technology, 2002. PowerCon 2002. International Conference on, (pages 2251 – 2255 vol.4).

[7] STRZELECKI, R., SUPRONOWICZ, H. *Współczynnik mocy w systemach zasilania prądu przemiennego i metody jego poprawy*. Oficyna Wydawnicza Politechniki Warszawskiej, Warszawa 2000.

[8] [8] ROZPORZĄDZENIE MINISTRA GOSPODARKI z dnia 4 maja 2007 r. W sprawie szczegółowych warunków funkcjonowania systemu elektroenergetycznego (29. maj. 2007), Warszawa

Transcom 2011, 27-29 June 2011
University of Žilina, Žilina, Slovak Republic

Simulation of logarithmic analog-to-digital converter with successive approximation

*Adam Szcześniak, **Zynovij Myczuda
*Department of Mechatronics and Machine Building, University of Technology in Kielce,
Aleja Tysiąclecia Państwa Polskiego 7, Kielce PL-25-314, Poland, e-mail: adam_szczesniak@o2.pl
**Department of Mechatronics and Machine Building, University of Technology in Kielce,
Aleja Tysiąclecia Państwa Polskiego 7, Kielce PL-25-314, Poland, e-mail: z_mychuda@ukr.net

Abstract. This article is a presentation of computer analysis of the logarithmic analog-to-digital converter (LADC) with successive approximation. The method of charge accumulation has been discussed and for the chosen parameters of converter structure, the simulation with chosen capacitances of accumulative capacitors has been conducted. A criterion for choosing capacitances of accumulative capacitors has been determined. Fundamental parameters of the converter have been given.

Keywords: analog-to-digital converter, logarithm, approximation, charge, simulation, accuracy.

1. Introduction

Fast development of monitoring computer systems and digital signals of information processing favoured an appearance of a considerable number of various analog-to-digital converters (ADCs) which are an important element in assuring linking between digital signals and systems with real objects. It should be emphasized that information of object condition is mostly (over 90%) in analog form. Particular attention is given to ADC with logarithmic characteristic of conversion. Using a logarithm allows an effective solution of such important tasks as compression of a dynamic range of output signals, assuring a constant value of relative error of conversion, linearization of conversion characteristics and a significant increase of efficiency of digital processors. In logarithmic arithmetic, operations of multiplication, division or raising to a power come down to operations of adding, subtracting, multiplication or division through constant coefficients of appropriate data which are in logarithmic form.

In fig.1 the logarithmic analog-digital converter (LADC) with successive approximation is shown.

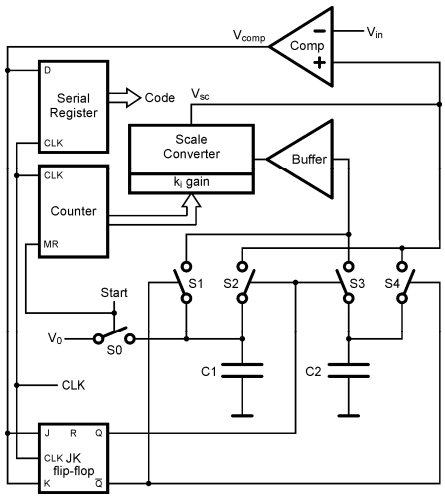

Fig.1. Logarithmic analog-to-digital converter (LADC) with successive approximation

Initially in this converter a capacitor C1 is being charged through a switch S0 to the reference voltage V0. At this time switches S1, S4 are closed and switches S2, S3 opened. The value of the initial voltage V0 being on the capacitor C1 is transferred on the scale converter (SC). The output voltage of this SC (Vsc) is compared with the input voltage Vin and the new value of voltage in accordance with the chosen transmission coefficient ki is set on a capacitor C2. Transmission coefficients ki must be different from unity. In simulated circuit they are assumed as being lower than unity. In the next tick of the clock the value of voltage VSC is compared with input voltage Vin. When the value of Vsc voltage is lower than Vin voltage a comparator is in "0" state and the next coefficient of transmission ki+1 is chosen. Then the capacitor C2 is being charged to the new value of voltage according to the set coefficient of transmission (in this case ki+1). When the voltage Vsc is higher than the measured voltage Vin then the comparator changes its state to "1" and during the next tick of the clock switches S1, S4 will be opened and switches S2, S3 closed. At the same time the value of the voltage on the capacitor C2 is being transformed on the capacitor C1. At this moment the algorithm of this method starts to repeat itself. When the comparator is in "1" state the capacitors C1 and C2 connect themselves to the SC with a change of their places. When the comparator is in "1" state capacitors C1 and C2 connect themselves to the SC with change of their places. When the comparator is in "0" state, the capacitor connection of the C1 and C2 to the SC stays the same. Voltage which was set on the capacitor connected to the input of the SC becomes transferred through the next coefficients ki until it reaches the voltage of the capacitor connected to output of the SC higher than Vin. The algorithm of converting a sample of signal lasts until ki=kn that is to take into consideration all transfer coefficients in cycle of sampled signal (for an eight bit converter n=8).

2. Simulation system of analog-to-digital converter with successive approximation

Analysis of the logarithmic analog-to-digital converter (LADC) with successive approximation was conducted using a signal circuit running from C1 capacitor to C2 capacitor (fig.2).

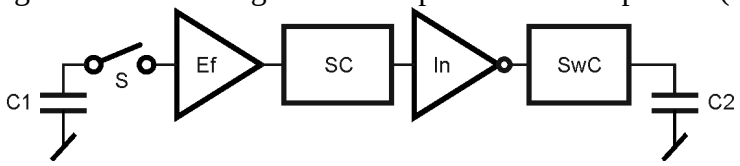

Fig.2. Converter system presenting signal circuit from C1 capacitor to C2 capacitor.

The presented system for examining the logarithmic analog-to-digital converter consists of five blocks: analog switch (S), emitter follower (Ef/Buffer), scale converter (SC) (system setting appropriate amplification lower from unity), signal inverter (In), switching circuit (SwC) (system decreasing resistance of ordinary analog switch)

It is assumed that the LADC system works with the same capacitances on input and output (C1=C2). In the simulation of the analog-to-digital converter these capacitances were chosen considerably higher than the parasitic capacitances of the system and were equal to: 0.1, 1, 10, 100 nF. For the realization of particular blocks of the converter (fig.2) switches AD4066 and operational amplifiers AD747AP were used.

Results of the simulation are presented in fig.4 - fig.7 in which for time from 0 to 1 µs the converter is switched off and in time t_0 = 1 µs becomes its switching-on. Analysis is considered for the first tick of the converter, that is when the voltage reference from C1 capacitor is equal to 10V and is transferred through the scale converter (SC) on C2 capacitor. In this analyzed tick the weight of the scale converter is set to 0.1 which sets the voltage on capacitor C2 sets on 1 V. In analyzed system parasitic capacitances of LACP (which have influence on oscillations occurring on capacitor C2) have been taken into account. Capacitance of LACP accumulative capacitors equals 0.1 nF (fig.4.) occur short lasting oscillations.

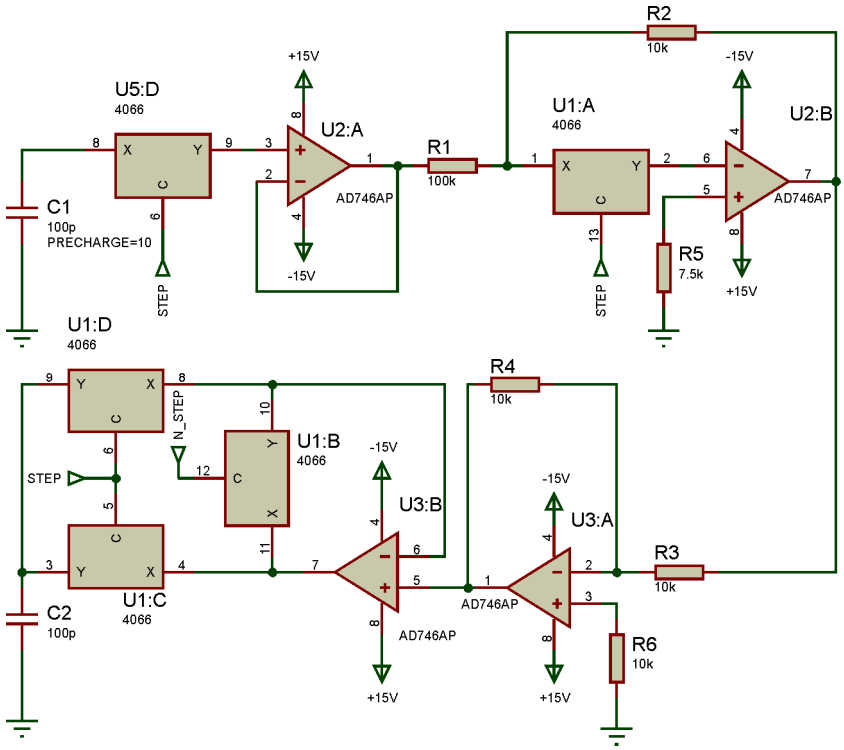

Fig.3. Simulation circuit (system diagram from the simulation software - Proteus)

It can be assumed that capacitor C2 reaches the demanded volume of 1V with accuracy of assumed error after 1.8 µs time. The highest amplitude of oscillations which occurs with load capacitance equals 1 nF (fig.5). These oscillations result from influence of parasitic capacitances of the system. It should be stated that with an increase of capacitance, the time of charging C2 capacitor increases and also the time of one tick of the converter increases. Obviously the time of one tick can be decreased to an appropriate acceptable error of the converter (fig.6). By using capacitances of accumulative capacitor equal to 10 nF, the frequency of oscillations on C2 capacitor does not have such a significant meaning as the lasting time of these oscillations. In fig.6 amplitude of impulse response for time from 8 to 14 µs has been magnified twenty times. Assuming that the scaling output voltage from C1 capacitor finishes in 11 µs then the scaled voltage on C2 capacitor will be with relative error equals $\delta = \pm 0.06$. As described above, the time of charging capacitor is particularly visible in fig.7. Time of reaching 1V voltage equals to 7 µs not counting time of lasting oscillations.

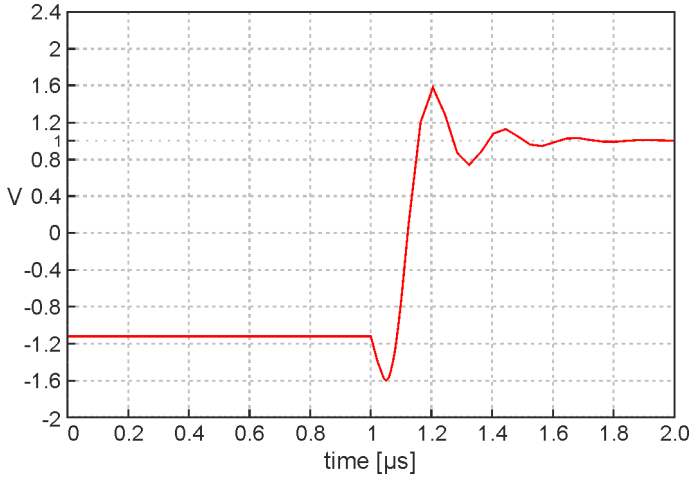

Fig.4. Voltage on C2 capacitor before and after switching-on one measuring tick of the converter for capacitances C1, C2 equal 0.1 nF

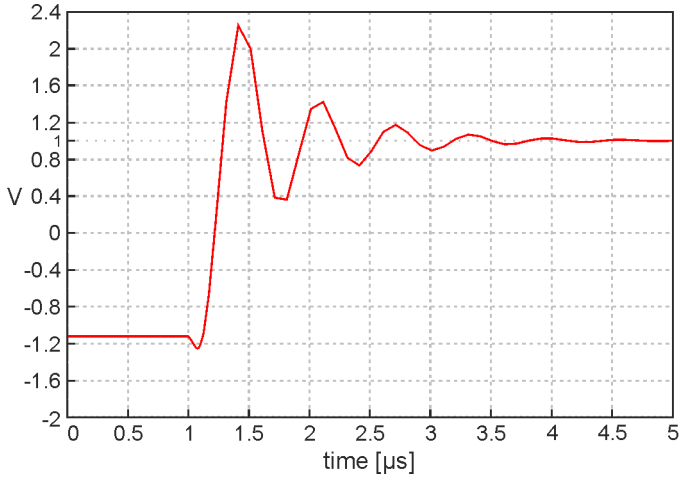

Fig.5. Voltage on C2 capacitor before and after switching-on one measuring tick of the converter for capacitances C1, C2 equal 1 nF

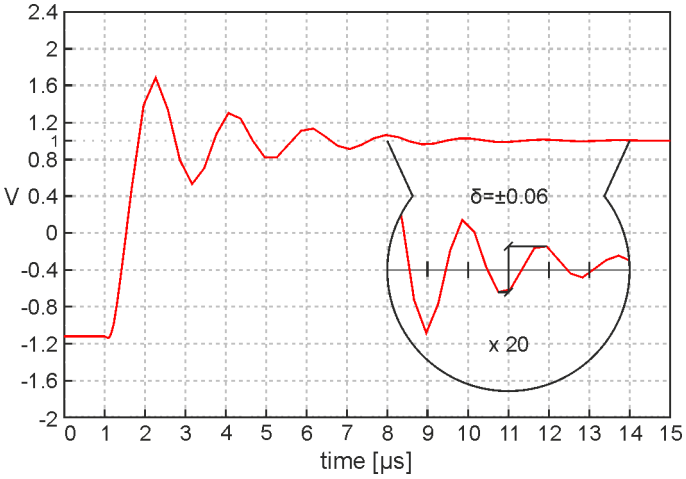

Fig.6. Voltage on C2 capacitor before and after switching-on one measuring tick of the converter for capacitances C1, C2 equal 10 nF

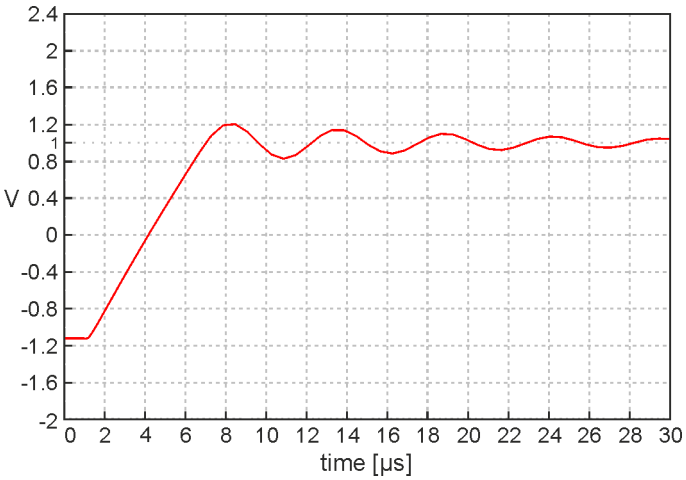

Fig.7. Voltage on C2 capacitor before and after switching-on one measuring tick of the converter for capacitances C1, C2 equal 100 nF

3. Summary

On the basis of conducted analysis of the logarithmic analog-to-digital converter it can be stated that:

On the output of LADC converter signal oscillations whose frequency depends on used parameters of system elements and accumulative capacitors C1 and C2 occur. From conducted simulation it can be stated that with increase of capacitance of accumulative capacitors (from 0.1 nF to 100nF) time of stabilizing response (time of fading signal oscillations on C2 capacitor) increase for the smaller accumulative capacitors from 0.1 nF and result in faster discharge of capacitance (lack of keeping charge) which influence the error of converter conversion.

Acknowledgement

This article is partly funded by the European Union as part of the European Social Fund entitled “Developmental Program of Didactic Potential of the University of Technology in Kielce – education for success”. Operation Program Human Capital, Agreement number UDA-POKL.04.01.01-00-175/08-00.

References

[1] Cantarano S., Pallotino G. Logarithmic Analog-to-Digital Converters: A Survey. "IEEE Transactions on Instrumentation and Measurement", Vol. IM 22, No 3, September, 1973, pp. 201-213.

[2] Guilherme J., Horta N. C., Franca J. E. Symbolic synthesis of non-linear data converters, “Electronics, Circuits and Systems, 1998 IEEE International Conference on”, Vol.3, pp. 219 – 222, 1998

[3] Greanger D.C., Heald A.B., Marlow B.K., Moore M.B. A switched-capacitor signal processing circuit for capacitive microsensors / Nat. Conf. Publ./ Inst. Eng., Austral.- 1991.- 91.-p.21-24.

[4] Lefas C.C. A serial charge redistribution logarithmic A/D converter. "Int. Journal of Circuit Theory and Applications", Vol.17, 1989, pp.47-54

[5] Lefas C.C. Successive approximation logarithmic A/D conversion using charge redistribution technigues. "Int. Journal of CircuitTheory and Applications", Vol.15, №1, 1987, pp.61-69.

[6] Myczuda Z., Szcześniak Zb. “Analiza parametrów układów elektronicznych”, Wydawnictwo - PAK 2011 ISBN 978-83-926319-3-4

[7] Szcześniak A., Myczuda Z. „Porzędowy logarytmiczny analogowo cyfrowy przetwornik”, IV international conference, Advanced Computer Systems and Networks, Design and Application, Lwów 2009, Ukraina

[8] Szcześniak A., Myczuda Z „A method of charge accumulation in the logarithmic analog-to-digital converter with a successive approximation”, Przegląd Elektrotechniczny (Electrical Review), ISSN 0033-2097, R.86 nr 10/2010 str.336-340

[9] Szcześniak A., Myczuda Z., „Przetwornik Cyfra-Analog”, Wynalazek został zgłoszony w Urzędzie Patentowym RP w dniu 8.12.2010r i zarejestrowany pod numerem P-393179 .

Transcom 2011, 27-29 June 2011
University of Žilina, Žilina, Slovak Republic

Development strategy of energy distribution in companies within the principle of investment efficiency

Jerzy Szkutnik, Rafal Sobota
University of Częstochowa, Faculty of Electroenergetic, Electrical Department, Armii Krajowej 17, 42-200 Częstochowa, Poland, {szkutnik, rsobota}@el.pcz.czest.pl

Abstract: This article presents the problem of development of medium and low voltage, and the same energy distribution companies. Much of the distribution network is already heavily exploited and needs to be modernized, which is associated with large financial outlay. Conducted by the company's investments should be economically justified and must contain optimal solutions for current and planned by the company's ventures in the energy sector.

Keywords: power, strategy, development, distribution networks, the efficiency of investment.

1. Introduction

The following text discusses the problem associated with the creation of distribution network development strategy in energy companies while safeguarding the effectiveness of investment in order to create a mechanism that will meet current energy demands, assuming of appropriate policies and activities of distribution companies. Creating long-term strategic plans for business development is essential to achieve those objectives, as well as financial gain from the distribution business unit of energy.

In recent decades there have been major changes in the energy sector, mainly related to national economic growth and increasing demand for electricity and heat by the public. The distribution companies have undergone a profound restructuring of today, where they are now privatized and liberalized. This sequence of events requires a new approach to planning development strategies of energy companies, as well as distribution companies must meet the relevant requirements in connection with the development of the energy sector, where new technologies are being implemented with increasing consumer demand for energy.
The development strategy of distribution companies is even more important, given the currently prevailing economic crisis. Because of him, many companies changed their attitude in connection with obtaining the best results in the shortest possible time, without paying attention to long-term development of the company, this resulted in a loss of liquidity, and ultimately bankruptcy.

A basic condition for the proper functioning of energy companies today is the efficiency of the current corporate management, as well as effective decisions on the overall development of the company and obtaining adequate funding for these goals. This evolution of the distribution companies should be implemented through specific investment projects and development of the basic criteria for the development of distribution networks such as the growing burden, the mechanical strength of the existing systems, the increasing number of loads and increased flows of energy while maintaining acceptable current density.

Therefore, the implementation of the development of the distribution companies should take into account a number of investment projects, which include:
- Replacement investments - to replace a worn out or obsolete systems with new, which will reduce the costs associated with the aging of the assets in the energy sector,
- Modernization investments - resulting in a reduction in electricity distribution costs associated with the introduction of new technologies,

- Business development - designed to meet the strategic development of early establishment of the energy business.

2. 2. Purpose of the energy company

Each energy company is in relation to a market economy and the law of the energy objective pursued. The main task of creating stable distribution companies is their sustainability. Depending on the adopted strategy of the unit, this development may also be negative, which could lead, in whole or in part to loss of control of the business. Consequently, it is related to the maintenance and survival of individuals in the energy market. Therefore, we should seek to ensure the proper growth and proper functioning of the distribution companies, which in turn reference a positive effect on both the investment and finance. Profit of the unit is possible when a company meets the requirements of addressing the needs of consumers for electricity, while maintaining the lowest price of production and reaching a high price for its sale.

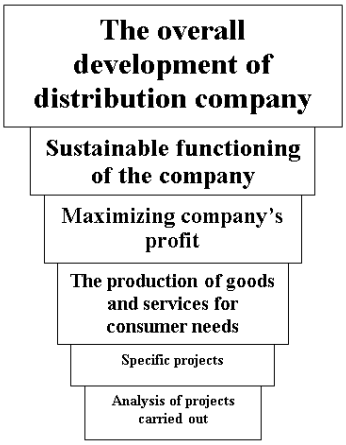

Fig.1. The hierarchy of objectives and activities of distribution company. Source: Own

The increase in the development of the distribution companies can be seen in the short and long term. Short-term measures include those that are non-investment. These include: the use of discounts to consumers, the extension of payment terms, to carry out organizational improvements in the units of distribution, or offer additional services to strengthen the relationship between the recipient and retailer of energy. However, long-term growth refers to the companies ongoing development projects at the turn of a few or several months in the energy company. This enables the construction and modernization of existing energy systems, as well as introducing new products and technologies to the energy market.

Another important objective for the existence of the distribution companies is to ensure national energy security. The basis for the safe operation of the energy sector is well developed and reliable transmission and distribution. The current distribution infrastructure in the coming years may prove to be insufficient for the needs of energy due to increasing demand for energy by consumers. Expansion and modernization of 110 kV and medium voltage network is a priority in order to ensure the safe supply of energy. Particularly important will be upgrading the network in rural areas and newly urbanized areas in the quality of energy supply. Downplayed the problem may in the future would result in transmission of energy, and even halting supplies to consumers. The actions of state bodies, the responsibility for the country's energy security, should move towards a legislative amendment to expedite and facilitate investment in the distribution. In view of the Polish energy commitments towards the European Union, state policy must provide clear and non-discriminatory regulatory mechanisms for the energy sector. The present law and its procedures are time consuming. The current legal status cannot be implemented in a timely manner most of the

elements of energy infrastructure to ensure energy security. Legal barriers to the energy sector may lead to failure to meet energy requirements in relation to the directives and guidelines of the European Union.

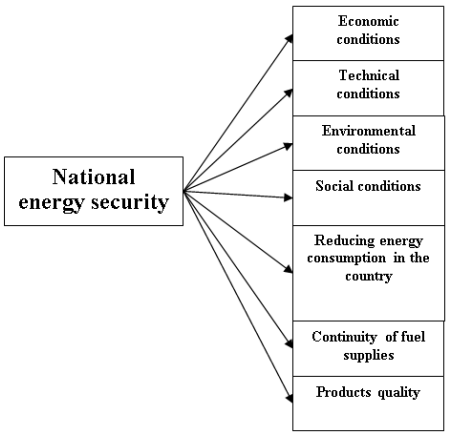

Fig.2. Constituent elements of national energy security. Source: Own.

All decisions taken, the distribution companies, in the direction of the selection of development activities can be divided into three main groups:

- Decisions to accept or reject an investment project undertaken in the enterprise energy,
- Decisions by which you selected the most profitable project among several investment options offered,
- Decisions to rationalize the development program for the distribution company.

Decisions concerning the development of energy enterprises should be based on the optimized criteria and actions. A useful tool, which forms the basis for making those decisions, can be employed cost-effectiveness of investment, which includes the following components: time of return and discounted payback period, return on capital, internal rate of return (IRR), net present value (NPV) and break - even.

3. Strategy and planning distribution company

The strategy of distribution companies in general is associated with economic and social contexts which define the directions of the case managers given unit of energy. In view of the situations that occur in the environment and taking into account their human potential, organizational, financial, technical and production management company is required to create new guidelines needed to achieve the development objectives set in advance. The strategy of one company is global, it affects the development and functioning of the whole power system of the country.

Adopted by the distribution company development strategy is a component of strategic planning as a formalized long-term plans which are used to define and implement the objectives of the unit. This is related to the achievement of the company's best performance distribution of electricity while maintaining the lowest investment costs. Strategic program of energy companies consider all factors favoring and hindering the achievement of previously set goals. This means the implementation of all development activities in the distribution company, which take into account the following considerations: economic, legal, environmental, technical, social, organizational, etc. Therefore, the strategy pursued by companies is the way to the objectives.

Keeping an appropriate strategy in the enterprise is strictly related to planning. Planning, as a function of unit management is the process of setting objectives and determine the best methods for their implementation. In addition, an analysis of potential projects to be undertaken to achieve the intended task. In addition, I use also examine the possibility of the unit distribution for the conditions, as well as how to respond depending on their volatility and how to manage your resources, as well as setting up events that could affect the further development of the energy

company. The task is also planning to eliminate all kinds of shortcomings in the quality, informational and administrative law in the distribution company.

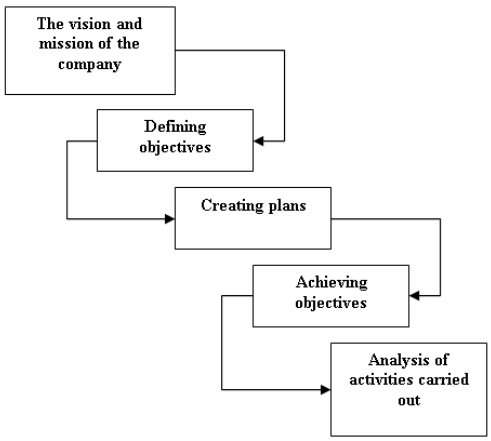

Fig.3. The planning process for development in the distribution company. Source: Own

4. Investments costs distribution networks

Distribution networks are constantly developing. Changes in the number of devices installed in the network, increases the number of energy consumers, and what is the associated change of power and energy losses. When designing the new power networks play an important role economic calculations. The high costs of network equipment mean that the choice of an appropriate design solution will determine the economic justification. The basic elements of economic calculation function criteria are capital costs and the costs of power losses and energy. The investment costs or costs of building new facilities will depend on: investment in basic construction (lines, stations), expenditures for additional investment in basic construction (eg, service station building for environmental protection), and additional expenses associated with the purchase of a license, and the implementation of the planned investment.

Capital expenditures for the construction of the new network are equal to the total capital expenditure on individual network devices. With the expansion of already existing distribution network to include additional expenditures for the purchase of new equipment and the cost of their connection to the network operated. When upgrading should be taken into account the direct costs associated with the improvement of the existing distribution network. For distribution lines total investment cost of a line of length 'l' is:

$$K_{cil} = k_{jl} \cdot l \qquad (1)$$

where: k_{jl} is being built at the expense of a separate new line [€/km].

Very often, when calculating the cost of the investment lines are included in the cost of transformers, along with stations, connectors, chokes, capacitors and additional costs associated with the planned investment, then the equation takes the form:

$$\left.\begin{aligned} K_{cis} &= \sum_{j=1}^{n_r} K_{irj} + K_{iT} + K_{in} + K_{id}, \\ K_{cir} &= \sum_{j=1}^{n_{rw,j}} K_{irwj} + \sum_{j=1}^{n_{rr,j}} K_{irrj}, \\ K_{ciT} &= \sum_{j=1}^{n_T} K_{iTj}. \end{aligned}\right\} \quad (2)$$

where:
K_{cis} - total investment cost of station,
K_{cir} - total investment cost of switchboard *j*,
K_{ciT} - total cost of transformers in the station with equipment,
K_{in} - capital costs of other devices (inductors, batteries, capacitors),
K_{id} - capital costs of additional equipment (building control room, compressed air equipment, equipment for himself),
$N_{rw,j}$ - number of fields equipped with a switchboard *j*,
$N_{rr,j}$ - number of fields in the switch of reserve *j*,
n_r - number of switchgears at station,
n_T - number of transformers in the station.

As mentioned earlier, in defining the principles of efficiency of investment in distribution companies also take into account the annual cost of power losses and energy. Need to include these costs result from the need to use more fuel in power stations to cover losses in the network and losses on the energy-producing facility. These costs are calculated from the formula:

$$K_{sme} = K_p \cdot (\Delta P_{max} + K_e \cdot \Delta Q_{max}) + K_A \cdot \Delta A \quad (3)$$

where:
ΔP_{max} - the maximum active power losses during the year in kilowatts,
ΔQ_{max} - maximum loss of reactive power in kilowatts per year,
ΔA - energy losses during the year,
K_p - the unit cost of power at a given point in the network [€/kW],
K_A - the unit cost of energy at a given point in the network [€/kWh],
K_e - the energy equivalent of reactive power at a given point in the network [kW/kvar].

As a complement to these methods of calculation of economic indicators also introduces the efficiency of investment that assess the investment in terms of reducing losses of electricity. Implies the introduction to the analysis of the indicators:

- Investment performance indicator for the line:

$$e_L = \frac{\delta \Delta E}{\Delta L \cdot k_{Lj}} \quad (4)$$

where:
ΔL - line growth during the period [km]
k_{Lj} - the cost of building 1 km of line [€/km]

- Investment performance indicator for the station:

$$e_F = \frac{\delta \Delta E}{\Delta F \cdot k_{Fj}} \tag{5}$$

where:
ΔF - increase the station during the period [pc]
k_{Fj} - the cost of building a distribution station [€/pcs]

Conclusion

The current state of distribution networks, as well as various storage facilities in our country is disappointing. The objectives and actions to improve them should be subject to general directions of development of various distribution companies. The development of these energy systems must be optimized in terms of social costs, technical economic, legal, environmental, and organizational.

With the increase in energy consumption and the growing demand of consumers will continue to be followed by an increase in audience share of total energy consumption in the country (agriculture, recipient existentially - households, small industry, service companies, etc.). The power and electricity is clearly affects the evolution of the energy and power transmitted by the electric grid (increased exploitation systems), and also requires relatively more resources to its development, in order to reduce their losses in transmission.

The increase in the share of energy consumption by increasing the public will require a relatively higher growth and greater financial resources for modernization of the most exploited, mainly medium and low voltage. This is because these networks have a decisive impact on the overall power and energy losses in all types of distribution networks. Downplayed the problem in creating economic development plans, distribution networks, or mistakes in choosing their optimal structure, significantly influence the resultant efficiency of the whole national electricity system. In addition, it can cause disturbance of Polish energy security, and ultimately stopping the supply of electricity to individual consumers.

References

[1] Gawlak A.: „*Sprawność sieci dystrybucyjnej"* – Efektywność w sektorze dystrybucji energii elektrycznej – Aspekty techniczne – Pod redakcją Anny Gawlak – Wydawnictwo TEKST sp. Z o.o. – Częstochowa 2009.
[2] Stós K.: „*Strategia a długofalowy rozwój przedsiębiorstwa energetycznego*."- Polityka energetyczna, Tom 12, Zeszyt 1. Wydawnictwo IGSMiE PAN , Kraków, 2009.
[3] Szkutnik J.: „*Efektywność w sektorze dystrybucji energii elektrycznej*" – Efektywność w sektorze dystrybucji energii elektrycznej – Aspekty ekonomiczne – Pod redakcją Jerzego Szkutnika – Wydawnictwo TEKST sp. Z o.o. – Częstochowa 2009.
[4] Szkutnik J.: „*Ekonomiczne podstawy programowania rozwoju systemu elektroenergetycznego*" – Efektywność w sektorze dystrybucji energii elektrycznej – Aspekty ekonomiczne – Pod redakcją Jerzego Szkutnika – Wydawnictwo TEKST sp. Z o.o. – Częstochowa 2009.
[5] Szkutnik J.: „*Modele zarządzania w przedsiębiorstwie dystrybucyjnym*" – Efektywność w sektorze dystrybucji energii elektrycznej – Aspekty ekonomiczne – Pod redakcją Jerzego Szkutnika – Wydawnictwo TEKST sp. Z o.o. – Częstochowa 2009.
[6] Szkutnik J.: „*Strategia rozwoju sieci rozdzielczych w spółce dystrybucyjnej, a możliwości zapewnienia środków budżetowych na jej realizację.*"- Budżetowanie działalności jednostek gospodarczych – teoria i praktyka, Oficyna Wydawnicza Akademii Górniczo – Hutniczej, Kraków – Zakopane, 2000.
[7] Tuma J., Martinek Z.: „*Security, quality and realiability of electrical energy*" – Wydawnictwo CONTE spol. S.r.o. CVUT Praha – Praga 2007.

Transcom 2011, 27-29 June 2011
University of Žilina, Žilina, Slovak Republic

Measurement of photovoltaic modules and solar radiation

[*]Jan Turcek, [*]Matej Hrasko
[*]University of Zilina, Faculty of Electrical Engineering, Department of Power Electrical Systems,
Univerzitna 1, 01026 Žilina, Slovakia, jan.turcek@fel.uniza.sk, matej.hrasko@fel.uniza.sk

Abstract. This paper deals with the measurement of basic characteristics of photovoltaic modules. It also describes the solar radiation measurement. The influence of module inclination to the size of output power and other specifics of photovoltaics were investigated too.

Keywords: photovoltaic, solar radiation, measurement.

1. Introduction

Photovoltaic (PV) is enjoying nowadays unprecedented interest in professional and general public. The source of energy has attributes like environmental friendliness, direct energy conversion of solar radiation to electricity or decentralized resources that contribute to its popularity. This energy source represents new ways of exploiting of available resources and electrification possibilities in non-reachable areas.

In contrast to all these positives there is a group of negatives, which causes an aversion to this energy source. Here we might include low efficiency of a conversion of solar energy into electricity, limited lifetime of PV panel caused by the cell-structure itself, high sensitivity to the external weather conditions, particularly the sensitivity to an amount of solar radiation and with that corresponding large variability in time-based power supply.

Another factor that we have to keep in mind while judging the PV sources is that their competition ability as on-grid applications in today's energetic market is ensured mainly by the legislative and the financial support.

2. Basic properties of photovoltaic panel

Basic properties and parameters can be determined by help of its Volt-Ampere (VA) characteristic. This characteristic defines volume of output power with the changing load. Measurement of VA characteristic was performed by mobile stand with two installed PV panels Moser Baer MBPV Max Series. These are polycrystalline silicon solar panels with 60 PV cells. Voltage and current values specified in PV modules datasheet were measured at standard test conditions (STC).

These STC are characterized by solar radiation 1000 $W.m^{-2}$, module temperature 25°C and air mass coefficient AM 1.5G. The air mass constant determines the radiation impact and the spectral combination of the light hitting the earth's surface. The letter G in this designation stands for global, which means that it includes the direct and the diffuse radiation. Measured short circuit current I_{SC} is 7.71 A and open circuit voltage U_{OC} is 35.72 V. The maximum power point (MPP) represents the operating point of VA characteristic with maximal power output measured under STC. Value of this output power is 197.41 W and measured MPP voltage U_{MPP} is 28.14 V and measured MPP current I_{MPP} is 7.01 A.

3. Measurement of photovoltaic panel

We measured VA characteristic at 21th March. The PV module was of 37.16 degree inclination to the horizontal plane. This value was chosen because the spring equinox occurs right at 21th March, the declination of sun is equal to zero and Earth continues to move towards the aphelion. For our latitude which is approximately 49.5 degree, it follows that the panel should be at the most effective inclination of 40.5 degrees. This value essentially corresponds with the preferred value of fixed PV installation inclination in Slovakia, which varies from 35 to 39 degrees. Mobile stand, we were using have got eight settings of inclination. Values of individual angles and corresponding measured open-circuit voltages are shown in Tab.1.

U [V]	33.5	33.9	34	34	34.1	34.1	34.1	34.05	34
α [°]	0	19,4616	29,5337	37,1637	43,9037	50,1967	56,2536	62,1937	68,103

Tab. 1. Measured voltages in relation to inclination

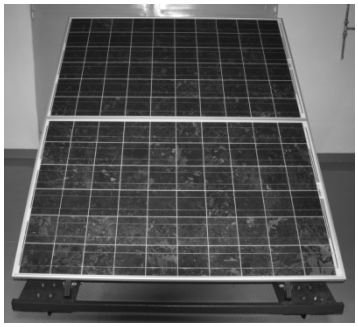

Fig. 1. Mobile stand with PV panels

Fig. 2. Visualization of mobile stand and inclination angle

We recorded surface temperature of PV module with infrared thermometer in 5 minute intervals during measurement which lasted from 12:00 till 12:30. These values are shown in Tab.2. The external temperature was 10 degrees during measuring process. We obtained this value from SHMU online data.

Time	12:00	12:05	12:10	12:15	12:20	12:25	12:30
Temperature [°C]	29,8	30,5	31	31,5	32	31,5	31

Tab. 2. Module temperatures measured in 5 minutes interval

The PV module surface is made by high transmission, low iron, tempered and textured glass with thickness of 3.2 mm. Given these characteristics and relative to the absorption properties of the PV cells themselves the changes of temperatures caused by total or partial covering are significant. As we expect year-round operation of PV plants, we have to monitor temperature changes. As the module temperature is partially inflicted changes of ambient temperature too, it is necessary to monitor this one, too. The reason for temperature changes monitoring is related with the PN junction characteristics and also with the PV cell properties. When the temperature rises there is a slight increase of short-circuit current but open-circuit voltage is decreasing. Nominal temperature of PV module is 25 degrees according to the STC. With the temperature increase there is a decrease of maximal power-output.

4. Measurement of solar radiation

As the measuring of VA characteristic last for half an hour we needed to secure higher outcome value of gained results. That’s why we measured global solar radiation during whole measuring process.

The measurement of solar radiation was done with KIMO SL200 device. This apparatus enables instant value of solar radiation measurement, it also enables statistical evaluation of measured results and the following data transfer to the computer where another work with them is possible. Two-day measurement with the use of mentioned device took place from 11th to 13th March. The measurement began at 11:50 of 11th March and it ended at 11:50 of 13th March.

The device record two values every sec and it is possible to make a 31 daylong uninterrupted measurement. KIMO uses solar cell with 1 cm^2 flat surface and device sensibility on spectrum of solar radiation ranges from 400 to 1100 nm.

Fig. 3 shows values of solar radiation for every time step in mentioned time period.

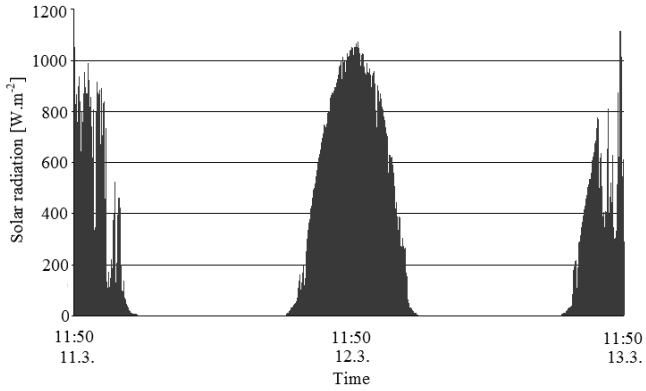

Fig. 3. Values of solar radiation measured with KIMO SL200.

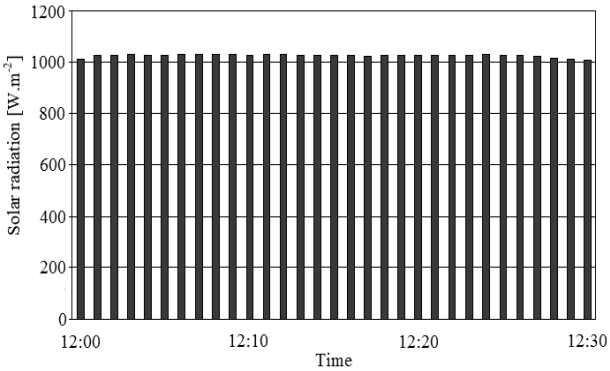

Fig. 4. Measured values of the solar radiation gained during the VA characteristic measurement

The measured values of solar radiation gained during measurement of VA characteristic are shown in Fig. 4 and it is obvious that we can expect this measurement to be correct because solar radiation was not changing a lot during the process. Maximal value of solar radiation was 1032 $W.m^{-2}$ and minimal value was 1002 $W.m^{-2}$.

5. VA characteristic

We measured VA characteristic which is shown in Fig. 5. We measured that short circuit current - I_{SC} is 7.3 A and open circuit voltage U_{OC} is 34.59 V. For the MPP the power output is 168.32 W with measured MPP voltage U_{MPP} = 26.3 V and measured MPP current I_{MPP} = 6.4 A.

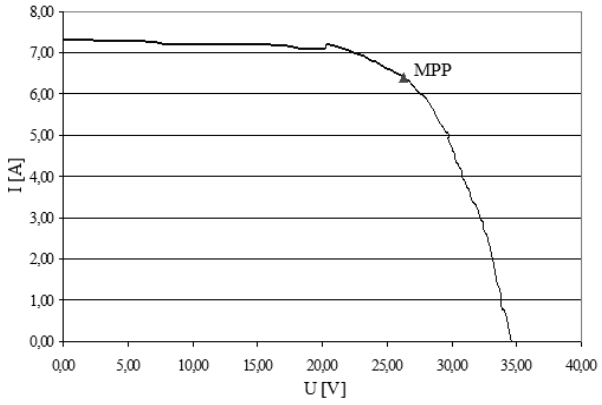

Fig. 5. VA characteristic of PV module

6. Long-term measurement

In addition to the measurement of VA characteristic and solar radiation we also made the measurement of output power of PV module which lasted more than four hours. Solar radiation

was also measured by KIMO apparatus during this measurement. Results of this measurement are shown in Fig. 6 and Fig. 7.

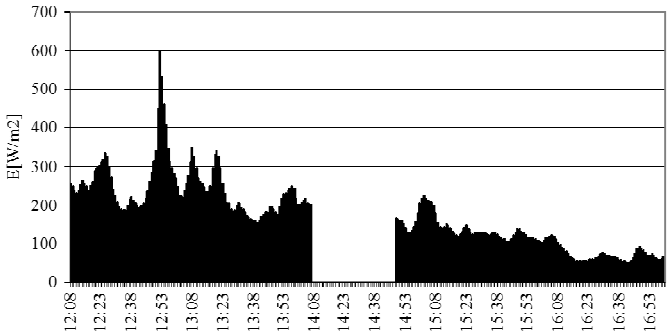

Fig. 6. Measured values of the solar radiation gained during long-term measurement.

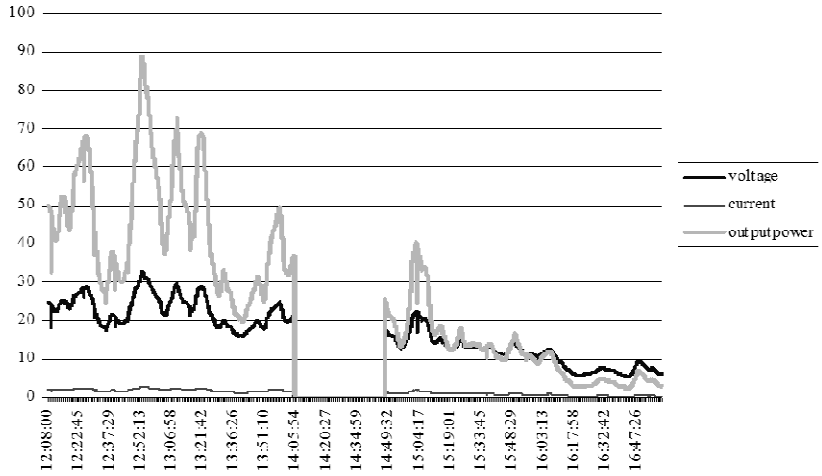

Fig. 7. Measured curves of voltage and current and calculated curve of output power.

7. Conclusion

Basic properties of the PV module and its behavior under various loads were verified by this measurement. We came near to STC in relation to solar radiation and module temperature during measurement. Therefore the result is measured VA characteristic which is very close to that one measured under STC. When measuring the impact of module inclination we concluded that the shift of 20 degrees to either side of the optimal angle has no significant effect on the output open-circuit voltage so that range of 40 degrees corresponds to 3% change of open-circuit voltage of PV module. Another fact which appeared during measurements is that by comparing multiple panels we found significant differences in the measured open-circuit voltages. We used panels consisting of 60 series-coupled PV cells. Open-circuit voltage of PV cell is reaching approximately 0.6 V according to datasheet. Open-circuit voltage drop of 2 V within one module practically means damage of four cells. This damage can be caused by inappropriate manipulation with modules during transportation or installation and assuming long-term application we can expect such damages caused for instance by the weight of snow blanket in the winter period.

References

[1] http://pvcdrom.pveducation.org/SUNLIGHT/AIRMASS.HTM, (accessed 12/10)

[2] http://www.moserbaersolar.com/resources/max-series-caap-bb.pdf, (accessed 01/11)

[3] http://www.shmu.sk/sk/?page=1&id=meteo_apocasie_sk&ii=11841, (accessed 03/10)

[4] http://eosweb.larc.nasa.gov/sse/, (accessed 02/11)

TRANSCOM 2011

Proceedings, Section 4

Published by University of Žilina
First Editions
Printed by EDIS-Žilina University publisher

ISBN 978-80-554-0373-1